

Wafer-Mounted Sensor Arrays for Plasma Etch Processes

by

Mason Lanse Freed

B.S. (University of California, Berkeley) 1997

M.S. (University of California, Berkeley) 1999

A dissertation submitted in partial satisfaction of the
requirements for the degree of
Doctor of Philosophy

in

Engineering - Electrical Engineering & Computer Science

in the

GRADUATE DIVISION

of the

UNIVERSITY of CALIFORNIA, BERKELEY

Committee in charge:

Professor Costas J. Spanos, Co-Chair
Professor Kameshwar Poolla, Co-Chair
Professor Michael A. Lieberman
Professor Andrew Packard

Fall 2001

The dissertation of Mason Lanse Freed is approved:

Co-Chair Date

Co-Chair Date

Date

Date

University of California, Berkeley

Fall 2001

Wafer-Mounted Sensor Arrays for Plasma Etch Processes

Copyright Fall 2001

by

Mason Lanse Freed

Abstract

Wafer-Mounted Sensor Arrays for Plasma Etch Processes

by

Mason Lanse Freed

Doctor of Philosophy in Engineering - Electrical Engineering & Computer Science

University of California, Berkeley

Professor Costas J. Spanos, Co-chair

Professor Kameshwar Poolla, Co-chair

This dissertation is concerned with the development of novel wireless sensor technologies appropriate for semiconductor manufacturing applications. More specifically, the feasibility of placing sensors directly onto the surface of a standard silicon wafer is explored. Such a wafer-mounted sensor system would be fully integrated. It would include driver electronics, a power supply, and a communication system, in addition to the sensing elements. As a result, measurements can be made *in-situ* to extract the process state. With such sensor systems, processes can be automatically optimized, equipment can be efficiently diagnosed, and traditional test wafers can be replaced by more effective “smart” sensor wafers.

The *status quo* of metrology methods in use in the semiconductor industry is first discussed. From this discussion, a compelling case for wireless sensor systems is made. Next, the impediments associated with engineering this type of system are discussed, and possible solutions are proposed. The remainder of the dissertation describes the design, fabrication, and testing of two types of sensors for plasma etch processes.

First, a film thickness sensor for polysilicon etch processes is presented. This sensor measures the resistance of a thin polysilicon film, and uses this information to infer

the film's thickness. Changes in the measured thickness, due for example to etching, can be directly sensed by this device. The sensor system incorporates a temperature sensor, both for measuring wafer surface temperature, and for compensation of the film thickness sensor against thermal variations. Design, fabrication, and testing results of this sensor are presented.

Next, a thermal flux sensor for plasma etch processes is developed. In plasma etch processes, there are many sources for the heat delivered to the wafer. The two most significant sources are the ion flux heating and the surface chemical reaction heating. The sensor discussed in this work is capable of separately measuring both effects, for use with equipment design, diagnostics, or control. Design, fabrication, and testing results of this sensor are presented.

Finally, future directions for this research topic are offered. In particular, alternate sensors, improved isolation, and novel uses for the sensor data are discussed.

Professor Costas J. Spanos
Dissertation Committee Co-Chair

Professor Kameshwar Poolla
Dissertation Committee Co-chair

To Julianna, whom I hope to see
more often now that this is done.

Contents

List of Figures	vi
List of Tables	ix
List of Symbols	x
1 Introduction	1
1.1 Summary of Results	4
1.2 Outline of Dissertation	4
2 Motivation	6
2.1 Existing Solutions	6
2.1.1 Wired Sensor Wafers	6
2.1.2 Test Wafers	7
2.2 Wireless Sensor Wafers	9
2.3 Summary	9
3 Plasma Etch Sensors	11
3.1 Introduction	11
3.2 Background	11
3.2.1 History / Motivation	12
3.2.2 Plasma Physics	13
3.2.3 Plasma Etch Equipment	14
3.2.4 Associated Problems	20
3.3 Importance	20
3.3.1 Many Variables to Measure	21
3.3.2 Complexity	21
3.3.3 Harsh Environment	22
3.3.4 Suitability for Wafer-Mounted Sensors	23
3.4 Challenges	23
3.4.1 Harsh Environment	23

3.4.2	Difficult communications	24
3.4.3	Contamination	25
3.5	Sensor Choice	26
3.5.1	Etch Rate	26
3.5.2	Thermal Flux	27
3.6	Summary	27
4	Etch Rate Sensor	29
4.1	Introduction	29
4.2	Motivation	29
4.3	Related Research	31
4.4	Design Issues & Choices	32
4.4.1	Mechanical Techniques	32
4.4.2	Optical Techniques	34
4.4.3	Electrical Techniques	35
4.4.4	On-Wafer Sensor Choice	37
4.5	Results	38
4.5.1	Process Flow	38
4.5.2	Temperature Compensation	38
4.5.3	Experimental Technique	42
4.5.4	Calibration	44
4.5.5	Experimental Results	47
4.6	Summary	57
5	Thermal Flux Sensor	58
5.1	Introduction	58
5.2	Motivation & Related Research	59
5.3	Sensor Design	60
5.3.1	Geometrical Considerations	60
5.3.2	Transduction Method	61
5.3.3	The Gardon Gauge	62
5.4	Standard Gardon Gauge: Operation	63
5.4.1	Operating Principle	63
5.4.2	Membrane	65
5.4.3	Temperature sensors	67
5.4.4	Wheatstone Bridge	67
5.4.5	Complete System	69
5.5	Standard Gardon Gauge: Analysis Assumptions	70
5.5.1	Incident Thermal Flux is Spatially Uniform	70
5.5.2	Incident Thermal Flux Strikes Top Surface Only	70
5.5.3	Membrane has Spatially Uniform Thermal Properties	71
5.5.4	Temperature Measurement Sensor has Zero Size	71

5.5.5	All Heat Flows Out Membrane Edges	71
5.6	Standard Gardon Gauge: Performance	77
5.6.1	Sensitivity	77
5.6.2	Responsivity	77
5.6.3	Power Dissipation	78
5.6.4	Time Constant	82
5.6.5	Thermal Noise	83
5.7	Sensitivity Problem	84
5.8	Modified Gardon Gauge: Operation	85
5.9	Modified Gardon Gauge: Analysis	86
5.9.1	Sensitivity	86
5.9.2	Responsivity	88
5.9.3	Power Dissipation	88
5.9.4	Time Constant	89
5.9.5	Thermal Noise	89
5.9.6	Antenna Deflection	89
5.9.7	Built-in stress	93
5.9.8	Parasitic Heat Transfer	93
5.9.9	Analysis Summary	94
5.10	Numerical Optimization of Modified Gauge	96
5.10.1	Optimization Setup	96
5.10.2	Optimization Results	98
5.11	Modified Gardon Fabrication	101
5.11.1	Requirements	101
5.11.2	Process Flow	105
5.11.3	Final structure	107
5.12	Experimental Results	107
5.12.1	Bench-top Experiment	107
5.12.2	Low Pressure Experiment	111
5.12.3	O ₂ Plasma Experiment	121
5.13	Summary	123
6	Conclusion	125
6.1	Dissertation Summary	125
6.2	Future Research Directions	126
	Bibliography	128
	A Four Point Probe Analysis	138
	B Film Thickness Sensor Process	141
	C Thermal Flux Sensor Process	143

D	Matlab Code	147
D.1	Matlab program: <code>sim_structure.m</code>	147
D.2	Matlab program: <code>optfun.m</code>	149
D.3	Matlab program: <code>optnonlcon.m</code>	150
D.4	Matlab program: <code>optimization.m</code>	151
D.5	Modified Gardon Optimization Results	153
D.6	Matlab program: <code>findexps.m</code>	155

List of Figures

2.1	Wired temperature sensor wafer manufactured by SensArray Corporation.	7
2.2	Peak temperature indicator label manufactured by Omega Engineering, Inc.	9
3.1	Comparison of isotropic undercutting of the mask and anisotropic etching with correspondingly less mask undercut.	12
3.2	Barrel plasma reactor configuration.	15
3.3	Parallel plate capacitively driven plasma reactor configuration.	16
3.4	Coaxial, “hexode” capacitively driven plasma reactor configuration.	17
3.5	High density plasma source configurations.	19
3.6	Variables affecting the operation of a plasma.	22
4.1	Collinear four-point probe arrangement. Note that $D \gg s$	35
4.2	Generic van der Pauw sheet resistance measurement structure.	37
4.3	van der Pauw sheet resistance measurement structure.	38
4.4	Etch rate sensor wafer design #1.	39
4.5	Etch rate sensor wafer design #2.	39
4.6	Etch rate sensor wafer design #3.	40
4.7	Etch rate sensor wafer design #4.	40
4.8	Simplified fabrication process for polysilicon van der Pauw sensor wafer.	41
4.9	Dual van der Pauw sensor arrangement allowing simultaneous measurement of film thickness and temperature	42
4.10	Photo of XeF_2 etching system used for etch rate sensor testing.	43
4.11	Photo of edgeboard connector attached to sensor wafer.	45
4.12	Photo of XeF_2 chamber with electrical feedthroughs and sensor wafer in place.	45
4.13	Plot of data from thermal calibration of etch rate sensor.	46
4.14	Plot of sensor resistivity versus temperature.	47
4.15	Experimental results from in-situ XeF_2 etch tests.	49
4.16	Sensor output with constant-thickness, for repeatability determination.	51

4.17	Results from the second in-situ XeF ₂ etch experiment, data set #1. . .	54
4.18	Results from the second in-situ XeF ₂ etch experiment, data set #2. . .	55
4.19	Results from the second in-situ XeF ₂ etch experiment, data set #3. . .	56
5.1	“Direct” thermal flux measurement structure.	61
5.2	Gardon type thermal flux sensor.	64
5.3	Closeup of Gardon gauge structure, with dimensions and material properties labeled.	65
5.4	Differential element of gardon gauge membrane, used for thermal analysis.	66
5.5	Standard Wheatstone bridge resistor configuration.	68
5.6	Wheatstone bridge arrangement for gardon gauge structure.	69
5.7	“Serpentine” resistor pattern for center temperature measurement resistor.	79
5.8	Gardon membrane with buried center temperature sensing resistor. . .	80
5.9	Approximation used to calculate the sensor time constant.	83
5.10	Modified thermal flux sensor design, with added heat-funneling antenna. .	85
5.11	Closeup of modified Gardon structure, with dimensions and material properties labeled.	87
5.12	Model used for calculation of antenna flexure due to gravity.	90
5.13	SEM image of nitride plate partially destroyed by XeF ₂ etchant. . . .	102
5.14	SEM image of 0.5 μ m nitride plate, supported in the middle, over the top of a 120 μ m pit etched into the silicon substrate by XeF ₂ etchant. .	104
5.15	SEM image of modified Gardon structure with high levels of residual stress. This antenna was constructed using a SiO ₂ / aluminum sandwich structure.	105
5.16	Simplified fabrication process for thermal flux sensor construction. . .	106
5.17	SEM image of modified Gardon structure, <i>without</i> photoresist coating. . . .	108
5.18	SEM image of modified Gardon structure, <i>with</i> photoresist coating. . . .	108
5.19	SEM image closeup of modified Gardon structure, <i>without</i> photoresist coating.	109
5.20	SEM image closeup of modified Gardon structure, <i>with</i> photoresist coating.	109
5.21	SEM image of cross section of modified Gardon structure, with complete antenna still present.	110
5.22	Closeup SEM image of sub-membrane pit etched with XeF ₂	110
5.23	Diagram of experimental setup used to verify and calibrate the heatflux sensors.	112
5.24	Photo of thin-film heater and off-the-shelf thermal flux sensor.	112
5.25	Photo of thermal flux sensor die connected to edgeboard connector. . . .	113
5.26	Plot of sensor voltage output and commercial sensor output vs. time. . . .	115

5.27	Calibration curve showing sensor voltage output vs. measured thermal flux.	116
5.28	Example of sensor failure at low pressure.	119
5.29	Plot of prototype sensor sensitivity vs. pressure.	120
5.30	Plot of thermal flux sensor output during an experimental run inside an active O_2 plasma.	122
5.31	Plot showing a method for determination of the plasma thermal flux from the time decay after shutdown of plasma.	124
6.1	“Clam-shell” sensor wafer, with electronics, power supply, and communications system fully encapsulated inside a standard silicon wafer.	127
A.1	Infinite sheet with linear four-probe arrangement	138

List of Tables

4.1	XeF ₂ etch rate sensor experimental procedure.	48
4.2	Results of sensor and NanoSpec measurements.	50
5.1	Summary of analytical results for both the standard Gardon gauge structure and the “modified” Gardon structure.	95
5.2	Constraints imposed on numerical optimization of modified Gardon structure.	97
5.3	Summary of materials and process-related parameters used in Gardon gauge analysis. These factors are assumed to be fixed when considering geometrical tradeoffs.	99
5.4	Summary of geometrical parameters used in Gardon gauge analysis. These factors may be tuned to maximize sensitivity.	100
5.5	Results from Matlab optimization of the modified Gardon gauge structure	100

List of Symbols

a	Antenna diameter (in μm)
α	Temperature coefficient of resistivity (in $\frac{\%}{\circ C}$)
b	Antenna support post diameter (in μm)
c	Membrane specific heat (in $\frac{J}{kgK}$)
c_{ant}	Antenna specific heat (in $\frac{J}{kgK}$)
D	Membrane diameter (in μm)
Δf	Sensor bandwidth (in Hz)
ΔT	Temperature difference across a heat flux sensor (in K)
h	Antenna thickness (in μm)
κ	Membrane thermal conductivity (in $\frac{W}{mK}$)
λ	Minimum lithographic linewidth (in μm)
$P_{electrical}$	Electrical heating power dissipated in center resistor (in W)
q	Thermal flux (in $\frac{W}{m^2}$)
q_{\perp}	Thermal flux perpendicular to a sensor (in $\frac{W}{m^2}$)
$q_{n,equiv,chem}$	Noise-equivalent (chemical) thermal flux (in $\frac{W}{m^2}$)
$q_{n,equiv,ion}$	Noise-equivalent (ion flux) thermal flux (in $\frac{W}{m^2}$)
$q_{p,equiv}$	Equivalent thermal flux due to resistive heating (in $\frac{W}{m^2}$)
R_{chem}	Responsivity to chemical heating (in $\frac{V}{W}$)
R_{ion}	Responsivity to ion flux heating (in $\frac{V}{W}$)
ρ	Membrane material density (in $\frac{kg}{m^3}$)

ρ_{ant}	Antenna material density (in $\frac{kg}{m^3}$)
ρ_e	Electrical resistivity (in Ohm-cm)
ρ_s	Sheet resistance (in $\frac{\Omega}{\text{sq}}$)
S_{chem}	Sensitivity to chemical heating (in $\frac{\mu V}{W/m^2}$)
S_{ion}	Sensitivity to ion flux heating (in $\frac{\mu V}{W/m^2}$)
t_o	<i>A-priori</i> measurement of etch rate sensor thickness (in μm)
$t_{\text{compensated}}$	Temperature-compensated thickness measurement (in μm)
T_e	Electron temperature (in K , or in V with $V = \frac{kT}{q}$)
T_i	Ion temperature (in K , or in V with $V = \frac{kT}{q}$)
T_o	Temperature at the edge of a Gardon gauge structure (in K)
T_c	Temperature at the center of a Gardon gauge structure (in K)
τ	Sensor time constant (in s)
v_e	Electron thermal velocity (in $\frac{m}{s}$)
v_i	Ion thermal velocity (in $\frac{m}{s}$)
v_{max}	Maximum physical deflection at antenna edge (in μm)
V_{buried}	Voltage output from the non-exposed etch rate sensor (in V)
V_{DD}	Wheatstone bridge supply voltage (in V)
V_{exposed}	Voltage output from the exposed etch rate sensor (in V)
w	Membrane thickness (in μm)

Acknowledgements

Many people helped me complete this project, and many others made my stay at Berkeley an enjoyable one. For these things I am infinitely grateful. I'm not a terrifically witty person, so I find it difficult to come up with a good story for every person who has influenced me along the way. Also, my memory isn't what it used to be, which means that I've likely left people out of these acknowledgements. For both of these facts, I apologize; I hope nobody is slighted by my oversight.

First, and foremost, I'd like to thank my mentors, Kameshwar Poolla and Costas Spanos, for the wisdom, direction, and friendship they have shown me. Without their guidance, and not just in relation to academic pursuits, I definitely wouldn't be where I am today. I owe them a debt of gratitude, which I will attempt to repay when and where I can.

I would like to thank Professors Michael Lieberman, Andrew Packard, Nathan Cheung, Tsu-Jae King, Kristofer Pister, and Andrew Isaacs for the advice they've given me, and for their assistance with my research and class pursuits. I'd also like to thank all of the professors whom I've had the privilege of taking a class from at Berkeley; they taught me a great deal, some of which I still remember.

Many of my fellow students deserve thanks for their friendship and advice. First, I'd like to thank Darin Fisher and Michiel Krüger for allowing me to bounce mediocre ideas off of them and have great ideas reflected back. Chris Pfaff has been a good friend since we braved 107B many years back, and I look forward to many more golf games and good times. The current and former members of the BCAM and BCCI labs (Roawen Chen, Sundeep Rangan, Anna Ison, Nickhil Jakatdar, Xinhui Niu, Junwei Bao, Haolin Zhang, Jae-wook Lee, Dongwu Zao, Tiger Chang, Jason Cain, Ralph Foong, Tim Duncan, Jiangxin Wang, Payman Jula, Zach Lerner, Mareike Claasen, Greg Wolodkin, Garrett Stanley, KJ Al-Ali, Dave Faris, Eric Wemhoff, John Mussachio, Zach Jarvis-Wloszek, Rodney Martin, Elaine Shaw, Alpay Kaya, Lance Hazer, Lun Li, Kunpeng Sun) made my stay here both fun and educational, and for

that I am grateful. I've met many other interesting and friendly people during my stay (Kyle Leboutitz, Yashesh Shroff, Vito Dai, Mathew Wasilik, Karen Cheung, Sat Pannu, Alex Papavasiliou, Wesley Chang, Andrew Miner, Angela Marchetti, Andrea Franke, Adam Wengrow, William Wong, and Michael Guddal, to name a few) and I've very much enjoyed knowing them.

My experience with the "real world" has been limited; therefore, the advice and support I received from several people out there, including Randy Mundt and John Plummer, was much appreciated.

All of the fabrication for this project was performed in the UC Berkeley Microfabrication Laboratory. This allowed me to get my hands dirty (well, as dirty as you can get in a cleanroom) and learn the intricate yet crucial details of IC processing that aren't taught in a classroom. I am therefore thankful for the expertise and attention of the people who keep this laboratory up and running: Katalin Voros, Bob Hamilton, Marilyn Kushner, Sia Parsa, Kim Chan, Jim Bustillo, Joe Donnelly, Ben Lake, Phill Guillory, Susan Kellogg-Smith, Madeleine Leullier, Leon Tsao, Zeb Rapp, Mitra Javandel, and many others. Also, I am thankful for the help that Guobin Wang, Scott Eitapence, Kevin Cho, and Andy Gleckman gave me by doing much of my "dirty" work. As it turns out, much of the importance lies in the details.

Without money, research is difficult, and for this reason I am thankful for the fellowships and scholarships that were generously offered to me: the UC Berkeley Drake Scholarship, the UC Berkeley Chancellors Scholarship, the Department of Defense Graduate Research Fellowship, the National Science Foundation Graduate Fellowship, and the Intel Foundation Graduate Research Fellowship. In addition, my research was supported by the UC SMART program, under contract #SM97-01.

Finally, to my family I'd like to extend my warmest admiration and appreciation for the encouragement, advice, love, and support that they've given me over the years. It is difficult to put my feelings toward them to words. Without them, where would I be?

Chapter 1

Introduction

As semiconductor linewidths shrink to ever smaller dimensions, there is a growing need for tighter process and equipment control. This is driven both by the need to reduce variability with each technology generation, as well as the need to improve yield and time-to-yield. However, in order to implement any control scheme, process measurements must be made; these measurements form the basis for the control action.

There are many ways in which these measurements can be made. The traditional method is to have a standalone metrology station to which wafers are brought and measured. This type of measurement scheme works well for processes that need few measurements of variables that are complicated to measure. However, because the metrology equipment is located remotely from the standard process flow, and the measurement typically takes a relatively long time to complete, standalone metrology seriously reduces the fab throughput [1]. Further, this type of equipment has the disadvantage that it takes up substantial “footprint” within the fab, increasing the overall cost of the facility. Finally, because only a small fraction of the production flow can be measured in this way, process trends and equipment problems take longer to detect.

Because standalone metrology has these problems, the growing industry trend is

toward in-line metrology [1]. Where possible, measurement equipment is being moved from standalone stations to integrated measurement systems physically attached or in close proximity to the equipment. These in-line systems have the ability to measure every wafer going into or out of the process, as opposed to just a fraction. Because much more data is available, process fluctuations and trends can be accurately monitored and recorded. Also, because the data is taken more frequently, adjustments to the process can be made more frequently, so product variability can be reduced. Finally, by measuring all of the wafers in-line and allowing them to continue instead of removing selected wafers for metrology, more production wafers can reach process completion, improving throughput.

Unfortunately, there are still a few problems with the in-line metrology model. First, the money and time that it takes to integrate metrology stations onto process equipment is significant [1]. Because the original equipment was typically not designed with this modification in mind, parts, viewports, and loading systems must be retrofitted to accommodate the new sensors. For example, to integrate an ellipsometer onto a plasma etch chamber would require the addition or modification of the chamber viewports to allow direct optical access to the wafer at the proper viewing angle. It is also possible that these physical equipment modifications can adversely affect the stability of the process. In addition, because the metrology system is now part of the equipment, when there are metrology problems, the entire machine must be taken down for maintenance, reducing the equipment availability. The sensors therefore reduce the overall system throughput.

For these reasons, the next paradigm shift might be from sensors on the equipment to sensors on the wafer. Such an “integrated sensor wafer” would contain multiple process sensors, measurement electronics such as analog to digital converters and signal processors, an onboard power source, and a method for wirelessly communicating the sensor data to the outside world. Because the sensor wafer would physically resemble a standard product wafer, both in terms of materials and physical dimensions,

the equipment could load and process this wafer in the same way as any other wafer. Therefore, no modifications would need to be made to the equipment at all; the complete sensor system would reside on the wafer. The visualization and/or storage of the data could be provided by an external computer (the “base station”), which would not require any physical connection to the process equipment. The data would be transmitted directly (via RF, IR, or other wireless method) from the sensor wafer to the base station. In this way, the same process information is gleaned but with minimal invasion into the process chamber.

It is important to note that integrated sensor wafers will never completely replace in-line or standalone metrology. Because all of the measurement equipment must be located on the wafer, many sensor types are impossible to incorporate. For these types of sensors, standalone or in-line metrology is the only option. In addition, some variables that are either very easy to measure, or very important to measure on every wafer, in-line or *in-situ* metrology is clearly better. In these cases, the lost throughput and data resulting from occasional sensor-wafer measurement is unacceptable. However, for many processes and variables of interest, wafer-mounted sensors are advantageous.

This overall research project seeks to provide evidence that sensor wafers can be built: that relevant sensors can be fabricated onto a wafer, that wireless power and communications methods can be placed onto a wafer, and that these completed sensor wafers can survive and function within a harsh process environment. The latter two aspects pose challenging problems that are beyond the scope of this thesis; other research addresses these issues [2-8]. This dissertation exclusively addresses the design, fabrication, and testing of the sensors.

1.1 Summary of Results

This dissertation investigates the design, fabrication, and testing of two types of on-wafer sensors: an etch-rate / film-thickness sensor and a spatially-resolved thermal flux sensor. These sensors were constructed on standard silicon wafers using standard semiconductor processes. Because the focus of this research is on novel sensors for semiconductor processes, the sensors are connected to the “outside world” using physical connections, i.e. cables. However, the sensors were designed to be compatible with wireless operation; this means that their power requirements are low enough that they can be powered by standard off-the-shelf lithium batteries, and their interface is such that they can be queried by a standard microcontroller chip.

Several prototype etch-rate sensors were successfully designed and fabricated. Further, temperature compensation sensors and circuitry were included to mitigate the sensor’s inherent temperature sensitivity. The sensors were tested both on the bench and *in-situ* during a XeF_2 silicon etch process. Data from these experiments suggest an accuracy of 50\AA , a repeatability of 15\AA , and a stability of better than 1\AA .

Several thermal flux sensors were also successfully designed and fabricated. Bench-top testing was used to confirm the functionality of the sensors, and low-pressure testing was used to measure their performance characteristics. This testing yielded a measured sensitivity of $0.25 \frac{\mu\text{V}}{\text{W}/\text{m}^2}$, a repeatability of $8.3 \text{ W}/\text{m}^2$, and a time constant of 19 seconds. These sensors were then placed into an commercial plasma chamber and etched, and data from this experiment were recorded.

1.2 Outline of Dissertation

This dissertation discusses the design, fabrication, and testing of several sensors, for use with on-wafer sensor applications. We focus exclusively on the sensors themselves, and only mention the specifics of power, communications, and isolation in passing. Other research is being conducted into methods for accomplishing these

tasks, and the reader is referred to [2–8] for more information on these subjects.

The organization of the remainder of this dissertation is as follows. In Chapter 2, we discuss the alternative wireless measurement schemes that are available, and motivate the use of this type of integrated sensor wafer. Chapter 3 provides motivation for the decision to focus on plasma-related sensors. Here, we also provide a background on plasma processes and processing equipment. From this discussion, a list of desirable sensors is derived. The next two chapters, 4 and 5, describe the design, fabrication, and testing of various prototypes of two of these sensors: an etch rate sensor and a thermal flux sensor. Finally, Chapter 6 concludes with a summary of the dissertation, as well as a few suggestions for future research directions.

Chapter 2

Motivation

2.1 Existing Solutions

There are several alternatives to the proposed sensor-wafer concept. Each allows the measurement of semiconductor process variables without making modifications to the process equipment. However, each has serious shortcomings that limit its utility.

2.1.1 Wired Sensor Wafers

Wired sensor wafers are commercially available [9]; these consist of a wafer with attached sensors, with a bundle of wires connecting the sensors to the outside environment (see Figure 2.1). The principal downside of this type of approach is that the wires severely limit the use of the product. To make a measurement from inside a plasma chamber, for example, the chamber must be vented and disassembled to allow the hand-placement of the wafer onto the chuck, a vacuum feedthrough must be added to the chamber (if not already present) to allow the wires to be fed into the chamber, and then the chamber must be re-assembled and pumped down. For typical processes, this process takes several hours to complete [10]. Once the measurement is complete, the entire process must be repeated to remove the sensor wafer

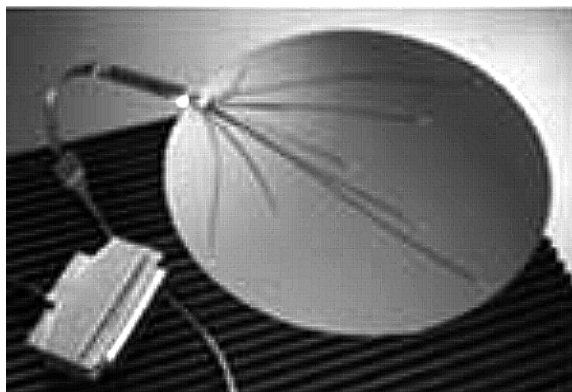


Figure 2.1: Wired temperature sensor wafer manufactured by SensArray Corporation [9].

and return the equipment to normal working order. Even for seemingly more benign environments, such as lithography bakeplates, several hours of downtime are required due to the wired wafer's inability to be handled by standard wafer robotics. These limitations severely limit the use of wired sensor wafers, and they are typically used only for equipment design, where throughput and cleanliness are not major concerns. In addition, commercially-available wired wafers typically measure temperature only, and do not contain sensors for other variables.

2.1.2 Test Wafers

The most widespread test method in production processes involves test wafers. This involves the processing of a blank or nearly-blank silicon wafer using the process of interest, and then measuring the characteristics of the wafer. For example, in an etch process, a wafer with only the material layer and the pattern of interest is processed by the equipment. After the process, the linewidth and line profile are measured to deduce equipment performance. This method has the advantage that it does not require any modifications to the equipment. However, the major disadvantage is that it does not directly measure process attributes. It measures only the integrated effect on the final product, and the connection between the two is some-

times difficult or impossible to ascertain. Therefore, this is typically used as a way to detect machine problems or calibration errors, but it is less useful as a diagnostic tool for repair. Another disadvantage of this method is that the typical measurements that are made on the wafer (usually critical dimension, or sometimes process-specific quantities such as etch rate or selectivity) must be made using specialized sensor equipment, i.e. standalone metrology.

While the use of test wafers does allow the features of interest on the wafer (such as critical dimension) to be directly measured, it can sometimes mask latent equipment problems until much too late. For example, as a process goes out of control, it is possible that the critical dimension will stay constant for a period of time due to nonlinearities in the process. If these effects are directly measured, this condition can be detected and repaired sooner.

Temperature Labels

One special case of test wafers is the use of so called “temp-dots”. These commercially available sensors [11] are in widespread use for temperature measurement in plasma environments. They consist of an adhesive-backed sheet of plastic-coated material which undergoes a permanent color change when its temperature rises above a threshold (see Figure 2.2). By having materials with several different thresholds on a single plastic sheet, the peak temperature can be measured by finding the lowest temperature threshold that did not change color. These dots are adhered to the surface of a blank wafer, the wafer is sent through the process, and the peak temperatures are read when the process is complete. While this method offers the convenience and usability offered by the wireless approach, they have low accuracy and resolution, low spatial resolution, and no time-resolution. Typical labels offer at most 3°C resolution, and a limited temperature range. They are fairly large, limiting the number of wafer points measured to at most 20. Finally, since they only show the peak temperature encountered by the wafer, useful real-time information is completely lost. For these

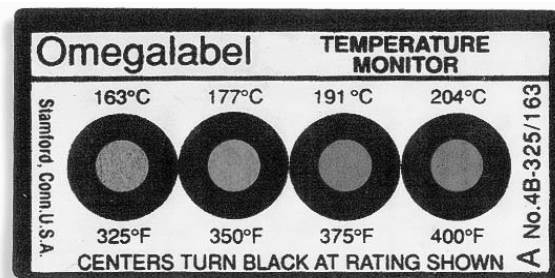


Figure 2.2: Peak temperature indicator label manufactured by Omega Engineering, Inc. [11]

reasons, temp dots are limited to basic equipment re-calibration after maintenance, and to ruling out major equipment flaws.

2.2 Wireless Sensor Wafers

In principle, a wireless wafer containing sensors, electronics, a power supply, and communications would solve all of the problems discussed above. It would allow measurements to be taken from within a process chamber, without modifying the equipment, and without disrupting the normal process flow. It would measure process-specific variables of interest directly, and could measure wafer-state variables as well. The measurements made would be accurate, highly spatially-resolved, highly time-resolved, and they would be instantly available without the use of a separate metrology station.

2.3 Summary

In this chapter, we described the existing alternatives to the proposed wafer-mounted sensor concept. Included in this list were wired sensor wafers, blank test wafers, and temperature labels. Each of these types of metrology has drawbacks that limit its practical use in production semiconductor processes. This chapter also

introduces the concept of a wireless sensor wafer, and the advantages of this technique are briefly listed. The next chapter discusses the wireless sensor concept in more detail, in addition to providing a background for plasma etch processes, the target process for this research.

Chapter 3

Plasma Etch Sensors

3.1 Introduction

This chapter will first present a background on plasma physics and plasma processing equipment. Following this, the need for sensors in plasma processing will be discussed. Next, the difficulties involved with the placement of wireless, wafer-mounted sensors into a plasma tool will be enumerated. Finally, the complete list of desirable plasma sensors will be given, along with justification for choosing the two sensors discussed in this dissertation.

3.2 Background

Because both of the sensors described in this dissertation are geared toward plasma etch processes, it is necessary to give a brief background on plasmas. This will be a basic introduction to the subject, and the reader is directed to [12] for a detailed analysis.

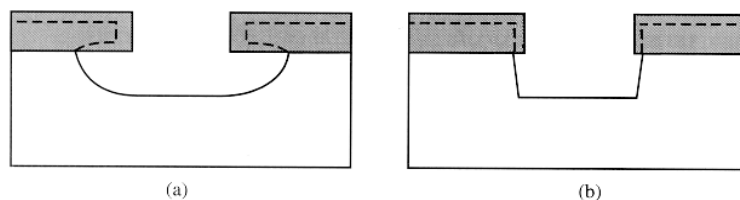


Figure 3.1: Comparison of (a) isotropic undercutting of the mask, and (b) anisotropic etching with correspondingly less mask undercut [13].

3.2.1 History / Motivation

In the early days of the IC industry, wet chemical etchants were used for all etch processes. Wet etchants are both highly selective and easy to use. However, most wet etchants are isotropic, etching material in all directions at the same speed. Therefore, they undercut a photoresist mask by the same distance that they etch downward through the film (Figure 3.1a depicts this situation). So, as line widths decreased and became comparable to the thickness of the thin films, wet etchants became useless.

In addition to this line width problem, several materials are difficult to etch using wet etching. For example, the Si_3N_4 passivation layer on top of the finished ICs can only be etched using HF, which is not selective to the underlying SiO_2 layer, or by using hot H_3PO_4 , which requires the use of a SiO_2 masking layer.

To counteract these effects, a directional, anisotropic etch process was necessary. For this purpose, plasma etching was adopted by the industry. This process utilizes electromagnetic fields to excite a gas and create reactant etchant species. Further, electrical biases that either form naturally inside the plasma or are externally applied cause ions inside the plasma to be accelerated toward the wafer. The directional nature of these high-speed ions allows the etch process to be highly directional, causing vertical sidewalls and very little undercutting of the mask. Figure 3.1b shows a depiction of a typical anisotropic etch profile. In addition, many reactants can be formed inside a plasma that do not exist in a wet chemical form. For example, a

CF_4 / O_2 plasma creates atomic fluorine atoms which readily etch Si_3N_4 [13].

3.2.2 Plasma Physics

A plasma can be generally described as a mixture of ionized particles and free electrons that is electrically neutral on average. While this description encompasses a wide range of plasma types and conditions, a more specific class is typically used in semiconductor processing. This type of plasma, called a “low pressure glow discharge”, is weakly ionized (meaning most of the gas molecules are neutral), low pressure (1 mTorr to 1 Torr), and non-equilibrium (meaning the electrons contain most of the energy and the ions remain near room temperature). There are many methods used to create and maintain a processing plasma, and these are described in Section 3.2.3; the general features of a plasma are described in this section.

The thermal velocities of the free electrons and ions inside the plasma are given by the equations [14],

$$v_e = \left(\frac{eT_e}{m} \right)^{\frac{1}{2}} \quad (3.1)$$

$$v_i = \left(\frac{eT_i}{M} \right)^{\frac{1}{2}} \quad (3.2)$$

where e is the charge on an electron (and also on a singly-ionized particle), T_e and T_i are the electron and ion temperatures, and m and M are the masses of the electron and ion, respectively. For typical semiconductor processing plasmas, T_e is between 1 and 10V (here, temperature and voltage can be considered equivalent through the relation $V = \frac{k_B}{q}T$; therefore, $300K \equiv 0.026V$), while T_i is near room temperature. The ion mass is also much larger than the electron mass. For these two reasons, $v_e \gg v_i$, and during the time immediately after the plasma is ignited, the electrons are lost to the chamber walls much more rapidly than the ions. This leaves the bulk plasma with a net positive charge, which sets up an electric field from the plasma to the walls. This “self-bias” serves to repel further electrons from the walls, and

establishes an equilibrium condition at which the total flux of ions and electrons to the wall is the same. The high electric field region near the walls is called the “sheath”.

In the sheath region, the electric field reflects nearly all of the electrons back into the plasma; therefore, the potential across the sheath is on the order of several T_e . This field also causes ions that enter the sheath to be accelerated across the gap toward the walls. Since the ion temperature in the bulk plasma is low ($\approx 0.026V$), the energy of the ions bombarding the chamber walls is on the order of several T_e . If the wafers to be processed are placed on one of the walls, these ions will strike the wafers with high velocity, and at nearly-normal incidence. This ionic bombardment is the basis for the anisotropic etching that can be provided by a plasma etcher.

Inside a plasma, atoms of the gas are dissociated into many different types of ions and neutrals. Therefore, many species can be generated in a plasma that do not exist under normal conditions; examples include free atomic fluorine or chlorine. This allows many types of processes to be conducted in a plasma, including etching, deposition, and surface treatment. The gas chemistry and the substrate condition determine which process takes place. This aspect of plasma processes is not well understood, mostly because of the complexity and number of possible chemical reactions [15].

3.2.3 Plasma Etch Equipment

To use plasma to process silicon wafers, a plasma reactor must be constructed. There are many choices for geometry, excitation source, chemistry, and several other factors. The more commonly used configurations are described in this section.

Barrel Etch

Barrel etch reactors generate a capacitively-coupled plasma in an annular region surrounding the wafers (see Figure 3.2). A conductive shield keeps the plasma from

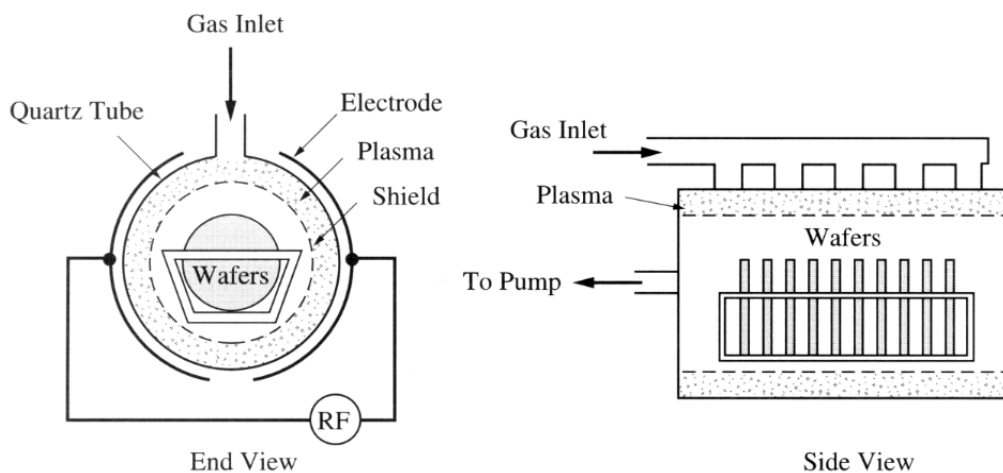


Figure 3.2: Barrel plasma reactor configuration [13].

contacting the wafers directly. Because the wafers are not in contact with any electrodes or the plasma, they are not bombarded by ions; therefore, the etch is isotropic. For this reason, this type of etcher is used primarily to generate etchant species in the plasma. These etchants then diffuse inside the shield and react with the wafers.

Because of the purely chemical nature of the etch process, highly selective etches can be performed using a barrel reactor. However, they typically offer very low across-wafer uniformity, and because the etch is isotropic they cannot be used to print small features. Typical applications include photoresist stripping (using O_2 plasma) and other non-masked stripping operations.

Capacitively Coupled Plasma

Capacitively coupled plasma sources (sometimes called “RF Diodes”) are common in the semiconductor industry. They typically consist of a set of parallel electrodes with a low-pressure gas in the center region (see Figures 3.3 and 3.4). By applying a large radio-frequency (RF) voltage across the plates, an oscillating electric field is produced in the center region. This electric field couples to the plasma electrons, causing them to oscillate; the highest energy electrons then impact the neutral gas

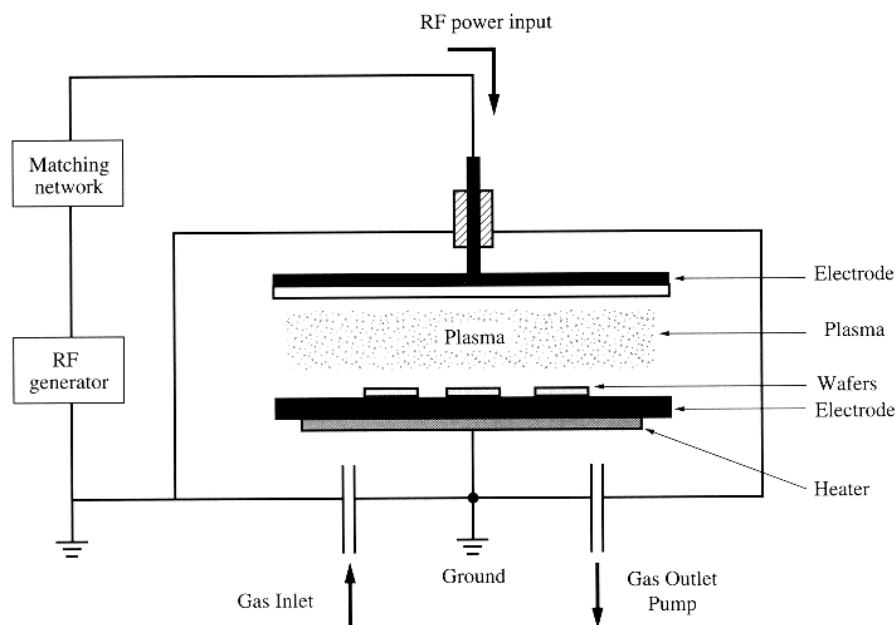


Figure 3.3: Parallel plate capacitively driven plasma reactor configuration [13].

molecules, ionizing them to sustain the plasma.

Since the bulk plasma contains free electrons, its resistance is relatively low compared to the resistive, electron-depleted sheath regions. Therefore, the majority of the total applied voltage is dropped across the sheaths. Further, if one of the electrodes is made to be much larger than the other, then the sheath at the smaller electrode will accumulate a much larger voltage drop, nearly equaling the total applied voltage. For typical parallel plate plasma systems, this drop is several hundred volts peak to peak. Therefore, ion bombardment energies in capacitively driven sources are on the order of hundreds of eV [14].

Another capacitively driven source design is the “hexode” reactor, shown in Figure 3.4. In this design, many wafers are placed at the center electrode, and a concentric outer electrode is used as the other terminal. This design allows a highly asymmetric electrode sizing, with the center much smaller than the outer. Also, many wafers can be processed in parallel, speeding throughput. One disadvantage

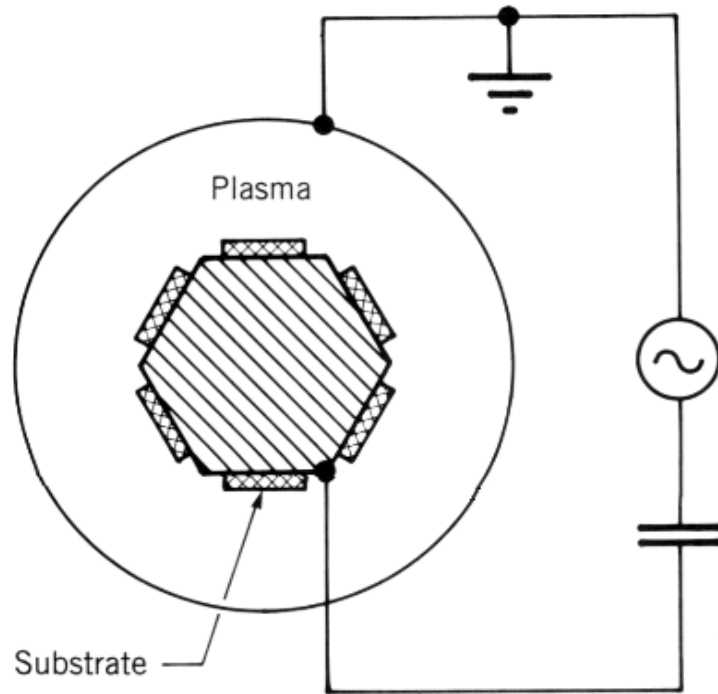


Figure 3.4: Coaxial, “hexode” capacitively driven plasma reactor configuration [14].

of such a multi-wafer system is loss of wafer-to-wafer control, and the corresponding increase in wafer-to-wafer non-uniformity.

Capacitively driven sources in general have several limitations. First, since the applied RF voltage controls both the ion bombardment energy as well as the plasma density, there is no way to independently control these quantities. Increasing the RF voltage increases the drop across the sheath, which raises the bombardment energy; this simultaneously provides more ionization energy to the gas, increasing the plasma density [14]. For some applications, this is a very limiting factor. It might be desirable, for example, to reduce the bombardment energy to avoid damaging sensitive structures, while simultaneously increasing the plasma density to raise the etch rate. For this reason, the semiconductor industry moved away from capacitively coupled systems for the critical etching steps, where uniformity and control are of critical importance.

High Density Plasma

In high density plasma systems, the plasma is excited through non-capacitive means. Because there is no high driving voltage requirement, the sheath potentials can be reduced to their minimum possible value, equivalent to several T_e . To provide independent control of the ion bombardment energy, the wafer electrode can be separately biased using an RF source. This scheme allows the simultaneous production of a high density plasma, while allowing independent bombardment energy control.

Four such methods for plasma excitation are shown in Figure 3.5. In electron cyclotron resonance (ECR) plasma sources, microwave power flows along a DC magnetic field. The magnetic field is made to vary with distance, such that a circularly polarized wave is generated; the frequency of this wave is tuned to match the electron natural frequency (the “electron gyration frequency”) so that maximum power transfer is achieved. In a helicon plasma source, a uniform DC magnetic field and an RF antenna structure are used to excite a so-called “helicon wave”. This wave transfers power to the electrons, sustaining the plasma. Helical resonators use a helical antenna and a conducting cylinder surrounding the chamber to excite an electromagnetic wave in the plasma. Finally, in an inductively coupled plasma (ICP), sometimes called a transformer coupled plasma (TCP), an RF coil antenna couples power into the plasma by transformer action. The plasma acts as a single-turn coil, magnetically coupled to the antenna coil.

As shown in Figure 3.5, most high density plasma sources are constructed as “remote plasmas”, in which the plasma is generated at a distance from the substrate. The products of the plasma or the plasma itself are then allowed to diffuse to the substrate location. This has the advantage that radiation exposure of the substrate due to the plasma generation mechanism is reduced. Because high density sources offer higher plasma density, the gas pressure can be correspondingly reduced while still maintaining a high etch rate. With lower pressure, higher etch directionality can be achieved due to fewer ionic collisions within the sheath.

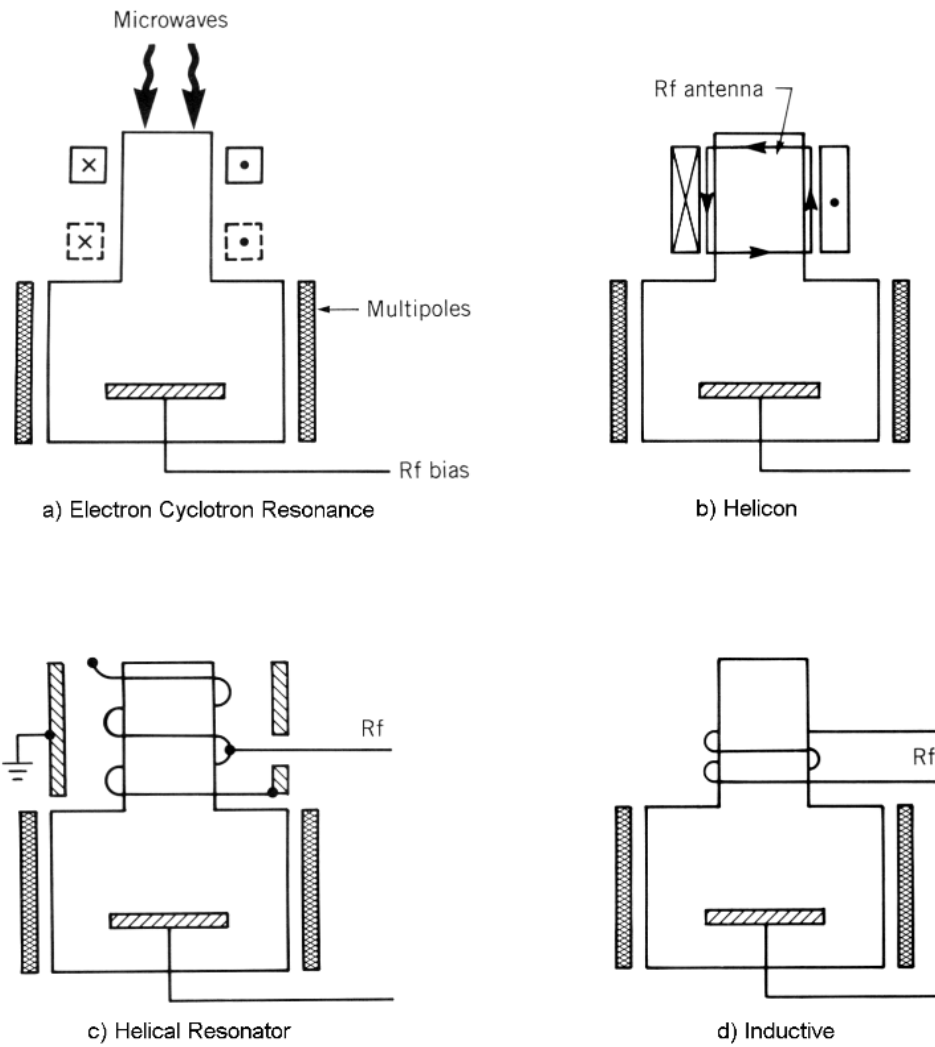


Figure 3.5: High density plasma source configurations [14].

3.2.4 Associated Problems

The primary concern with plasma reactors is ensuring uniformity of the etch across the wafer surface [13]. Differences from location to location can cause device failure and increased product spread, both of which reduce overall yield. As wafer sizes get larger, this task becomes even more daunting. In addition, next generation processes contain more and more etch steps, primarily due to the increased number of metal and dielectric layers used.

The industry shift to single-wafer systems has allowed better control of each wafer, but tight control of plasma uniformity, gas flows, and wafer temperature are still difficult problems [13]. In any etch process, there must be careful control of etch rate, selectivity, and anisotropy, while at the same time minimizing surface damage, particulate formation, and etch residue formation. It is generally not possible to optimize all of these parameters at the same time: there is an inherent tradeoff. For example, it is possible to increase the chemical nature of the etch, which will increase the selectivity but decrease the anisotropy.

In order to control the uniformity of various etch parameters, spatially-resolved measurements of these parameters must be made. However, as discussed in Chapter 2, this type of measurement is sometimes difficult or impossible. In addition, detailed plasma reactor models are required to make effective use of the data from a process sensor. In order to build these complex models, very detailed measurements of a test process must be made, so that comparisons with the model can be performed.

3.3 Importance

In general, there are four categories of semiconductor process: deposition, doping, photolithography, and etching. All are critically important, and each requires tight process control. Some processes have more variables that require measurement than others, and some processes are more amenable to the application of sensors than

others. For example, in CVD processes there is typically no direct optical access, limiting the use of traditional optical film thickness metrology.

In particular, plasma processes are well suited for novel sensor development, because they are complex processes requiring detailed measurement and they typically contain few if any wafer-state measurement sensors. Also, plasma processing takes place in harsh environments precluding the use of most other types of sensors.

3.3.1 Many Variables to Measure

Plasma processes involve many different factors which affect the processing of the wafer (see Figure 3.6). Some of these quantities, such as excitation power, gas pressure, and pumping speed, are easy to measure externally. Sensors for these quantities are typically built into most plasma processing equipment. However, others such as wafer surface temperature, surface potential, and ion current, are much more difficult to measure from outside the chamber. In addition, these quantities must be measured at the wafer surface, because measurements at the chamber sidewall or on a bare chuck are crude approximations to those at the wafer surface. Therefore, there are many opportunities to develop new on-wafer sensors that can measure quantities of interest.

3.3.2 Complexity

Plasma processes are among the most complicated semiconductor processes in use [12]. A multitude of factors interact in subtle ways, and most of these interactions affect the processing of the wafer. This makes control of the tool difficult, which therefore makes process state measurement critical. Also, these processes are still not completely understood, and development engineers would like better measurements in order to create better plasma process models. For these reasons, plasma is a good process for which to target novel sensor development.

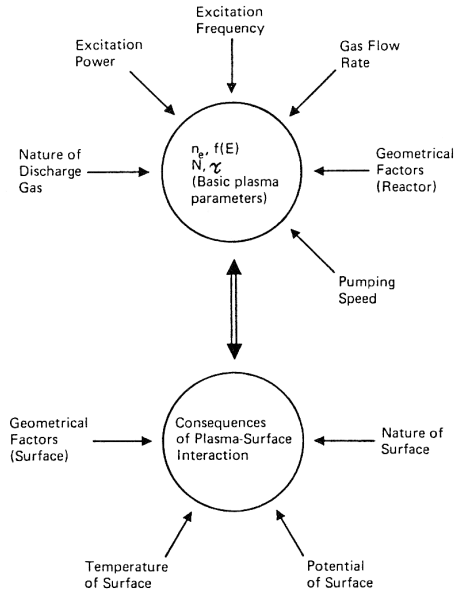


Figure 3.6: Variables affecting the operation of a plasma [16].

Because plasma processing is so complex, a substantial amount of work has been conducted into diagnostics [17–22]. All of these methods require sensor data, and the more data available, the better they perform. Therefore, it is desirable to fabricate sensors for the plasma process.

3.3.3 Harsh Environment

One difficulty presented by plasma processes is that they tend to be very harsh environments. The primary issue is that typical processing plasmas are electrically excited by radio frequency (RF) or microwave radiation. As a result, there is significant electrical interference present inside the chamber. Any wires that connect sensors on the wafer to the outside world will function as antennas, channeling this electrical noise out of the chamber. In addition, since the wires will carry significant electrical energy out of the chamber, it is very possible that the process will be changed by the presence of the wires, making the measurements suspect. Another issue is that

semiconductor plasma processes are always run at low pressures, which means that any wired connections to the wafer must pass through a vacuum feedthrough. Some chambers come with such feedthroughs installed, but others require the user to drill a hole in the chamber wall to install one. For these reasons, plasma processes are an important place where wireless sensor wafers are necessary.

3.3.4 Suitability for Wafer-Mounted Sensors

For the reasons described in this section, plasma processes provide an interesting testbed for the application of the wireless sensor wafer concept. There are a number of suitable sensors that can be fabricated (as described in Section 3.5), and in several cases wireless sensors of this type are the only option. Therefore, we have decided to pursue the construction of several sensors for use in plasma etching environments.

3.4 Challenges

There are many challenges associated with the construction and operation of a wireless sensor wafer inside a plasma process. First, plasma processes are very harsh environments which tend to interfere both physically and electrically with the sensor wafer. Second, typical plasma chambers are made almost entirely of metal. This makes the transmission of sensor data, whether by optical or electromagnetic means, difficult. Finally, as described in Section 3.2.4, chamber contamination must be kept to a minimum. Therefore, sensors and electronics must be properly shielded to avoid particle generation or outgassing.

3.4.1 Harsh Environment

Plasma process tools present a rather harsh environment to the wafer. First, these machines are designed to etch material from the wafer, which means that the

sensor wafer's sensors, electronics, communication system, and power supply must be properly shielded from both physical bombardment and chemical attack. While this can typically be done quite easily for the electronics and power supply (through encapsulation in an inert material), it may be more difficult for the communications system or the sensors themselves. For example, if the sensors consist of exposed resonator structures, they must be properly designed so that they are not destroyed by chemical attack.

In addition to this problem, plasmas typically use electromagnetic waves as an excitation source. The chamber is designed to shield the outside environment from this electromagnetic interference, but this is not true for the inside of the chamber. Therefore, all wafer-mounted components must be properly shielded from RF and microwave interference, to avoid data corruption by noise.

3.4.2 Difficult communications

Because typical plasma chambers must operate at low pressures, and must provide adequate shielding of the outside environment from the plasma, they are usually almost fully enclosed in metal. This metal shielding effectively blocks most electromagnetic communications schemes. In addition to the metal chamber walls, the plasma itself forms a low-resistance conductor surrounding the wafer, which further blocks RF communication techniques.

One alternative to electromagnetic transmission is the use of high-frequency (10 Mhz) acoustic data transmission. With this scheme, a piezoelectric or MEMS-based actuator on the wafer generates sound waves in the wafer. Because the chamber is at low pressure, these waves are highly damped during travel through the gas inside the chamber. However, the waves can easily travel downward into the metal chuck, and can be conducted to the outside world through the mechanical components of the etcher. A "listening" device placed in physical contact with the etcher on the outside would then be able to detect and decode the data being transmitted.

Some chambers include a small viewport window (approximately 2 inches by 8 inches on a Lam 9600 plasma tool), which allows optical access to the wafer. This window is typically used for optical emission spectroscopy (OES), which the tool uses for endpoint detection. This window could also be used by a sensor wafer for optical communications, using, for example, an infrared light emitting diode (Ir-LED). In this case, an infrared detector with a focusing lens would be placed just outside the viewport window to detect the transmitted sensor data. One problem with this technique is that a viewport is not present on all chambers, nor is it positioned in the same manner on each chamber. These facts make line-of-sight optical communications difficult. The lack of a viewport completely precludes the use of optical communications. Even if such a viewport is present, the transmitter must either be unidirectional, so that wafer orientation does not matter, or it must be directed in a machine-specific direction, so that it points toward the viewport while inside the chamber.

3.4.3 Contamination

It was stated in Section 3.4.1 that the wafer-mounted sensor system must be properly isolated from the harsh plasma environment, to avoid damaging the wafer. Conversely, this isolation must also be designed to safely isolate the *process* from the *wafer*. A wafer-mounted sensor system like the one described here would contain many non-standard components, such as electronics, sensors, power supplies, etc. Many of these components contain materials that are detrimental to CMOS circuit operation. For example, any solder present in the electronics would contain lead and tin, both of which function as recombination centers in IC circuits, damaging circuit performance. For this reason, great care is taken in high-volume production facilities to minimize the presence of these types of material. Therefore, if a wafer containing these materials is to be used in production process tools, the wafer must contain adequate isolation from both physical and chemical attack, to avoid the release of these materials into

the chamber. As described in Section 3.4.1, this can be a challenge for some types of sensors or communication systems, especially if these systems require exposure to the plasma environment in order to function.

3.5 Sensor Choice

There are many quantities of interest in plasma processes. Quantities that might be measurable with the integrated sensor wafer concept include etch rate, selectivity, anisotropy, gas pressure, wafer temperature, ion flux, electron flux, plasma density, ion energy distribution function (IEDF), electron energy distribution function (EEDF), electron temperature, and ion temperature.

All of these variables are useful for plasma modeling; however, some are more useful than others for equipment design, production process control, and equipment problem diagnosis. For these applications, the most useful quantities are those that directly affect the end product.

3.5.1 Etch Rate

The primary goal of a plasma etch tool is to provide rapid, uniform etching. Therefore, the most direct quantity that can be measured is the etch rate itself. The ability to take spatially resolved measurements of the actual surface etch rate would be a valuable tool for the industry. In addition, a sensor capable of this measurement could be used to characterize not only the etch rate, but also the selectivity and uniformity of the process.

For this reason, a wafer-mounted etch rate sensor will be explored in this research. Because the polysilicon gate etch process is one of the most crucial, and also difficult, etch processes in use [1], the etch rate sensor will be constructed for this etch process. Specifically, the sensor will consist of a film of polysilicon whose thickness can be rapidly and accurately measured. In this way, as the film is etched, its thickness will

change, and the etch rate can be inferred. This sensor is described in more detail in Chapter 4.

3.5.2 Thermal Flux

Monitoring systems for plasma etch processes often include temperature measurement sensors. Silicon wafers instrumented with temperature sensors and a tether for data transfer are often used to diagnose equipment problems, or to help equipment designers optimize the chamber geometry [9]. Temperature labels are used to detect the peak temperature experienced by the wafer at different locations. However, all of these measurements only detect the end-result of a problem: non-uniform heat delivery to or removal from the wafer. By instead directly measuring the thermal flux to the wafer surface, non-uniformities can be much better characterized and diagnosed. If the thermal flux sensor further discriminates between different modes of heating, even more information can be extracted from the process.

Another motivation for the construction of a wafer-mounted thermal flux sensor relates to the construction of plasma models. To accurately generate and validate plasma models that incorporate wafer temperature and heating effects [23, 24], measurements of these quantities must be available.

For these reasons, a wafer-mounted thermal flux sensor will be developed for this research. This sensor will be able to measure the heating effects due to ionic heating separately from that due to surface chemical etch reactions. This sensor is described in more detail in Chapter 5.

3.6 Summary

In this chapter, a plasma etch background is presented. Following this, the difficulties associated with the real-world application of plasma processing are listed, including problems related to the measurement of internal variables. Next, a motiva-

tion is given for the use of wireless sensors in plasma etch processes. The next section discusses the challenges inherent in the application of the wafer-mounted sensor concept to these processes. Finally, a motivation is given for the particular choice of two sensors for this research. The next two chapters discuss these sensors in more detail.

Chapter 4

Etch Rate Sensor

4.1 Introduction

This chapter describes the design, fabrication, and testing of a polysilicon film thickness sensor, to be used as an etch rate sensor in polysilicon etch processes. The sensor is designed for easy electrical interrogation, and it also contains an additional temperature sensor to compensate for thermally generated errors.

The remainder of this chapter is organized as follows. First, a motivation is given for the construction of a film thickness sensor. Next, a brief overview of research related to this type of sensor is discussed. Then, the available film thickness sensing methodologies are presented, and a particular choice for this project is made. Finally, experimental results gathered using several sensor prototype designs are presented.

4.2 Motivation

In an etch tool, there are three primary parameters of importance: overall etch rate, uniformity of etch, and selectivity. There are, of course, many other interesting quantities, but these are of secondary importance. Equipment designers need to measure these quantities as a function of chamber geometry and other design factors,

so that they can optimize the machine to produce highly uniform, highly selective, rapid etching.

Once the equipment is designed, process developers need to optimize the process flow for their technology. Because they are again mostly concerned with etch rate, uniformity, and selectivity, they would like to use measurements of these quantities to build a process model or response surface. This model can then be used to design optimal process recipes.

Finally, production managers have the responsibility for ensuring that the production process stays within control and within specifications. By measuring these primary output variables, they can more easily keep control charts of these quantities, thereby allowing faster response to out-of-control conditions.

The ability to directly measure the thickness of a film as it is being etched would allow the measurement of all three important quantities: uniformity, selectivity and etch rate. Such a sensor would directly allow the measurement of etch rate, by finding the derivative with respect to time of the film thickness. A measure of uniformity could be calculated by finding the variations among an array of such sensors, spread across the wafer surface. Finally, selectivity could be measured by fabricating several such sensors onto a single wafer, each using different materials for the film being etched, and then finding the difference in etch rate between the materials.

Currently, the primary method of assessing the spatially-resolved etch rate is to pattern a nearly-blank wafer (a “test wafer”) using the etch tool, measure the total etched film thickness, and then divide by the total etch time [25]. However, because this only measures the time-averaged etch rate, all time-related information is lost. For example, a steady increase in the etch rate over time due to wafer heating will be hidden with post-process measurement. Similarly, if the uniformity decreases as the etch proceeds, test wafers will not detect this effect.

For these reasons, we would like to fabricate a film-thickness sensor on the surface of a wafer, for use inside semiconductor etch processes.

To successfully fabricate an etch rate sensor onto a standard silicon wafer, several characteristics would be essential. First, because the sensor is directly sensing etch rate, it necessarily gets etched by the process. To be useful, the sensor must have enough thickness to “survive” at least one process cycle, perhaps lasting through about one minute of continuous etching. The second requirement is that the sensor wafer should behave like a regular wafer from the machine’s perspective. This means that the pattern density, total wafer open area, pattern uniformity, etc. should be as close as possible to the “real” product wafers that the machine regularly processes. The reason for this is that common etch processes are very sensitive to loading, i.e. the quantity and distribution of material being etched has an effect on the etch process. Therefore, if the data from the sensor-wafer are to be compared to the conditions experienced by standard product wafers, the etch loading should be similar in both cases.

4.3 Related Research

Many types of film-thickness / etch-rate sensors have been developed. However, each of these designs require modifications to be made to the process chamber. For example, a novel resonance-based etch-rate sensor was described in [26], but this sensor requires wires to be passed through the wafer chuck, fed through the vacuum system, and connected through a vacuum feedthrough to the outside of the equipment. Other techniques involving non-contact optical measurement have been developed [27–30]. These techniques require direct optical access to the wafer surface, which is not available in many commercial process chambers. Finally, there is a wide variety of sensors that are designed to measure *process-state* variables [21, 31, 32], which are only indirectly related (through process models) to the *wafer-state* variables of interest.

4.4 Design Issues & Choices

There are a number of measurement techniques that allow the measurement of film thickness, and several of these methods would be applicable to this type of on-wafer sensor. These alternatives are discussed in the sections below.

4.4.1 Mechanical Techniques

Most oscillating structures, to first approximation, can be modeled by the second-order differential equation,

$$\ddot{y} + 2\zeta\omega_n\dot{y} + \omega_n^2y = 0 \quad (4.1)$$

where y is the displacement of the structure, ω_n is the undamped natural frequency, and ζ is the damping ratio. For an underdamped oscillatory structure ($\zeta < 1$) governed by Equation 4.1, the position versus time is given by,

$$y(t) = A_0e^{-\zeta\omega_n t} \cos(\omega_d t - \phi) \quad (4.2)$$

where ω_d is the damped oscillation frequency, defined as,

$$\omega_d = \sqrt{1 - \zeta^2}\omega_n \quad (4.3)$$

Note that the frequency of oscillation depends on both the natural frequency and the damping present in the system.

Based on Equation 4.2, several film-thickness measurement methodologies are possible. For example, a cantilever beam fixed at one end and free to oscillate at the other is governed by Equation 4.1, with ω_n given by,

$$\omega_n = \sqrt{\frac{K_{\text{eff}}}{M_{\text{eff}}}} \quad (4.4)$$

where K_{eff} and M_{eff} are the effective spring constant and mass of the cantilever. The equation for K_{eff} can be determined exactly for a cantilever of width w , height h , length L , and elastic modulus E , while the effective mass can be determined up to a proportionality constant that depends on the oscillatory mode shape [33],

$$K_{\text{eff}} = \frac{12EI}{L^3} = \frac{Ewh^3}{L^3} \quad (4.5)$$

$$M_{\text{eff}} = \alpha\rho whL \quad (4.6)$$

where ρ is the mass density, and $0 \leq \alpha \leq 1$ depends on the mode shape. Putting Equations 4.5 and 4.6 together with Equation 4.4, we get,

$$\omega_n = \sqrt{\frac{\frac{Ewh^3}{L^3}}{\alpha\rho whL}} = \sqrt{\frac{Eh^2}{\alpha\rho L^4}} = \frac{h}{L^2} \sqrt{\frac{E}{\alpha\rho}} \quad (4.7)$$

The natural frequency of the cantilever beam depends on the height, length, and material properties of the beam. Therefore, any changes in these parameters, in particular the thickness h , will cause a shift in the oscillation frequency of the cantilever. This assumes, however, that the damping ratio, ζ , stays constant. If, for some reason, the damping ratio is also proportional to the etch depth, then Equation 4.3 shows that the damped oscillation frequency can stay constant. However, in most cases, the damping ratio is a function of the distance between the beam and the support, the width of the beam, and the atmosphere in between the two (so-called “squeeze-film damping”) [34].

Small beams of this type are commonly constructed out of quartz crystals, with piezoelectric transduction of the crystal motion, for use in evaporative deposition systems. In this application, the material being deposited is also deposited on a sacrificial quartz beam, so that the *increased* beam thickness changes the natural oscillating frequency. Such sensors can be extremely sensitive, because they are interrogated by measuring a frequency, which can be measured with *very* high precision ($\pm 0.0001\%$). The downside of using such a technique for an on-wafer sensor is that the oscillator

structure and associated drive and sensing elements must be fabricated onto the wafer. Because the oscillator extends up off the wafer surface and is vibrating, etch-rate is likely to be affected by the sensor itself.

4.4.2 Optical Techniques

Several optical thickness measurement techniques are in widespread use in the semiconductor industry. These include reflectometry, ellipsometry, and scatterometry. Of particular relevance to our discussion is reflectometry, which is described below.

A reflectometer illuminates the film at normal incidence with a light source, and measures the reflected intensity at either a single wavelength or at many wavelengths. If a single wavelength is used for an etching process, then the reflected intensity will vary in a sinusoidal manner, due to the alternating constructive and destructive interference from the etched layer. By measuring the time between maxima and minima, and taking the etched distance during this period to be one-half of the illumination wavelength, an approximate etch rate during the period can be deduced. In addition, if the layer's initial thickness is known, the overall layer thickness versus time can be approximated by integrating the etch-rate. This method has modest accuracy which is proportional to the wavelength of light used [35], but can handle a wide range of thickness values (typically between 200\AA and $15\mu m$) [36].

When multiple wavelengths are used, a reflectivity versus wavelength plot is generated by the system at each time instance. By using an optical model of the film stack under observation, thickness parameters in the model can be estimated using the reflectance versus wavelength data. In this way, an absolute thickness can be measured at each time, and the etch rate can be calculated by differentiating these results with respect to time. This technique provides much higher film-thickness measurement accuracy over a wide range of thickness values (typically between 200\AA and $15\mu m$) [36].

There are also several other optical thickness measurement systems, including

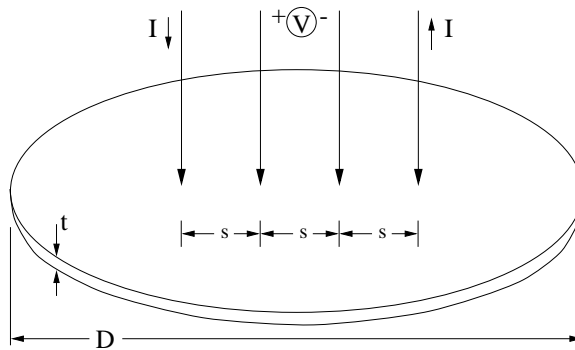


Figure 4.1: Collinear four-point probe arrangement. Note that $D \gg s$.

ellipsometers and scatterometers. However, all such systems (including the reflectometer) would be practically impossible to implement for an on-wafer sensor, since all require equipment (the light source and light sensor) external to the wafer being measured.

4.4.3 Electrical Techniques

An alternative scheme for measuring physical dimensions of conductive structures is to use electrical test structures. These structures measure the resistance of a structure, and deduce one of its dimensions from knowledge of its other dimensions and its material properties. One example of such a structure, which is commonly used in the semiconductor manufacturing industry, is the four-point probe. Consider an isotropic sample of material with constant resistivity ρ_e . If four electrical probes are contacted to the surface in a linear arrangement, and a current I is forced into and out of the outer two probes, then the voltage measured across the inner two probes can be shown to be (see [37] and Appendix A for more detailed four-point probe analysis),

$$V = \frac{\rho_e I}{2\pi F} \left(\frac{1}{s_1} + \frac{1}{s_3} - \frac{1}{s_2 + s_3} - \frac{1}{s_1 + s_2} \right) \quad (4.8)$$

where F is a unitless correction factor that accounts for the configuration of the

probes, and s_1, s_2 , and s_3 are the three distances between the four probes. The factor F in Equation 4.8 corrects the equation for deviations from the ideal geometry, which is a slab with an infinite planar surface, and infinite depth. Typically, the sample consists of a thin film of material (thickness t) on top of an insulating surface (see Figure 4.1). For this geometry, with uniform probe spacing ($s_1 = s_2 = s_3 = s$), $F = \frac{t}{2s \ln(2)}$, and Equation 4.8 can be rearranged to solve for the thickness, t ,

$$t = \frac{\ln(2)\rho_e I}{\pi V} \quad (4.9)$$

This equation relates the layer thickness to the measured voltage, the sourced current, and the resistivity of the material. While the material resistivity must be known in order to use this equation, it does not have to be measured directly. If an alternate film thickness measurement method is available, the measured film thickness can be substituted into Equation 4.9 to deduce the resistivity ρ_e . This sensor “calibration” need only be performed once, assuming the resistivity is stable with time.

A disadvantage of the four-point probe method is that it requires a large sensor area to approximate the semi-infinite sheet assumption. A slightly different technique was proposed by van der Pauw [38], in which a finite slab of material is probed at four points on the edge (see Figure 4.2). With this configuration, it can be shown that the sheet resistance of the layer can be found by making two sets of voltage/current measurements, with different probes used as current and voltage in each. In this case, the sheet resistance is given by the solution of [39],

$$\exp\left[\frac{-\pi t}{\rho_e}\left(\frac{V}{I}\right)_1\right] + \exp\left[\frac{-\pi t}{\rho_e}\left(\frac{V}{I}\right)_2\right] = 1 \quad (4.10)$$

where $\left(\frac{V}{I}\right)_1$ and $\left(\frac{V}{I}\right)_2$ are the values from the first and second measurement set, respectively. If a cylindrically symmetric structure is used, and the probes are equally spaced, then $\left(\frac{V}{I}\right)_1 = \left(\frac{V}{I}\right)_2$, and Equation 4.10 can be re-arranged as,

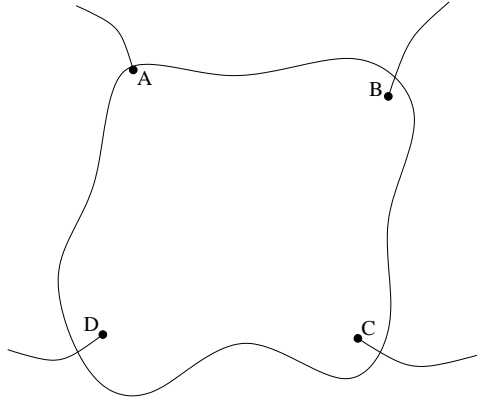


Figure 4.2: Generic van der Pauw sheet resistance measurement structure.

$$t = \frac{\ln(2)\rho_e}{\pi} \frac{I}{V} \quad (4.11)$$

Note that this is identical to Equation 4.9. The main assumption used to derive Equation 4.11 is that the probe size is much smaller than the overall dimension of the structure. Therefore, if suitably small contacts to the structure can be fabricated, then the overall size of the structure has no lower limit.

Accuracies for these types of electrical measurement techniques depend on the fidelity of the current sourcing and voltage measurement, and also on the position and layout uncertainty for the probes. Thickness accuracies on the order of $3nm$ can be achieved, and the overall accuracy is primarily determined by the current and voltage measurement system used [40].

4.4.4 On-Wafer Sensor Choice

For the wafer-mounted film thickness sensor design, we selected the electrical test structure because of its accuracy, simplicity, and robustness. Specifically, a square van der Pauw structure was used, and this design is shown in Figure 4.3.

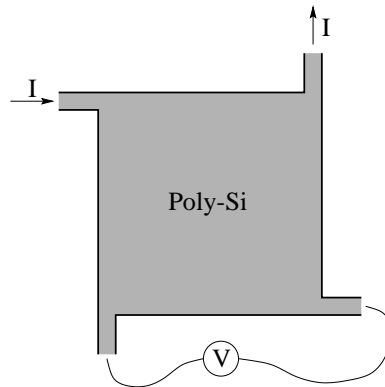


Figure 4.3: van der Pauw sheet resistance measurement structure.

4.5 Results

Several polysilicon van der Pauw film-thickness sensors have been fabricated and tested. Figures 4.4, 4.5, 4.6, and 4.7 show the various versions of etch rate sensor wafers that were made. Several modifications and improvements were made to the film thickness sensor process with each iteration, and reasonable accuracies, repeatabilities, and other gauge factors were measured for the final design. The calibration and testing of the final design is discussed in the sections below.

4.5.1 Process Flow

The process shown in Figure 4.8 was used to fabricate the final version of the polysilicon van der Pauw film thickness sensors. This process is designed to allow the fabrication of not only the polysilicon sensor structures, but also complex aluminum interconnections with over-crosses, and solderable nickel bond pads.

4.5.2 Temperature Compensation

In deriving Equation 4.11 as a method for measuring film thickness, it was assumed that the material resistivity was not only known, but was constant during

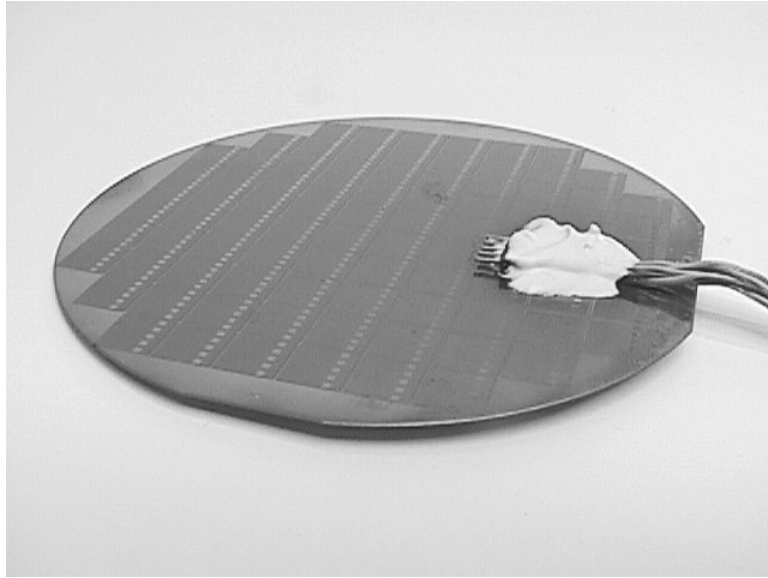


Figure 4.4: Etch rate sensor wafer design #1, with electrical connections glued to the surface.

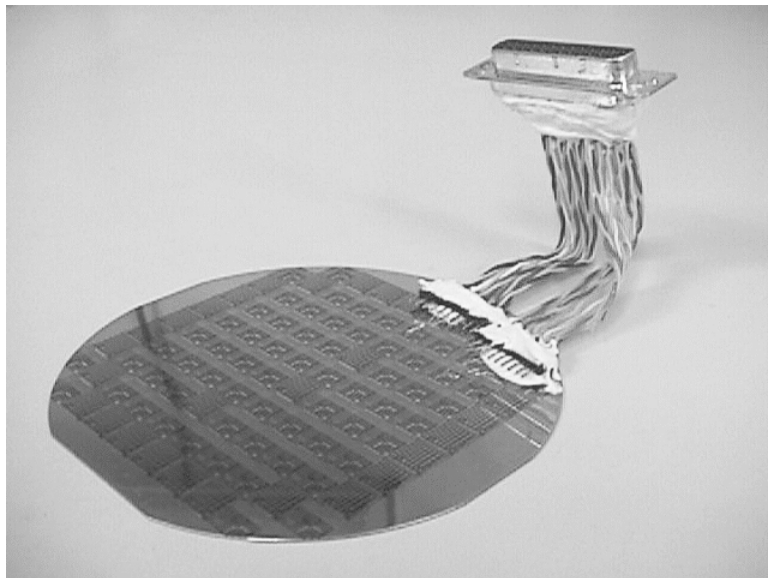


Figure 4.5: Etch rate sensor wafer design #2, with electrical connections glued to the surface.

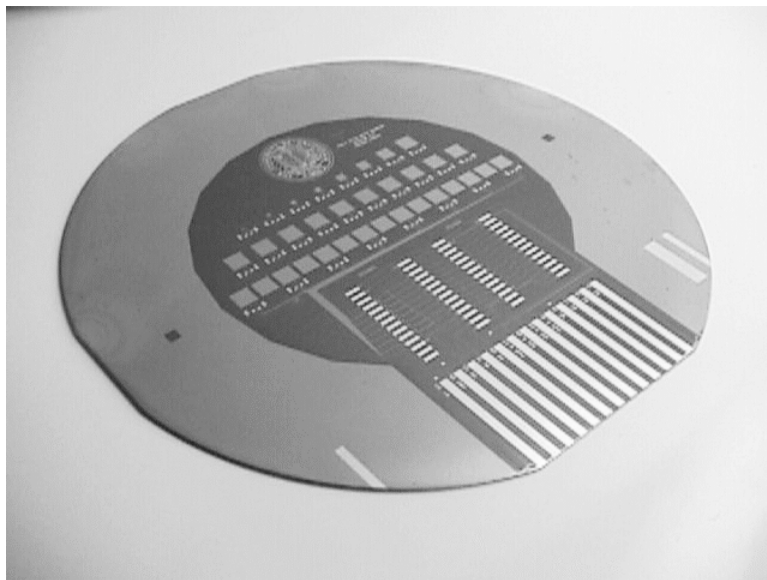


Figure 4.6: Etch rate sensor wafer design #3.

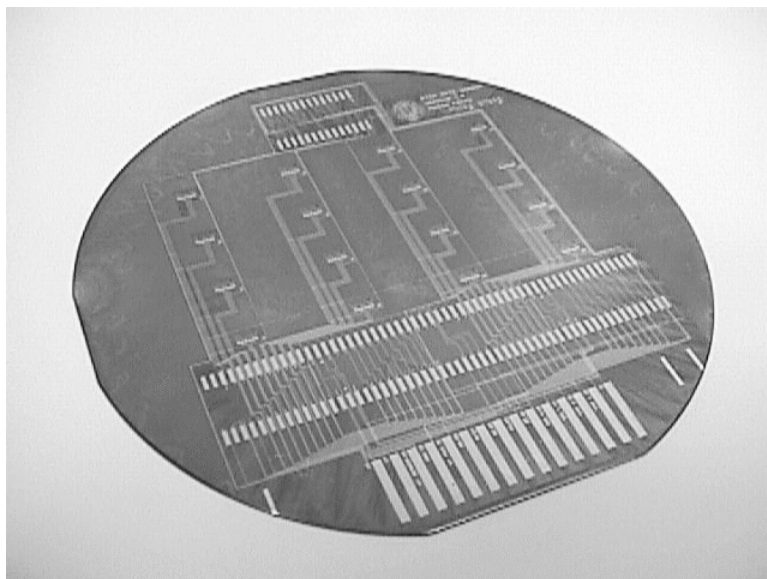


Figure 4.7: Etch rate sensor wafer design #4.

1. Start with $\langle 100 \rangle$ test-grade wafers
2. Grow 3000Å wet oxide
3. Deposit 8000Å n+ doped poly (sheet resistance $\approx 20 \frac{\text{ohm}}{\text{sq}}$)
4. Anneal poly
5. Pattern with POLY mask
6. Wet polysilicon etch in 64% HNO_3 /33% H_2O /3% NH_4F
7. Sputter 8000Å of Al-2%Si
8. Pattern with METAL1
9. Wet aluminum etch in 80% H_3PO_4 /10% H_2O /5% CH_3COOH /5% HNO_3
10. Apply 10000Å spin-on-glass
11. Anneal SOG
12. Pattern with VIA
13. Plasma etch SOG using $CHF_3/CF_4/He$ chemistry
14. Sputter 8000Å of Al-2%Si
15. Sinter aluminum
16. Sputter 3000Å of Ni
17. Pattern with METAL2
18. Wet nickel etch in 50% HF /50% HNO_3
19. Wet aluminum etch in 80% H_3PO_4 /10% H_2O /5% CH_3COOH /5% HNO_3

Figure 4.8: Simplified fabrication process for polysilicon van der Pauw sensor wafer (see Appendix B for full process).

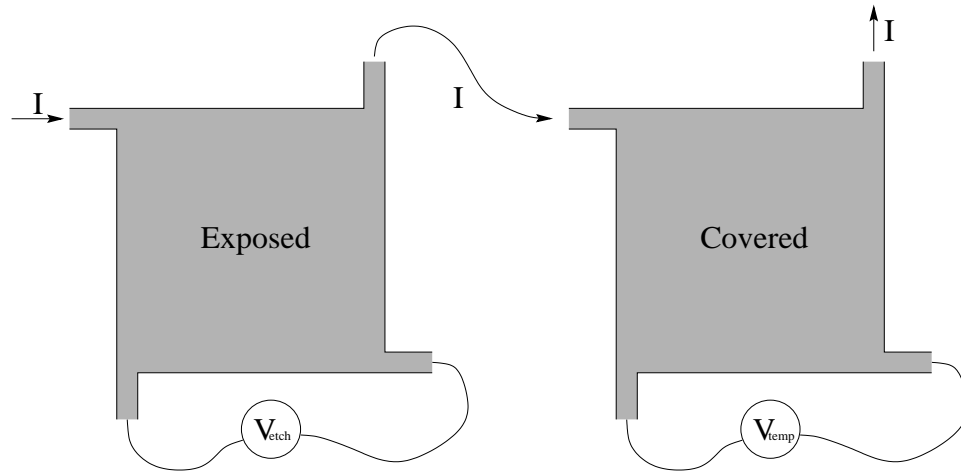


Figure 4.9: Dual van der Pauw sensor arrangement allowing simultaneous measurement of film thickness and temperature

measurement. However, the resistivity of polysilicon changes with temperature [41]. While the change in resistance may not be very large, it will significantly affect the accuracy and repeatability of the sensor output. Further, since most etch reactions are either exothermic or endothermic, it is very likely that temperature changes will occur during the etch process. Therefore, it is critical to compensate for this effect.

For temperature compensation, an identical but buried van der Pauw structure was added next to each film thickness sensor. Because this structure is buried, it does not get etched by the process. It can therefore be used to measure the wafer temperature and deconvolve the effects of temperature change and film etching. Figure 4.9 shows this dual-sensor arrangement. Section 4.5.5 discusses experimental verification of this temperature compensation technique.

4.5.3 Experimental Technique

To test the etch rate sensors, an XeF_2 etch system was utilized. XeF_2 is an isotropic, gaseous, non-plasma, silicon etchant. Because it is not a plasma-based system, there is no need to shield the sensor or electronics from electrical interference or physical attack. Further, because it is highly selective, it only etches the silicon

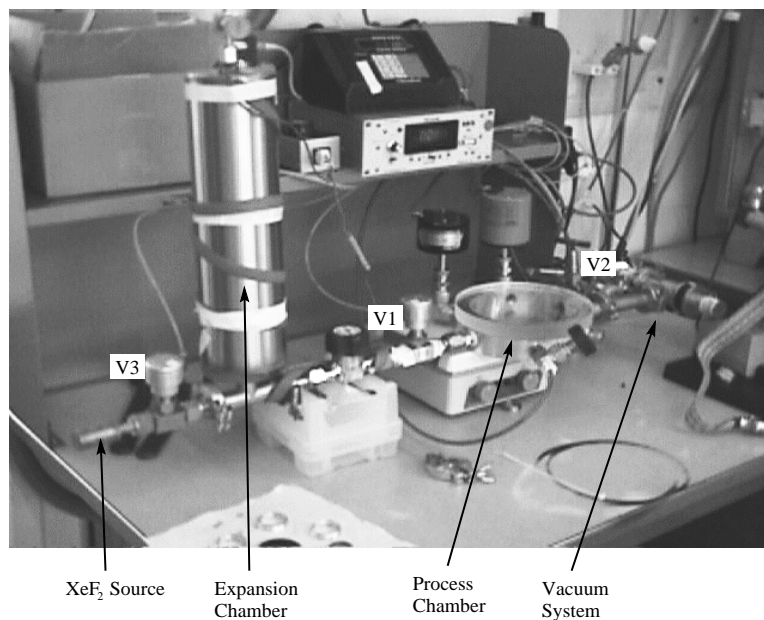


Figure 4.10: Photo of XeF_2 etching system used for etch rate sensor testing.

structures, leaving the interconnections and supporting substrate intact. XeF_2 is a white crystalline solid at room temperature, with a vapor pressure of 2.7 Torr. For use in etching, it is necessary to pump an “expansion” chamber down to $\approx 0.3T$, expose the XeF_2 solid to this chamber, and allow XeF_2 gas to sublime into the chamber. Then, the substrate to be etched is exposed to the sublimated gas.

The XeF_2 etching system used for this sensor testing (shown in Figure 4.10) consists of a small XeF_2 source bottle, an expansion chamber, a processing chamber (holding the substrate), and a vacuum system. Three pneumatic valves control the flow of gas: V3 is between the XeF_2 source bottle and the expansion chamber, V1 is between the expansion chamber and the processing chamber, and V2 is between the processing chamber and the vacuum pump. To perform an etch, the three valves are controlled to introduce a volume of XeF_2 gas into the chamber, allow it to etch for a period of time (typically ≈ 30 seconds), and pump it back out. The processing chamber is a circular aluminum dish with a clear Plexiglas lid.

To make electrical connections to the wafer, the first versions of the sensor wafers

used permanent wired connections. This was done by either gluing wires to the surface of the wafer and then using an ultrasonic wirebonder to bond between the ends of the wires and the bond pads on the wafer (see Figures 4.4 and 4.5), or by directly soldering wires to nickel bond pads on the wafer. Because both methods are fairly time-consuming, a novel “clip-on” method was developed. Using this method, a row of metal strips is patterned on the wafer, with the strips leading to the edge of the wafer. The pitch and dimension of each strip is made to match that of a plastic “edge-board” connector. By selecting the appropriate connector dimensions, the edge of the wafer can simply be slid into the connector, making up to 15 parallel electrical connections at once. A photo of a wafer using this scheme is shown in Figure 4.11.

Because the XeF_2 etch system is simple and compact, electrical connections were easy to make. An alternate Plexiglas lid was fabricated that contained a vacuum-tight electrical feedthrough for 25 wires (Figure 4.12 shows a photo of this setup). This allowed the electrical signals to be brought outside the chamber for analysis. For this purpose, the signals were connected to a computer with a National Instruments AT-MIO/64-E3 data acquisition system, which allowed the system to automatically digitize measurements and record them.

4.5.4 Calibration

Before the sensors were used in an etch process, they were first calibrated. The actual thickness of the film thickness sensor was measured, as were the temperature response characteristics of the temperature sensor.

The actual thickness of the sensors was measured using a NanoSpec / AFT reflectometric film thickness measurement station. They were then attached (on the benchtop) to the data acquisition system and measured electrically. The measured thickness value (t_{measured}) and the measured current and voltage (I and $V_{\text{thickness}}$, respectively) were used to deduce the sensor resistivity via the van der Pauw equation as,

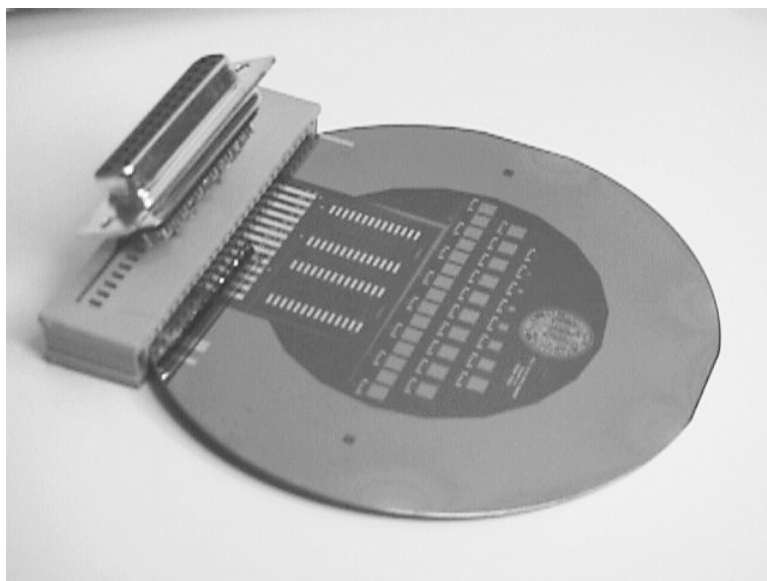


Figure 4.11: Photo of edgeboard connector attached to sensor wafer.

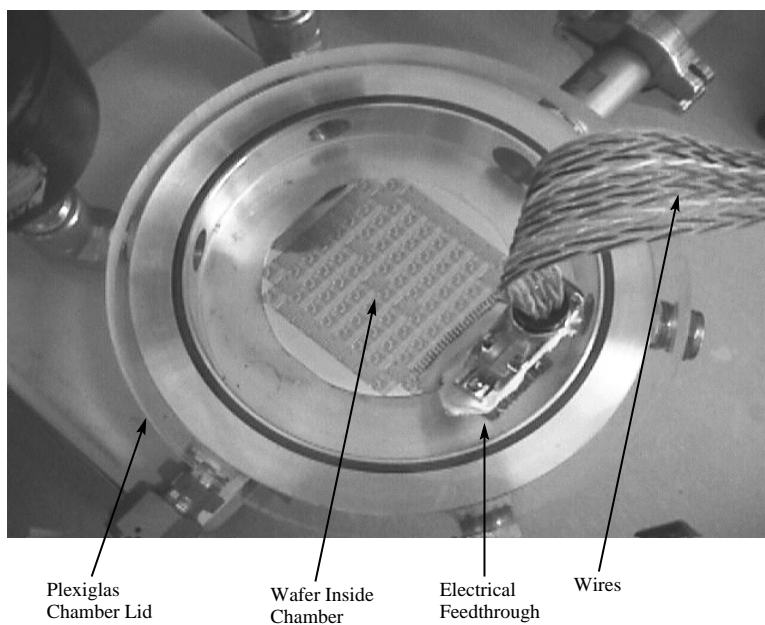


Figure 4.12: Photo of XeF_2 chamber with electrical feedthroughs and sensor wafer in place.

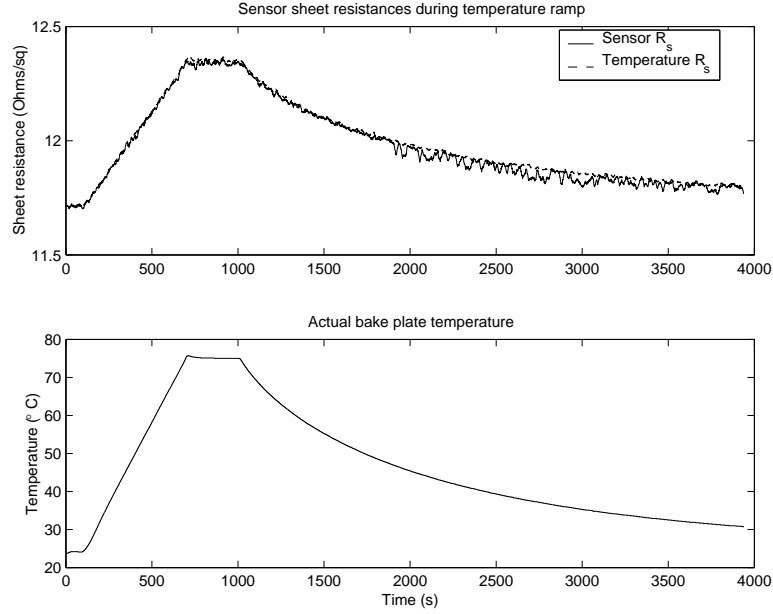


Figure 4.13: Plot of data from thermal calibration of etch rate sensor. The top plot shows the sheet resistances measured by the film thickness sensor and temperature sensor, and the lower plot shows the measured bake plate temperature.

$$\rho_{e,\text{sensor}} = \frac{\pi t_{\text{measured}} V_{\text{thickness}}}{\ln(2) I} \quad (4.12)$$

To calibrate the temperature sensor, the wafer was placed onto a computer-controlled bakeplate. The temperature of the bakeplate was slowly increased, and the sensor current and voltage as well as the bakeplate temperature were recorded by the computer. By using Equation 4.11 with the value for $\rho_{e,\text{sensor}}$ calculated above, the sheet resistance of each type of sensor can be found. A plot of the sensor sheet resistances and actual bakeplate temperatures is shown in Figure 4.13. Because the sensor thicknesses remain constant during this experiment, the sensor resistivity versus temperature can be extracted from these data (shown in Figure 4.14). Because the sensor is made of heavily-doped polysilicon, it exhibits a positive thermal coefficient of resistance (TCR) [41]. For the sensor data shown in Figure 4.14, the TCR is approximately $0.1 \frac{\%}{^\circ\text{C}}$.

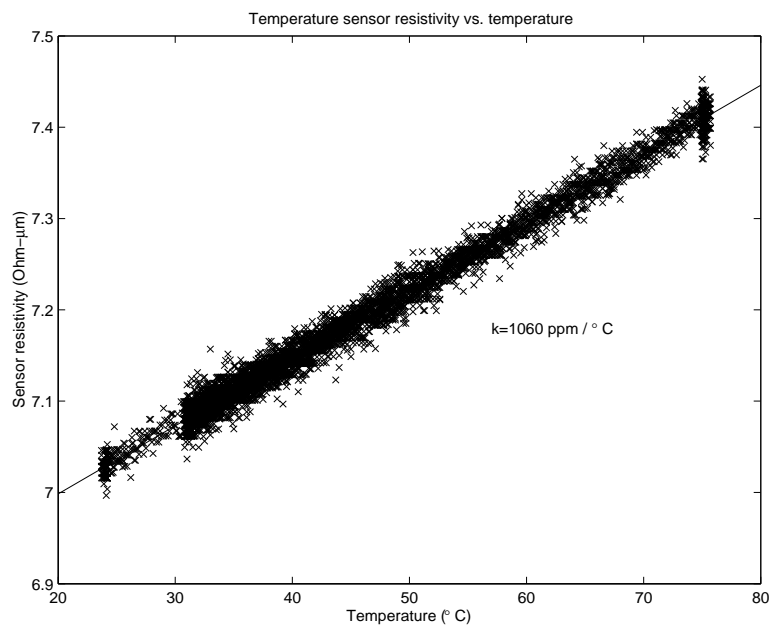


Figure 4.14: Plot of sensor resistivity versus temperature.

4.5.5 Experimental Results

To test the sensors under etching conditions, they were placed into the XeF_2 chamber and etched. To assess the gauge factors of the film thickness sensor, an experiment was conducted during which the sensor was repeatedly etched and then independently measured. The full experimental procedure is shown in Table 4.1. This procedure is designed to compare the sensor output to a reference thickness measurement, provided by a reflectometry system, at multiple absolute thickness values. This way, the accuracy, repeatability, and stability of the sensor can be computed.

This experiment was carried out on a wafer with three sensors, and the resulting data are shown in Figure 4.15. In the XeF_2 chamber used, the XeF_2 gas entered from a single port on the side of the process chamber. For this reason, the etch proceeded more rapidly on that side of the wafer, because the etchant became depleted as it moved across the wafer. Therefore, the sensor on the side closest to the entrance port

-
1. Measure the thickness of sensor using the NanoSpec /AFT reflectometric film-thickness measurement station.
 2. Record real-time measurements of film-thickness from the sensor while performing a polysilicon etch in the XeF₂ reactor. Etch only a fraction of the sensor's total thickness.
 3. Remove the sensor-wafer from the etch chamber and re-measure the sensor's new film-thickness using the NanoSpec.
 4. Repeat the process until the sensor is fully etched away
-

Table 4.1: XeF₂ etch rate sensor experimental procedure.

is etched the fastest, and this effect can be seen in Figure 4.15. Between each of the etches, the sensors were each measured using the NanoSpec system.

One problem that was encountered during the experiment is related to the roughness of the etched sensors. Because XeF₂ is highly selective to SiO₂, the thin native oxide on the polysilicon inhibits the etch for several minutes. When the etchant finally breaks through the oxide surface, it rapidly consumes the underlying silicon. This breakthrough occurs in some places before others, resulting in a very rough silicon surface. High surface roughness such as this tends to scatter the light used in reflectometry, thereby rendering the measurements inaccurate. For this reason, reflectometry measurements below $\approx 6000\text{\AA}$, as measured by the sensors, were discarded in the gauge analysis.

A summary of the results from these experiments is shown in Table 4.2. For each row of the table, the difference between the sensor-measured thickness and the NanoSpec measured thickness is computed, and these values are listed on the right as the sensor bias. As can be seen from the table, the maximum bias value is -45.9\AA , which corresponds to a 0.7% error.

To compute the sensor repeatability, a sample of sensor data was taken at constant

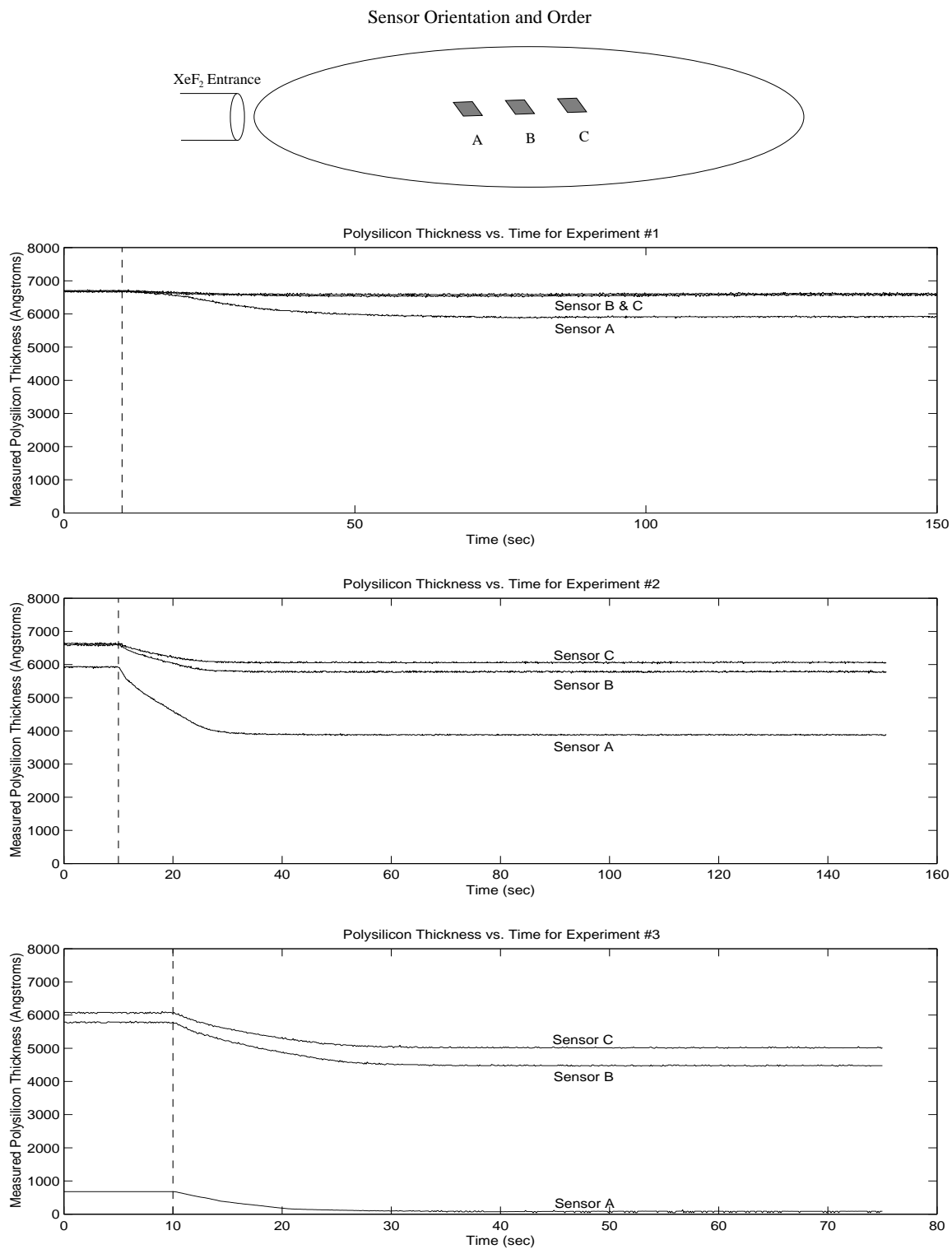


Figure 4.15: Experimental results from in-situ XeF_2 etch tests. The vertical dotted lines indicate the times when XeF_2 was introduced into the chamber.

Trial		Sensor Measurement		NanoSpec	
Exp. #	Sensor	Average (\AA)	St. Dev. (\AA)	Measurement (\AA)	Bias (\AA)
before	A	6689.1	12.5	6686.0	3.1
	B	6691.2	12.4	6687.3	3.9
	C	6700.9	14.4	6696.7	4.2
1	A	6679.1	11.0	6663.7	15.4
	B	6678.3	15.3	6668.0	10.3
	C	6698.6	13.2	6682.0	16.6
2	A	5925.1	13.7	6417.4	N/A
	B	6586.5	13.2	6632.4	-45.9
	C	6623.1	14.9	6650.6	-27.5
3	A	678.4	0.8	N/A	N/A
	B	5782.3	13.0	6416.6	N/A
	C	6069.7	13.6	6537.0	N/A

Table 4.2: Results of sensor and NanoSpec measurements.

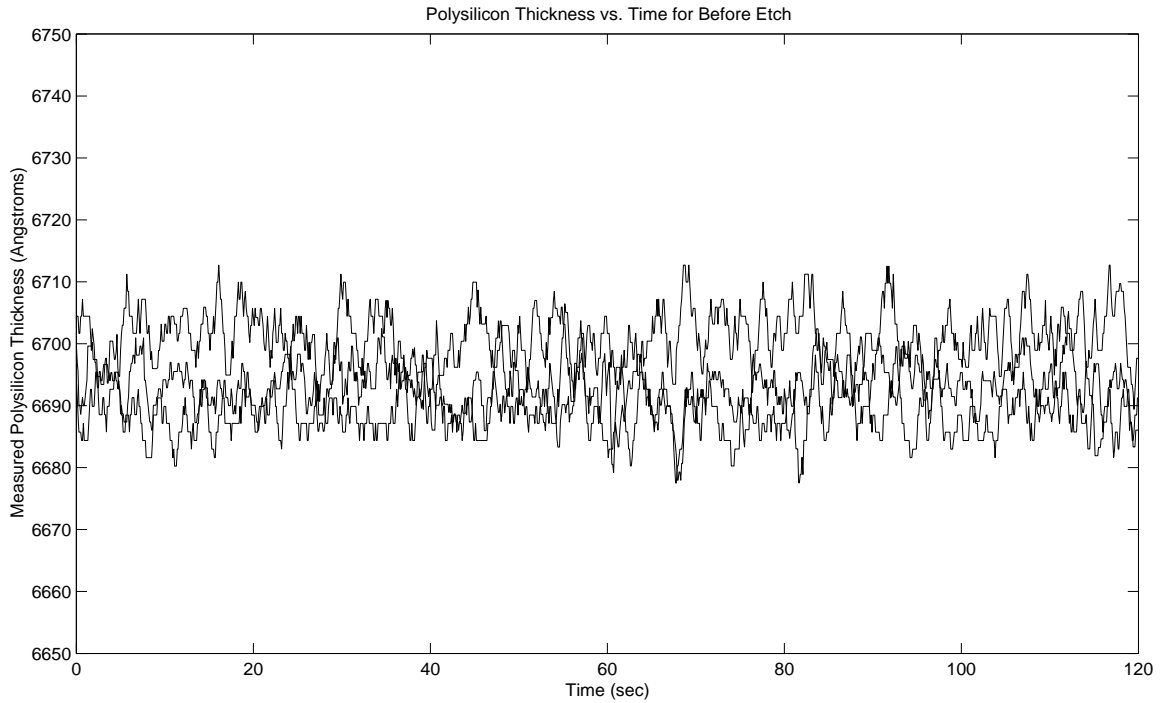


Figure 4.16: Sensor output with constant-thickness, for repeatability determination.

temperature and prior to any etching. A plot of this data is shown in Figure 4.16. The average of the standard deviations for the three sensors is 13.1\AA , or 0.2% of the full-scale value.

To compute the stability of the sensor, two sets of sensor data were taken approximately 15 minutes apart, and the average sensor outputs compared. The two averages differed by 3.2\AA , and this difference can most likely be attributed to a slight temperature fluctuation during the period.

Temperature Correction

To compensate for thermal variations in the polysilicon resistivity, the output of the buried van der Pauw structure was used. Because the buried sensor's thickness does not change, its current/voltage measurements, combined with the *a-priori* thickness measurement, t_o , can be used as a gauge of the polysilicon resistivity. By

substituting the equation for the resistivity of the buried structure into Equation 4.11, we can solve for the temperature-compensated thickness value,

$$t = \frac{\ln(2)\rho_{e,\text{polysilicon}}}{\pi} \frac{I}{V_{\text{exposed}}} \quad (4.13)$$

$$\rho_{e,\text{polysilicon}} = \frac{\pi t_o}{\ln(2)} \frac{V_{\text{buried}}}{I} \quad (4.14)$$

$$\Rightarrow t_{\text{compensated}} = \left(\frac{V_{\text{buried}}}{V_{\text{exposed}}} \right) t_o \quad (4.15)$$

where I is the same current through both sensors, V_{exposed} and V_{buried} are the voltages measured from the exposed and buried sensors, respectively, and t_o is the actual beginning thickness of the sensors, measured using a reflectometer. Equation 4.15 can therefore be used to compensate for variations in the polysilicon resistivity.

Another experiment was performed in which the wafer placed into the XeF_2 chamber and etched. Just before the etch, a section of the wafer close to the sensors was scratched, exposing a clean silicon surface at this location. The sensors, on the other hand, still had their thin native oxide protecting them from the etchant. This situation was meant to simulate the non-uniform nature of the etch.

Figures 4.17, 4.18, and 4.19 show the data from this experiment. The data are broken up into three sections (corresponding to the three figures); between each section, the wafer was removed from the chamber and inspected. The data are also moving average filtered, to reduce noise and make the trends more apparent. Each figure consists of two plots, with the top plot showing the thickness measurements and the bottom plot showing temperature measurements. The thickness plots each show two traces: one shows the raw, uncompensated output from the film thickness sensor, and the other shows the compensated thickness which uses the resistivity measured by the buried sensor. The temperature plots are generated by mapping the resistance measured by the buried sensor to the sensor temperature using Figure 4.14.

In the first section, no etching is taking place, and the temperature remains constant. The standard deviation of the uncompensated sensor (with the moving average

in place) is 5.1\AA , while the standard deviation for the compensated sensor is 6.0\AA . Here, the compensated sensor shows higher variance because it is the result of a division of two voltage measurements, V_{exposed} and V_{buried} (see Equation 4.15), while the uncompensated sensor is the result of a division of a voltage and a current. The inherent noise in the voltage and current measurements are different, resulting in different variances of the two traces.

In the second section, the etch begins to occur at the nearby location, about 110 seconds into the experiment. This raises the temperature of the sensors, as seen by the sharp rise in the temperature sensor output around 110 seconds. At this point, the uncompensated sensor also begins to heat up, causing its apparent thickness to drop by about 30\AA . However, the uncompensated sensor is not affected by this temperature rise, and its thickness value stays fairly constant. Here, the standard deviation of the uncompensated output rises to 13.1\AA , due to the temperature rise, while the compensated output's standard deviation stays roughly constant, at 5.9\AA . In this set of data, the thermal compensation method has reduced the standard deviation by about 7.2\AA , a 220% improvement.

In the final section, the etchant begins to etch the sensors. Both thickness traces decrease at approximately $36\frac{\text{\AA}}{\text{min}}$. However, the compensated thickness trace is approximately 13\AA higher than the uncompensated trace; this is due to an overall rise in the wafer temperature. Note that the average temperature at the beginning of the experiment (Figure 4.17) is $26.4\text{ }^{\circ}\text{C}$, while the average temperature in Figure 4.19 is $27.5\text{ }^{\circ}\text{C}$. This increase in temperature manifests itself as an apparent drop in the uncompensated thickness. In this set of data, the thermal compensation method has improved the accuracy by about 13\AA , which is a 39% improvement (assuming an uncompensated accuracy of 46\AA).

The compensation method also significantly improves the sensor stability. Two sets of data were taken approximately 15 minutes apart, and no etching was done during the period. The uncompensated sensor output drifted by 7.4\AA during the

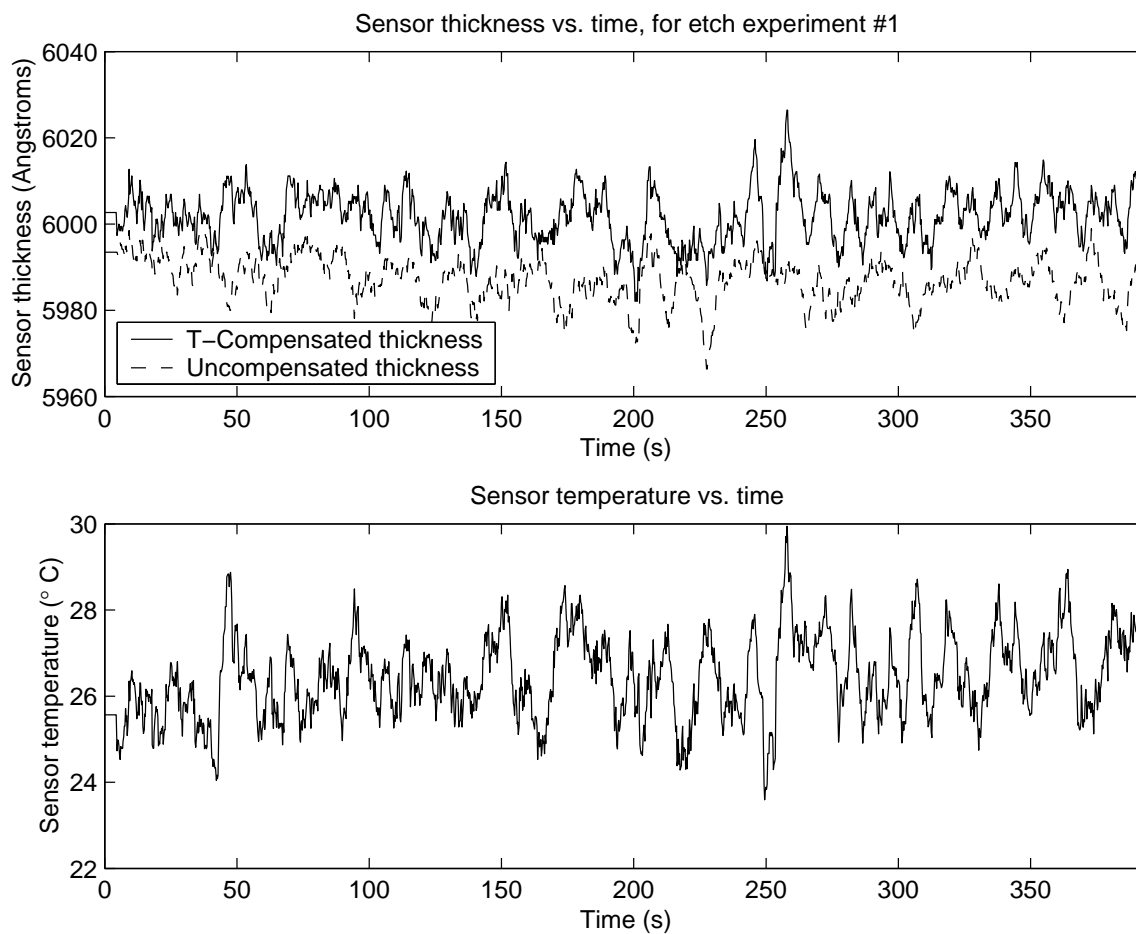


Figure 4.17: Results from the second in-situ XeF_2 etch experiment, data set #1. The top plot indicates thickness (containing a temperature-compensated trace and an uncompensated trace), while the bottom plot indicates temperature.

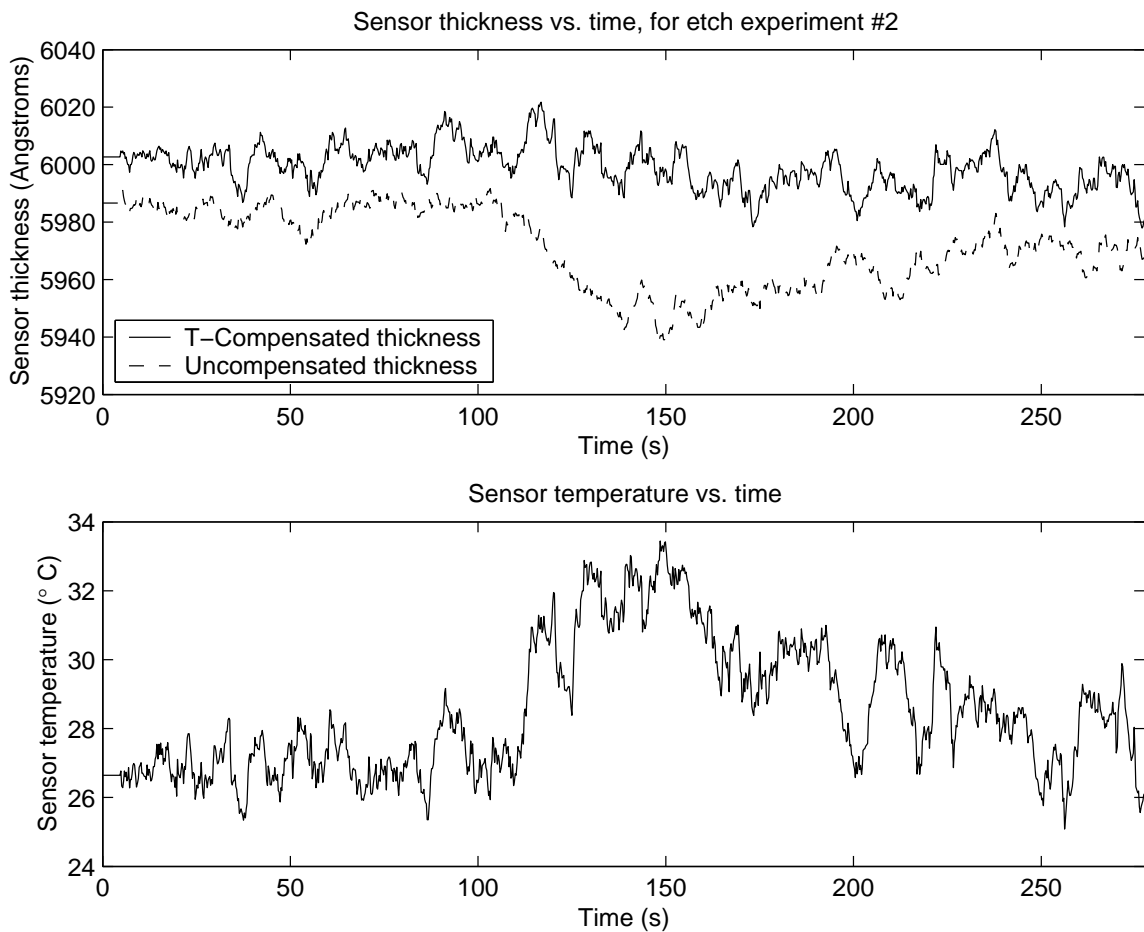


Figure 4.18: Results from the second in-situ XeF_2 etch experiment, data set #2. The top plot indicates thickness (containing a temperature-compensated trace and an uncompensated trace), while the bottom plot indicates temperature.

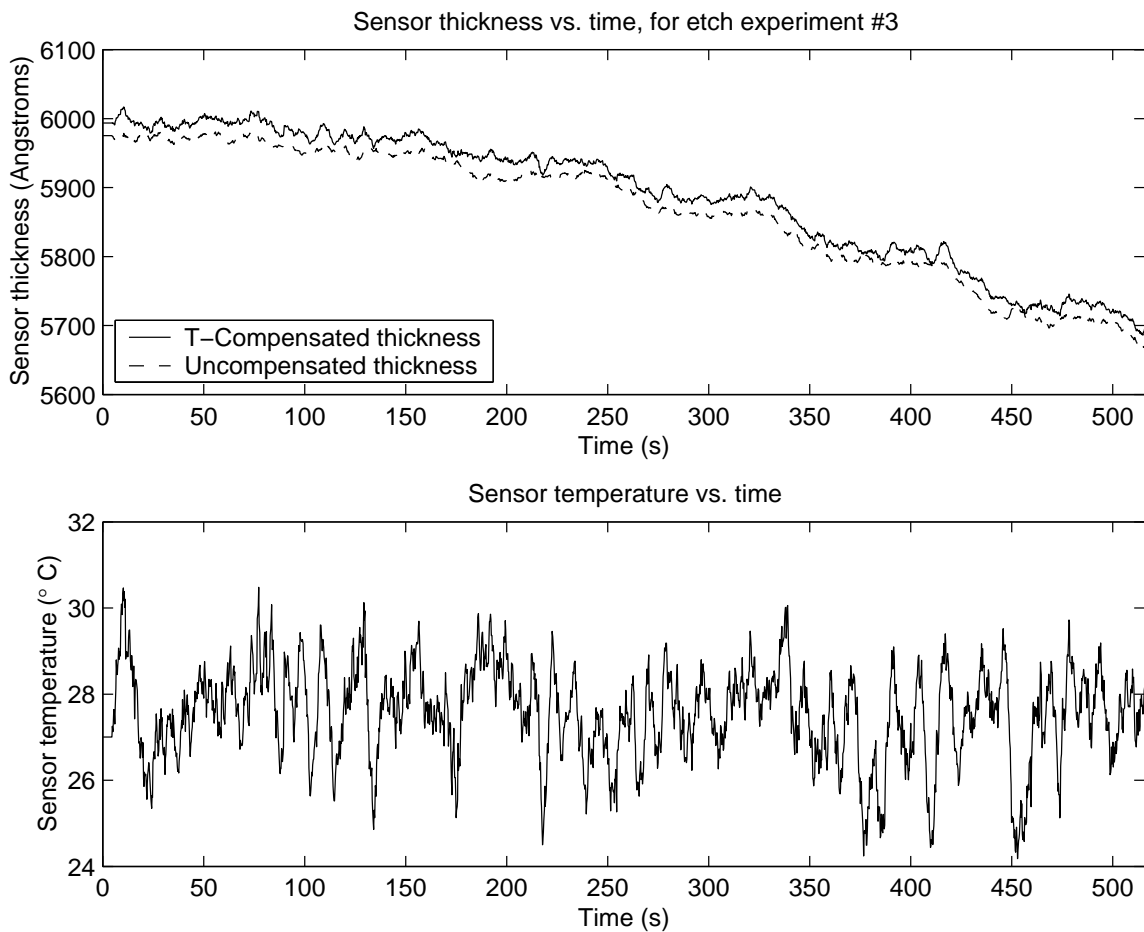


Figure 4.19: Results from the second in-situ XeF_2 etch experiment, data set #3. The top plot indicates thickness (containing a temperature-compensated trace and an uncompensated trace), while the bottom plot indicates temperature.

period, while the compensated output drifted by only 0.8\AA . This fact clearly indicates that the drift in the thickness sensor is almost entirely due to a change in temperature. Indeed, the average temperature, as measured by the buried sensor, changed by $1.0\text{ }^{\circ}\text{C}$ during the 15 minute period.

4.6 Summary

This chapter describes the design, construction, and testing of a prototype film thickness measurement wafer, for use in polysilicon etch processes. The results presented show that such a sensor can be successfully operated inside an etch environment, and can provide repeatable, accurate, stable measurements. The accuracy was shown to be better than 50\AA , repeatability better than 15\AA , and stability better than 1\AA over a 15 minute period. The sensor detects and compensates for temperature shifts through the use of a buried reference sensor.

Chapter 5

Thermal Flux Sensor

5.1 Introduction

This chapter treats the design, fabrication, and testing of a thermal flux sensor for use in plasma etch processes. This thermal flux sensor has the capability to separately resolve the heating due to ion flux and that due to surface chemical reactions.

As will be described in this chapter, thermal flux sensors have a number of important applications. First, because these sensors provide more information about the plasma than is available using conventional sensors, it can be used to refine plasma process modeling and to more reliably diagnose faults in production equipment. Second, these sensors have the ability to indirectly measure the etch rate (through its correlation with the amount of chemical heating) and also the ion flux (through its correlation with the amount of ion flux heating). Direct measurement of either of these quantities typically requires a much more complicated apparatus. In addition, direct-measurement sensors for these quantities are typically consumed rapidly by the process (as was seen for the film thickness sensor described in Chapter 4).

The remainder of this chapter is organized as follows. First, the importance and role of thermal flux sensors is discussed. Next, the particular design developed in this dissertation is presented. Following this, a full analysis of the performance of

this sensor is presented, including sensitivity, time constant, and noise analysis. This analysis motivates a modification to the basic structure which allows a higher overall sensitivity, and a similar analysis is performed on this structure. Finally, experimental results from the second type of sensor are presented and discussed.

5.2 Motivation & Related Research

While some studies report findings that various plasma etch parameters, such as etch-rate, are independent of temperature [42, 43], the great majority of research results (both theoretical [23, 24, 44] and experimental [45–49]) indicate a strong temperature dependence of these parameters. Non-uniformity of temperature therefore causes etch nonuniformity, which, in turn, adversely affects circuit yield [1]. This temperature non-uniformity can be caused by non-idealities in both the deposition of heat energy onto the surface of the wafer, and also by heat transfer from the backside of the wafer by the chuck and wafer cooling system [23]. Further, the top surface of the wafer is heated by several sources. These include energetic ions and electrons striking the wafer, exothermic chemical reactions occurring on the surface of the wafer, and neutral atom recombination or de-excitation at the wafer surface [46]. Of these various heating mechanisms, the two dominant sources in typical plasma etch processes are ionic heating and exothermic chemical heating [46]. Of course, the proportion of deposited heat from ions and chemistry depends strongly on the type of etch process. Metal etch processes, for example, exhibit a more exothermic etch reaction than polymer etch [45]. Reactive ion etch (RIE) processes tend to have much higher ion bombardment energy, which leads to a higher proportion of ionic heating in these processes [45].

Many different “macroscale” thermal flux sensors have been fabricated for a number of different applications [50–62]. However, these sensors all use macroscale fabrication techniques, which makes them large (in comparison to devices made using IC

technology) and difficult to manufacture. Several thermal flux sensors have been fabricated using IC technology [53, 63–71], but most require a highly specialized MEMS-based process. This makes integration with on-chip electronics difficult, and results in complex, expensive sensor fabrication. Finally, a few researchers have used *temperature* sensors to infer thermal flux to the substrate in ZnO sputtering processes [72], X-ray mask processing [73], and in rapid thermal process (RTP) chambers [74]. One study used a *thermal flux* sensor to measure single-point thermal flux to a blank substrate location in a metal sputtering process [75]. However, all of this work involves the placement of very few (one or two) macroscale temperature sensors onto a non-silicon substrate to measure thermal properties.

To the author’s knowledge, no work has been done to measure spatially resolved thermal flux, with ion flux and exothermic chemical reactions measured separately, to the wafer during plasma etching. This information would be useful, both for detailed plasma modeling and for more reliable equipment diagnosis and fault isolation.

5.3 Sensor Design

5.3.1 Geometrical Considerations

In general, thermal flux sensors are structures that convert the thermal flux of interest into a difference in temperature between two points on the structure. Measurement of the heat flux then reduces to measurement of this temperature difference. The simplest such structure, shown in Figure 5.1, consists of a rectangular block of dielectric, with known thermal conductivity (κ) and thickness (t). A thermal flux perpendicular to this sensor (q_{\perp}) produces a temperature difference (ΔT) across the sensor proportional to the applied thermal flux, according to the Fourier law,

$$\Delta T = \frac{t}{\kappa} q_{\perp} \quad (5.1)$$

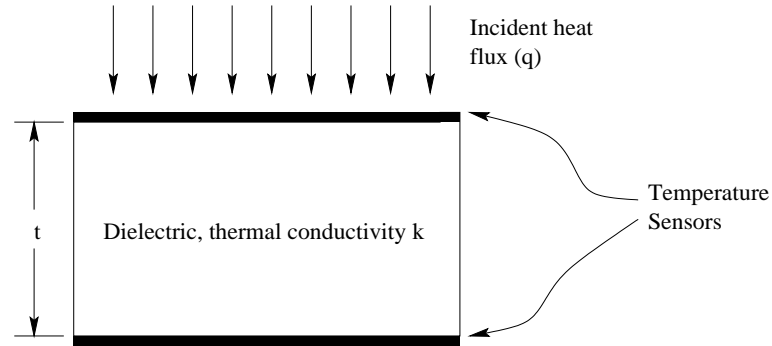


Figure 5.1: “Direct” thermal flux measurement structure.

As will be discussed in Section 5.3.3, other more complicated structures are also possible. Depending on the sensor application, the goal of these structures could be increased sensitivity, decreased thermal resistance, or faster time constant. However, all such sensors function by inducing a temperature difference across two points.

5.3.2 Transduction Method

There are many methods for measuring a difference in temperature between two points, including thermistors, thermopiles, and resistive temperature detectors (RTDs). Each has advantages and disadvantages relating to their accuracy, ease of use, speed, and many other parameters.

For the simple thermal flux sensor structure shown in Figure 5.1, using typical surface feature dimensions ($\approx 2\mu m$ thicknesses), thermal conductivities ($1.38 \frac{W}{mK}$ for SiO_2) and plasma thermal fluxes ($\approx 1000 \frac{W}{m^2}$), the resultant temperature difference is extremely small. A simple calculation reveals that,

$$\Delta T = \frac{(2\mu m)}{\left(1.38 \frac{W}{mK}\right)} \left(1000 \frac{W}{m^2}\right) = 0.001K \quad (5.2)$$

To accurately measure thermal gradients of this magnitude, some form of amplification is required. One of the most widely used techniques here is to employ a thermopile [53, 64, 66]. This method uses the natural amplification property given by

the series connection of many thermocouples. Because each thermocouple adds its thermovoltage to the overall output voltage, the output voltage can be amplified many hundreds or thousands of times by simply interconnecting hundreds or thousands of thermocouples in series. However, this method has a number of drawbacks. First, the size of the measurement structure is linearly related to the number of interconnected thermocouples. Second, typical thermocouples use “exotic” materials that have a high Seebeck coefficient to achieve maximum sensitivity [69]. However, these materials are not used in standard CMOS processes. The n-type and p-type polysilicon layers in CMOS processes can be used to fabricate a thermocouple, but the sensitivity of this thermocouple is much lower than traditional thermocouple materials [69].

5.3.3 The Gardon Gauge

Another alternative to accurately measure thermal flux is to increase the thickness t . This will result in an increase of the temperature gradient ΔT (see Equation 5.1). While vertical dimensions in a CMOS process are limited to a few micrometers, lateral dimensions are not. Therefore, by employing a structure that “redirects” the heat flow from the perpendicular direction to the horizontal, sensors with much larger values of t can be fabricated. To perform this redirection, we employ a structure similar to the Gardon thermal flux sensor [50]. In this type of thermal flux sensor (shown in Figure 5.2), the heat is incident on a thin insulating membrane. Since the membrane is in thermal isolation with no films above or below it, and the absolute temperature and pressure are low in typical plasma processes, convection and radiation thermal losses from the membrane can be safely ignored (see Section 5.5 for an analysis to justify this claim). As a result, all of the incident heat must flow radially outward through the membrane to the edge. In the next section, it will be shown that the temperature difference between the center of the membrane and the edge (ΔT) is given by,

$$\Delta T = q \frac{D^2}{16\kappa w} \quad (5.3)$$

Here, q is the incident thermal flux, D is the diameter of the membrane, w is its thickness, and κ is its thermal conductivity.

Two of these membrane structures can be fabricated in close proximity to each other on the wafer. One of these can be coated with an etch-sensitive material; this sensor will henceforth be known as the “etched sensor”. This configuration permits the effects of ion flux heating and exothermic etch reaction heating to be resolved. As the ion flux (over short distances) can be assumed to be uniform and not loaded by the presence of sensor structures, both sensors are heated equally by ion flux. However, since only the etched sensor is coated with a material that is etch sensitive, this sensor will have an additional thermal flux due to exothermic reactions. Therefore, the isolated sensor (henceforth known as the “non-etched sensor”) measures the ion flux heating, and the difference between the two sensor outputs measures the exothermic chemical heating.

5.4 Standard Gardon Gauge: Operation

This section describes in further detail the structure of a standard Gardon gauge, fabricated using standard semiconductor processes. In addition, the electrical connections and measurement scheme are also given.

5.4.1 Operating Principle

In the standard Gardon structure (shown in Figure 5.2), the thermal flux of interest strikes a thin membrane. All of this heat flows laterally along the membrane, inducing a temperature difference between the center and edge. Temperature sensors are then placed at the center and edge of the membrane, and the difference between

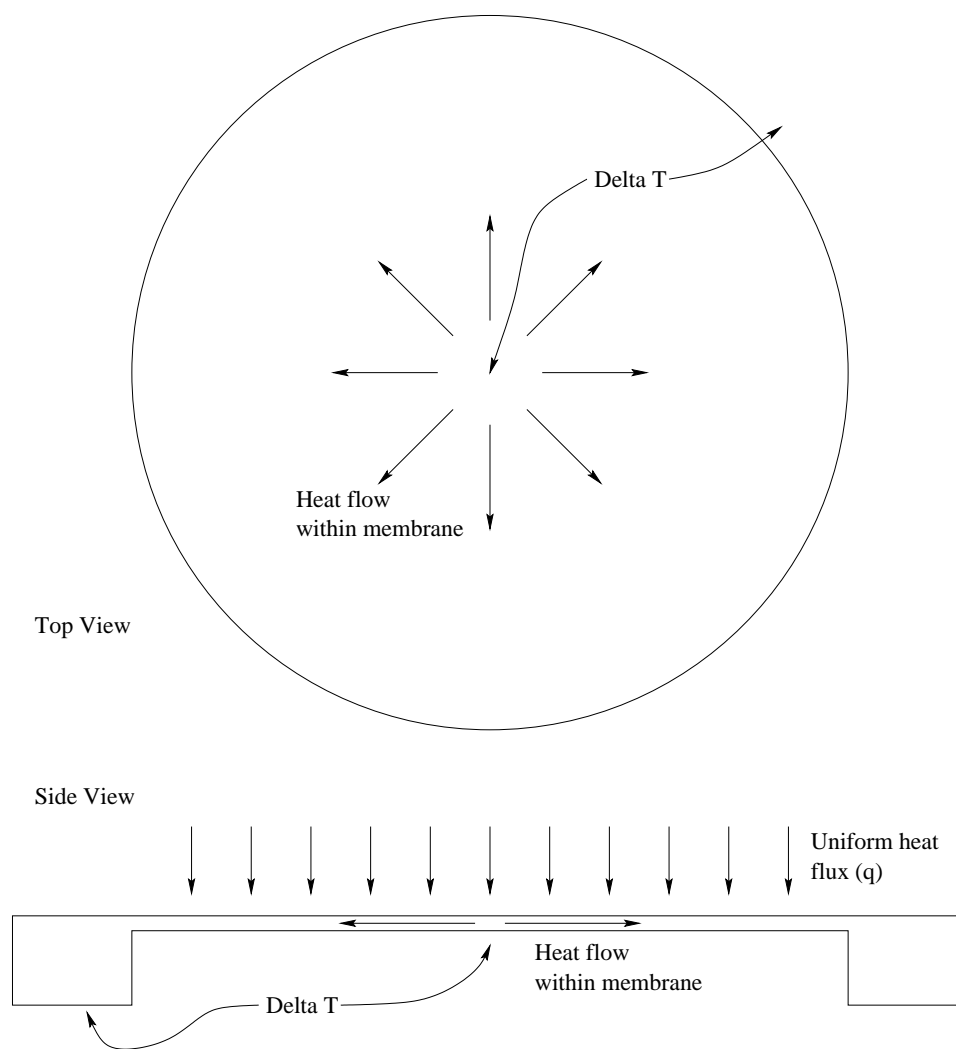


Figure 5.2: Gardon type thermal flux sensor.

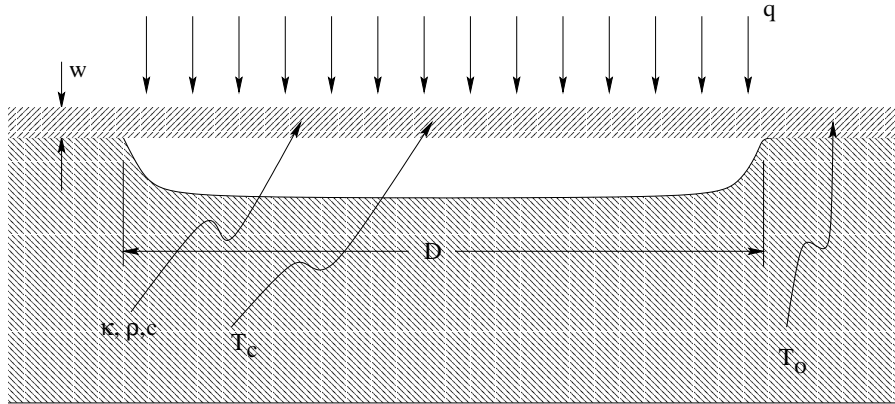


Figure 5.3: Closeup of Gardon gauge structure, with dimensions and material properties labeled.

the readings is used to calculate the thermal flux. This process is described in more detail in the following sections.

5.4.2 Membrane

Figure 5.3 shows a diagram of the system under consideration, including the relevant dimensions and material properties. We take a differential element of the membrane structure (shown in Figure 5.4), and calculate the heat transfer within this element using the heat diffusion equation,

$$\frac{\partial T}{\partial t} = \frac{\kappa}{\rho c} \nabla^2 T \quad (5.4)$$

Here, T is temperature, κ is the thermal conductivity, ρ is the material density, and c is the specific heat of the medium. For the differential element shown in Figure 5.4 [50], the heat diffusion equation becomes,

$$\frac{\partial T}{\partial t} 2\pi r w c \rho \partial r = 2\pi r q \partial r - \frac{\partial T}{\partial r} 2\pi \kappa r w + \left(\frac{\partial T}{\partial r} + \frac{\partial^2 T}{\partial r^2} \partial r \right) 2\pi \kappa w (r + \partial r) \quad (5.5)$$

$$\Rightarrow \frac{c \rho}{\kappa} \frac{\partial T}{\partial t} = \frac{q}{w \kappa} + \frac{1}{r} \frac{\partial T}{\partial r} + \frac{\partial^2 T}{\partial r^2} \quad (5.6)$$

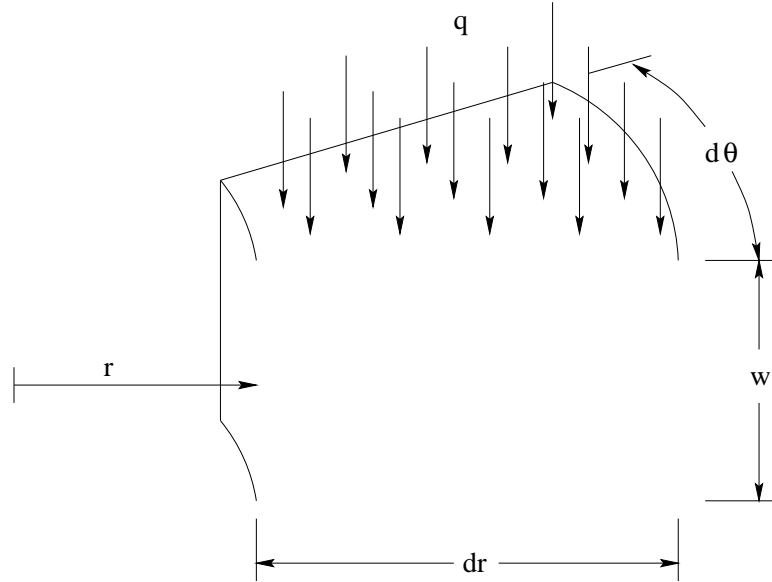


Figure 5.4: Differential element of gardon gauge membrane, used for thermal analysis.

where r , dr , w , and q are shown in Figure 5.4, and $T(r, t)$ is the temperature of this element, which is constant throughout the differential element in the limit $dr, d\theta \rightarrow 0$. The boundary conditions for this system are,

$$T = T_o \quad \text{for } t = 0 \text{ and } 0 < r < \infty \quad (5.7)$$

$$T = T_o \quad \text{for } 0 < t < \infty \text{ and } r \geq \frac{1}{2}D \quad (5.8)$$

By taking $\frac{\partial T}{\partial t} = 0$ in Equation 5.6, and assuming radial symmetry, we get the ordinary differential equation for the steady state temperature distribution in the membrane,

$$\frac{d^2T(r)}{dr^2} + \frac{1}{r} \frac{dT(r)}{dr} + \frac{q}{w\kappa} = 0 \quad (5.9)$$

where $T(r)$ is the steady state temperature distribution in the membrane. The solution to Equation 5.9, subject to the boundary conditions given in Equation 5.7, is,

$$T(r) = \frac{q}{16\kappa w} (D^2 - r^2) + T_o \quad (5.10)$$

Therefore, the difference between the center temperature and the outside temperature is given by,

$$\Delta T \equiv \left[T(0) - T\left(\frac{1}{2}D\right) \right] \equiv (T_c - T_o) = \frac{D^2}{16\kappa w} q \quad (5.11)$$

5.4.3 Temperature sensors

The proposed sensor uses temperature sensitive polysilicon resistors to measure the inside and outside temperatures. For heavily-doped polysilicon, the resistivity (ρ_{poly}) is a linear function of temperature [76],

$$\rho_{\text{poly}} = \rho_0 (1 + \alpha (T - T_0)) \quad (5.12)$$

where ρ_0 is the resistivity at $T = T_0$, and α is the temperature coefficient of resistivity for polysilicon. Therefore, for a given resistor size, the total resistance is also linearly dependent on temperature. A change in temperature, ΔT , results in a resistance change,

$$\Delta R = R_0 \alpha \Delta T \quad (5.13)$$

Typically, this equation is used to find the change in resistance as a resistor's temperature is changed. However, it can also be applied to find the difference in resistance between two identical resistors that are at different temperatures. We will use Equation 5.13 in this way to compare the temperatures at the center and edge of the Gardon membrane.

5.4.4 Wheatstone Bridge

When measuring differential resistances, the Wheatstone bridge circuit (shown in Figure 5.5) is widely employed. In this circuit, two resistive voltage dividers are

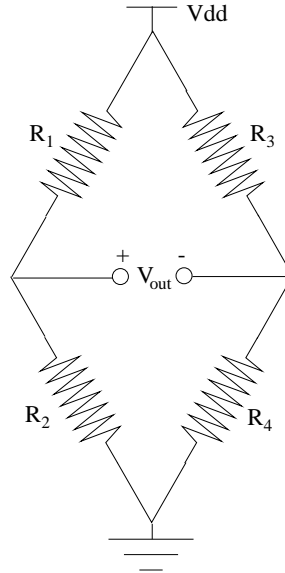


Figure 5.5: Standard Wheatstone bridge resistor configuration.

constructed, and their respective output voltages are compared. For the configuration shown, V_{out} is given by,

$$V_{out} = \frac{R_2}{R_1 + R_2} V_{DD} - \frac{R_4}{R_3 + R_4} V_{DD} = \frac{R_2 R_3 - R_1 R_4}{(R_1 + R_2)(R_3 + R_4)} V_{DD} \quad (5.14)$$

The Wheatstone bridge is typically used in the balanced, equal-resistance regime, where $R_1 \approx R_2 \approx R_3 \approx R_4 \equiv R$. In this case, the nominal output voltage $V_{out} = 0$ (see Equation 5.14 with $R_1 = R_2 = R_3 = R_4$). Thus, the measured voltage is actually ΔV_{out} . The differential output voltage simplifies to [77].

$$\Delta V_{out} = \left[\frac{\eta + 1}{2(\eta + 2)} \right] [(\Delta R_2 - \Delta R_1) - (\Delta R_4 - \Delta R_3)] \frac{V_{DD}}{R} \quad (5.15)$$

where η is given by the total variation in all resistors,

$$\eta = \frac{\Delta R_1}{R} + \frac{\Delta R_2}{R} + \frac{\Delta R_3}{R} + \frac{\Delta R_4}{R} \quad (5.16)$$

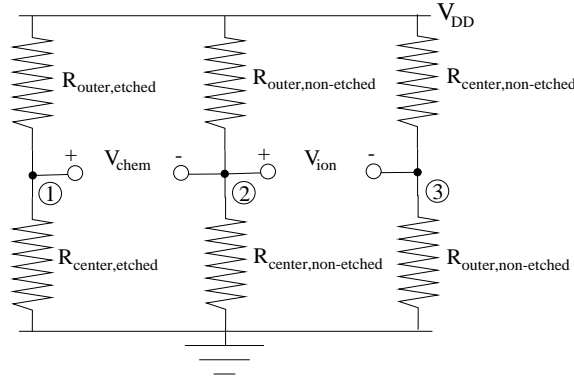


Figure 5.6: Wheatstone bridge arrangement for gardon gauge structure.

When the deviations of $R_1 \dots R_4$ are small, $\eta \approx 0$, and Equation 5.15 simplifies to,

$$\Delta V_{out} = [(\Delta R_2 - \Delta R_1) - (\Delta R_4 - \Delta R_3)] \frac{V_{DD}}{4R} \quad (5.17)$$

5.4.5 Complete System

For the complete sensor system, we construct the Wheatstone bridge arrangement as shown in Figure 5.6. In this structure, each of the vertical legs of the bridge represents a single Gardon thermal flux sensor, using resistive temperature sensors at the center and edge. The labels on each resistor denote their location; for example, $R_{\text{center,etched}}$ represents the resistor located at the *center* of the *etched* thermal flux sensor. Using the analysis from the previous sections, relations for V_{chem} and V_{ion} can be derived,

$$V_{\text{chem}} = \frac{1}{4R} [(\Delta R_{\text{center,etched}} - \Delta R_{\text{outer,etched}}) - \dots (\Delta R_{\text{center,non-etched}} - \Delta R_{\text{outer,non-etched}})] V_{DD} \quad (5.18)$$

$$V_{\text{ion}} = \frac{1}{2R} (\Delta R_{\text{center,non-etched}} - \Delta R_{\text{outer,non-etched}}) V_{DD} \quad (5.19)$$

Equation 5.19, of course, assumes that the values of R_{inner} and R_{outer} are identical for

the two non-etched sensors. This assumption can be tested in the finished product by comparing terminal ② to an external pair of reference resistors that are located off-chip. This method, however, has the disadvantage that the external references are not co-located with the sensors; consequently, the overall sensor will probably be very sensitive to absolute temperature and other factors. However, using appropriate layout techniques, it is possible to match the resistances of the inner and outer resistors reasonably well (see Section 5.12.1 for experimental verification).

5.5 Standard Gardon Gauge: Analysis Assumptions

For the analysis of the standard Gardon gauge, many assumptions related to the structure, material properties, and dimensions, are made. These assumptions are listed and justified in this section.

5.5.1 Incident Thermal Flux is Spatially Uniform

This assumption mandates that the measured heat flux is uniform over distances equal to the sensor size (0.5mm or less). While there may be differences across very small distance scales in general, the application of this sensor is to wafer-scale non-uniformities. Therefore, these small-scale variations will be ignored for this application, and the assumption will be made that they average out.

5.5.2 Incident Thermal Flux Strikes Top Surface Only

The next assumption states that the measured heat flux may only strike the top surface of the membrane. Because the structure of the sensor will be such that the bottom size is enclosed by a silicon well, this can be considered a good assumption.

5.5.3 Membrane has Spatially Uniform Thermal Properties

The next assumption dictates that the material used to construct the membrane must be spatially uniform, in terms of thermal conductivity, specific heat, and density. As typical semiconductor processes (which will be used to construct the sensor) can be uniform within several percent across the entire wafer, it is a very good assumption that these parameters will be uniform across the $\approx 0.5mm$ size of the sensor.

5.5.4 Temperature Measurement Sensor has Zero Size

In this assumption, the central temperature sensor is assumed to occupy zero area. Obviously this is not possible in reality; however, the central sensor will be designed to occupy minimal area. If it takes up less than 10% of the total sensor area, then the assumption will be made that this is negligible.

5.5.5 All Heat Flows Out Membrane Edges

This last assumption states that all of the incident heat flows out of the membrane at the edges by conduction. It therefore must be shown that no heat is lost or gained from any other surface, either due to conduction, convection, or radiation. To verify this assumption, these other heat loss mechanisms must be analyzed. Since the edge of the membrane is supported along its periphery, and it is assumed that this is where the heat is lost, the only two membrane surfaces that need to be analyzed are the top and bottom of the membrane. These calculated results will be compared to the typical thermal fluxes of interest in a plasma, and $1000 \frac{W}{m^2}$ will be used for this value.

Heat loss through radiation

For radiation heat transfer, the governing equation is [78],

$$q_{\text{radiation}} = \epsilon\sigma(T^4 - T_{\text{surr}}^4) \quad (5.20)$$

where ϵ and T are the emissivity and surface temperature of the membrane, σ is the Stefan-Boltzmann constant ($5.67 \times 10^{-8} \frac{W}{m^2 K^4}$), and T_{surr} is the temperature of the surrounding environment. To calculate a worst-case radiation transfer, we assume the emissivity of the membrane is 1.0 and the surrounding chamber is $\approx 10K$ hotter than the membrane (which is assumed to be at $\approx 300K$). In reality, the membrane will be at nearly the same temperature as the chamber walls, since all are exposed to the plasma. Using these values yields a heat transfer of $64 \frac{W}{m^2}$. This is a worst-case estimate, and it is only 6% of the typical value; therefore, it can safely be ignored. For the radiation transfer from the membrane downward to the substrate, the temperature difference is much lower. Because the substrate material, silicon, is a good thermal conductor, the substrate temperature is in equilibrium, and this difference is likely to be less than a degree. Using $300K$ for the substrate temperature and $300.5K$ for the membrane temperature yields a thermal flux of $3 \frac{W}{m^2}$, 0.3% of the typical value.

Heat loss through convection

Convection heat transfer occurs when a fluid surrounding an object has bulk motion. Because the fluid is in contact with the object, heat is transferred to (or from) the fluid, and this heat is transported away from (or to) the object by the fluid. When the bulk fluid motion is due to some external phenomenon, then this is called *forced* convection. If there is no externally imposed fluid motion, it is still possible for convection to occur. Heat from the object causes the surrounding gas to expand, and this expansion sets up a flow within the gas, and *free* convection is said to occur.

For both types of convection, the relationship between temperature differences and thermal flux can usually be approximated by the equation [78],

$$q_{\text{convection}} = h(T - T_a) \quad (5.21)$$

where h is called the “convection coefficient”, T is the temperature of the object, and T_a is the temperature of the ambient fluid. When considering convective heat trans-

fer, the Nusselt number (Nu), a dimensionless quantity related to the temperature gradient at the surface, is often used. The Nusselt number is related to the convective heat transfer coefficient (h) by the following equation,

$$Nu \equiv \frac{hL}{k_f} \Rightarrow h \equiv \frac{Nuk_f}{L} \quad (5.22)$$

where L is a “characteristic length” associated with the geometry of the problem, and k_f is the fluid thermal conductivity. It can be shown that the average Nusselt number is only a function of two other dimensionless quantities, the Reynolds number (Re) and the Prandtl number (Pr) [79]. The Reynolds number is defined as,

$$Re \equiv \frac{VL}{\nu} \quad (5.23)$$

where V is the fluid velocity and ν is the kinematic viscosity of the fluid. For $Re < 5 \times 10^5$, the fluid flow can be assumed to be laminar, and an empirical formula for the relation between \bar{Nu} (the average Nusselt number) and Re and Pr is [79],

$$\bar{Nu} = 0.664Re^{\frac{1}{2}}Pr^{\frac{1}{3}} \quad (5.24)$$

The Prandtl number is a property of the fluid, and is defined as the ratio of the kinematic viscosity over the thermal diffusivity (α),

$$Pr \equiv \frac{\nu}{\alpha} \quad (5.25)$$

For the membrane structure under consideration, the characteristic length is on the order of the membrane diameter, and the velocities of interest are in the order of the gas flow rates. While these two quantities are independent of pressure, the kinematic viscosity is not, via its dependence on fluid density. To a good approximation, the kinematic viscosity is inversely proportional to pressure [79],

$$\nu(P) \approx \nu(760T) \frac{760T}{P} \quad (5.26)$$

Combining Equations 5.23 and 5.26, and using typical values for various parameters yields,

$$Re \approx \frac{\left(1 \frac{m}{s}\right) (200 \mu m)}{15.86 \frac{m^2}{s} \frac{760T}{20mT}} = 3.3 \times 10^{-10} \quad (5.27)$$

Since this is approximately 15 orders of magnitude less than the turbulent flow threshold, the flow will always be laminar. Therefore, Equation 5.24 can be considered a valid approximation, and Equation 5.24 together with Equation 5.22 yields,

$$h = \frac{0.664 Re^{\frac{1}{2}} Pr^{\frac{1}{3}} k_f}{L} \quad (5.28)$$

Typical numbers for Pr are on the order of 1, and typical values for k_f are on the order of $0.5 \frac{W}{mK}$ [79]. Using these values, along with the value for Re given by Equation 5.27 yields a value of $h \approx 0.05 \frac{W}{m^2K}$. With this value, and with a worst-case temperature difference of $10K$, Equation 5.21 yields a thermal flux of $0.5 \frac{W}{m^2}$, or 0.05% of the typically measured thermal flux value. Therefore, convection heat loss is not a concern for this sensor.

Heat loss through conduction

It was determined in the previous section that convection heat loss to the surrounding gas was negligible. However, heat loss can also occur by *conduction* from the membrane surface through the surrounding gas to the chamber walls. Similar to the relation for convection given above, conduction can be described by the equation [78],

$$q_{\text{conduction}} = \frac{k}{L} (T - T_{\text{surr}}) \quad (5.29)$$

where k is the “conduction coefficient” for the fluid, L is the distance between the object and the surroundings, and T_{surr} is the temperature of the surroundings.

The conduction coefficient for a gas is proportional to three parameters [79]: the mean free path (λ), average molecular velocity (\bar{c}), and molecular density (n). Therefore,

$$k \propto \lambda \bar{c} n \quad (5.30)$$

As λ is inversely proportional to gas pressure and n is directly proportional to gas pressure, these two effects cancel one another and the conduction coefficient is independent of temperature. However, at very low pressure, where λ becomes comparable to the dimensions of the containment vessel, the situation is different. Below this pressure, the “effective” mean free path becomes constant (equal to the vessel dimensions), while n continues to decrease. Therefore, at low pressures, the conduction coefficient is proportional to pressure. This regime is called “molecular flow”, as opposed to the high pressure regime which is called “viscous flow”.

This assumption can be used to find the conduction coefficient for a given pressure, if the coefficient at atmospheric pressure is known. An approximate equation for mean free path of air at $300K$ is [80],

$$\lambda \approx \frac{50\mu mT}{P} \quad (5.31)$$

where P is the gas pressure. Typical plasma chambers are on the order of $0.5m$ in diameter, and typical processing pressures are on the order of $20mT$; using these values in Equation 5.31 yields a mean free path of $2.5mm$. Because this is still well below the dimensions of the chamber, the conduction coefficient can be assumed to be the same as that for room temperature.

We assume a worst-case thermal drop from the membrane to the chamber wall of $10K$, a conduction distance of $0.5m$, and a typical conduction coefficient of $0.5\frac{W}{mK}$. Using these values with Equation 5.29 yields a thermal flux of $10\frac{W}{m^2}$, or 1% of the typical value. Therefore, conduction through the chamber gas is not a concern.

Finally, the conduction from the membrane down through the gap to the substrate must be computed. The analysis is the same as that used above, with the exception that the “vessel” is now the cavity below the membrane. Because this gap is on the order of $15\mu m$ for the proposed design, the mean free path ($2.5mm$) is significantly greater than this distance. Therefore, the conduction coefficient is proportional to the ratio of the ambient gas pressure to the pressure at which λ becomes comparable to $15\mu m$. This value, calculated using Equation 5.31, is $\approx 3T$. Therefore, the conduction coefficient within the gap is given by the relation,

$$k(P) \approx \frac{P}{3T} k_{\text{cond},760T} \quad \text{for } P < 3T \quad (5.32)$$

Computing the thermal flux across the gap using Equations 5.29 and 5.32 with a temperature differential of $0.5K$ yields a thermal flux of $110 \frac{W}{m^2}$, or 11% of the typical value. Because these are worst case estimates, this heat transfer mode can be assumed to contribute a negligible error.

Heat loss through electrical wires

The center thermistor must be electrically connected to the other resistors in the Wheatstone bridge. Therefore, wires must run from the edge of the membrane to the center. As these wires are likely to be good heat conductors, care must be taken to limit the conduction of heat through them. To accomplish this, the wires will be made thin and long, and will be connected to the membrane only where necessary.

A detailed analysis of the heat loss through the leads would be difficult, as it would depend heavily on the exact contact areas and membrane sizes involved. Therefore, care will be taken to minimize these areas where possible.

5.6 Standard Gardon Gauge: Performance

This section provides the detailed analysis of the standard Gardon gauge structure described in Section 5.4. Included in this analysis are the sensitivity, responsivity, power dissipation, time constant, and thermal noise.

5.6.1 Sensitivity

To find the sensitivity of the standard Gardon gauge structure, Equations 5.13, 5.18, and 5.19 can be combined to yield,

$$V_{\text{chem}} = \frac{\alpha}{4} [(\Delta T_{\text{center,etched}} - \Delta T_{\text{outer,etched}}) - \dots (\Delta T_{\text{center,non-etched}} - \Delta T_{\text{outer,non-etched}})] V_{DD} \quad (5.33)$$

$$V_{\text{ion}} = \frac{\alpha}{2} (\Delta T_{\text{center,non-etched}} - \Delta T_{\text{outer,non-etched}}) V_{DD} \quad (5.34)$$

Now, using 5.11 and the fact that $\Delta T_c - \Delta T_o = T_c - T_o$, we obtain,

$$V_{\text{chem}} = \frac{\alpha D^2 V_{DD}}{64 \kappa w} (q_{\text{etched}} - q_{\text{non-etched}}) = \frac{\alpha D^2 V_{DD}}{64 \kappa w} q_{\text{chem}} \quad (5.35)$$

$$V_{\text{ion}} = \frac{\alpha D^2 V_{DD}}{32 \kappa w} q_{\text{non-etched}} = \frac{\alpha D^2 V_{DD}}{32 \kappa w} q_{\text{ion}} \quad (5.36)$$

On re-arranging Equations 5.35 and 5.36, we obtain the sensitivity relations with respect to both ion flux heating and chemical heating,

$$S_{\text{chem}} \equiv \frac{V_{\text{chem}}}{q_{\text{chem}}} = \frac{\alpha D^2 V_{DD}}{64 \kappa w} \quad (5.37)$$

$$S_{\text{ion}} \equiv \frac{V_{\text{ion}}}{q_{\text{ion}}} = \frac{\alpha D^2 V_{DD}}{32 \kappa w} \quad (5.38)$$

5.6.2 Responsivity

Another important figure of merit for any thermal flux sensor is its responsivity. This quantity is defined as the sensitivity divided by the total sensor area, and it

defines the required sensor size for a given application. For the gardon membrane described above, the responsivity is given by,

$$R_{\text{chem}} \equiv \frac{S_{\text{chem}}}{A_{\text{chem}}} = \frac{\alpha V_{DD}}{16\pi\kappa w} \quad (5.39)$$

$$R_{\text{ion}} \equiv \frac{S_{\text{ion}}}{A_{\text{ion}}} = \frac{\alpha V_{DD}}{8\pi\kappa w} \quad (5.40)$$

5.6.3 Power Dissipation

Since the proposed sensor uses resistive sensing of temperature at the center of the membrane, some electrical heat will be dissipated in this resistor during measurement. If this heat is sufficient to increase the temperature of the membrane, then the external thermal flux measurement will be perturbed. The power dissipated in the center resistor during measurement is given by,

$$P \equiv I^2 R = \left(\frac{V_{DD}}{R_o + \Delta R_o + R_i + \Delta R_i} \right)^2 (R_o + \Delta R_o) \quad (5.41)$$

where R_o and R_i are the initial outer and inner resistances, and ΔR_o and ΔR_i are their changes in resistance. As typical resistance changes are small compared to the absolute magnitude of resistance, these perturbation terms can be ignored. Further, since we assumed that the inner and outer resistances are the same, Equation 5.41 simplifies to,

$$P = \frac{V_{DD}^2}{4R} \quad (5.42)$$

To deduce the effect of power dissipation on the measurement, it is useful to convert this absolute power quantity into an “equivalent” thermal flux. The equivalent thermal flux is defined as the amount of *external* thermal flux that would cause the same temperature profile as that imposed by the electrical heating alone. To calculate this quantity, Equation 5.9 must be solved for a more complicated set of boundary conditions corresponding to the presence of a heat generating resistor at the center.

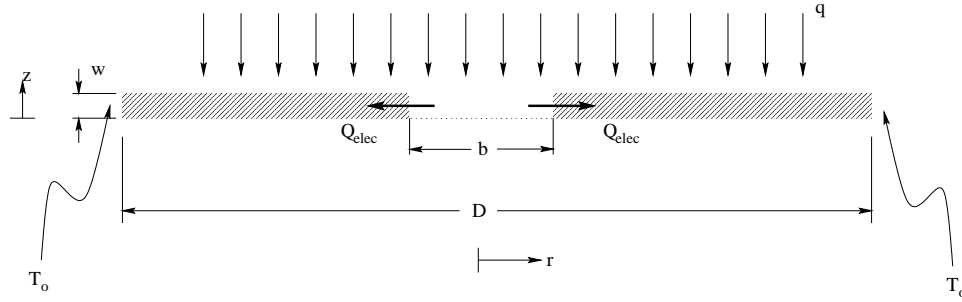


Figure 5.8: Gardon membrane with buried center temperature sensing resistor.

$$R = \frac{b^2 \rho_s}{2\lambda^2} \quad (5.44)$$

Assuming this resistor is buried inside the membrane, and this new system is arranged as shown in Figure 5.8, the new boundary equations for Equation 5.9 are given by,

$$T\left(r \geq \frac{1}{2}D\right) = T_o \quad (5.45)$$

$$\int_0^w \int_0^{2\pi} q\left(r = \frac{1}{2}b\right) r d\theta dz = P_{\text{electrical}} \quad (5.46)$$

where $q\left(r = \frac{1}{2}b\right)$ is the thermal flux flowing out of the cylindrical surface defined by $r = \frac{1}{2}b$. Equation 5.46 states that the integral of this thermal flux across the entire surface is equal to the total thermal power generated in the resistor region, $P_{\text{electrical}}$. As both radial and z-axis uniformity are assumed in this problem, the integral reduces to a product,

$$T\left(r \geq \frac{1}{2}D\right) = T_o \quad (5.47)$$

$$q\left(r = \frac{1}{2}b\right) = \frac{P_{\text{electrical}}}{2\pi bw} \quad (5.48)$$

Since we are now assuming that the external thermal flux is zero, Equation 5.9 becomes a homogeneous problem,

$$\frac{\partial^2 T(r)}{\partial r^2} + \frac{1}{r} \frac{dT(r)}{dr} = 0 \quad (5.49)$$

and the general solution of this problem is,

$$T(r) = A \ln(r) + B \quad (5.50)$$

By applying the boundary conditions from Equations 5.47 and 5.48, A and B can be found. The solution yields,

$$T(r) = \frac{-P_{\text{electrical}}}{4\pi\kappa w} \ln\left(\frac{2r}{D}\right) + T_o \quad (5.51)$$

To compare this to the solution without the resistor, we must assume that the central resistor region is iso-thermal. If $b \ll D$, this is a good assumption, and the temperature differential between center and edge is given by,

$$\Delta T = T\left(\frac{1}{2}b\right) - T\left(\frac{1}{2}D\right) = \frac{P_{\text{electrical}}}{4\pi\kappa w} \ln\left(\frac{D}{b}\right) \quad (5.52)$$

Equating this ΔT to that given by Equation 5.11, we can see that the equivalence between resistor heating power and external thermal flux is,

$$\frac{q_{\text{external}}}{P_{\text{electrical}}} = \frac{4}{\pi D^2} \ln\left(\frac{D}{b}\right) \quad (5.53)$$

If we assume that the inner and outer resistances are the same, then we can replace $P_{\text{electrical}}$ in Equation 5.53 with size and material parameters only, plus the supply voltage used for measurement, yielding the relation for the equivalent external thermal flux due to resistive heating,

$$P_{\text{electrical}} = \frac{V_{DD}^2}{4R} = \frac{V_{DD}^2 8\lambda^2}{4\pi b^2 \rho_s} \quad (5.54)$$

$$\Rightarrow q_{\text{p,equiv}} = \left(\frac{\lambda V_{DD}}{\pi D b}\right)^2 \frac{8}{\rho_s} \ln\left(\frac{D}{b}\right) \quad (5.55)$$

5.6.4 Time Constant

Since the temperature of the outer ring of the membrane is assumed to stay at constant temperature, and the only other place the temperature is measured is at the center of the membrane, it is sufficient to calculate the time constant for the center temperature. It is assumed that this time constant is equivalent to the overall sensor time constant. To find a first-order approximation, the further assumption that the entire membrane can be modeled as a “lumped capacitance” is made. Using this assumption, Equation 5.6 simplifies to,

$$\frac{c\rho}{\kappa} \frac{\partial T}{\partial t} = \frac{q}{\kappa w} \quad (5.56)$$

$$\Rightarrow \frac{\partial T}{\partial t} = \frac{1}{c\rho w} q \quad (5.57)$$

The solution to this equation is,

$$T = \frac{q}{c\rho w} t + C \quad (5.58)$$

Clearly, the temperature of the membrane cannot obey this profile for all time, since this would lead to an infinite surface temperature. However, for small times immediately after the step in thermal flux input, this is most likely a good approximation for the shape of the temperature profile. To find the approximate time constant using this equation, the assumption is made that the line described by Equation 5.58 is tangent to the “actual” temperature vs. time profile, as shown in Figure 5.9. The time constant is then defined to be the time at which this tangent line crosses the final membrane central temperature (ΔT),

$$\tau = \frac{c\rho w \Delta T}{\Delta q} \quad (5.59)$$

Using Equation 5.11, a relation for the change in temperature (ΔT) for a given change in thermal flux (Δq) can be found,

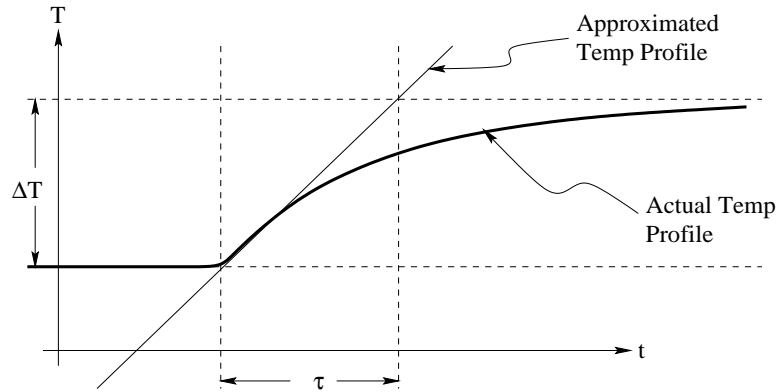


Figure 5.9: Approximation used to calculate the sensor time constant.

$$\frac{\Delta T}{\Delta q} = \frac{D^2}{16\kappa w} \quad (5.60)$$

Combining Equations 5.59 and 5.60, the time-constant for the Gardon membrane can be found,

$$\tau = \frac{c\rho D^2}{16\kappa} \quad (5.61)$$

5.6.5 Thermal Noise

Resistive elements naturally produce thermal (“Johnson”) electrical noise at their terminals. This noise is white, and its amplitude is proportional to the temperature of the resistor, as well as the absolute resistance, according to the relation [81],

$$V_{\text{Johnson,RMS}} = \sqrt{4k_B\Delta fTR} \quad (5.62)$$

where k_B is Boltzmann’s constant ($1.38 \times 10^{-23} \frac{J}{K}$), Δf is the frequency bandwidth of interest, T is the temperature in Kelvin, and R is the resistance. For the Wheatstone bridge arrangement shown in Figure 5.6, four thermal noise sources (one per resistor) add to give the output terminal thermal noise. Assuming the resistances do not change

appreciably during measurement, and that the resistance is given by Equation 5.44, this results in an output noise voltage of,

$$V_{\text{Johnson,RMS}} = \frac{2b}{\lambda} \sqrt{2k_B \Delta f T \rho_s} \quad (5.63)$$

In order to see how this affects the thermal flux measurement, this noise voltage can be translated into an equivalent input thermal flux noise by simply dividing by the sensitivity of the sensor,

$$q_{\text{n,equiv,chem}} = \frac{V_{\text{noise,RMS}}}{S_{\text{chem}}} = \frac{128b\kappa w \sqrt{2k_B \Delta f T \rho_s}}{\alpha \lambda D^2 V_{DD}} \quad (5.64)$$

$$q_{\text{n,equiv,ion}} = \frac{V_{\text{noise,RMS}}}{S_{\text{ion}}} = \frac{64b\kappa w \sqrt{2k_B \Delta f T \rho_s}}{\alpha \lambda D^2 V_{DD}} \quad (5.65)$$

$$(5.66)$$

5.7 Sensitivity Problem

The Gardon-gauge structure, used with the dual-sensor methodology described in Section 5.3, presents a serious design problem. In the dual-sensor scheme, one of the sensors must be coated with another material, to provide an etched surface to the plasma. However, if this material is thermally conductive, then the overall thermal conductivity of the membrane will be dramatically higher,

$$\kappa_{\text{stack}} = \frac{\kappa_1 t_1 + \kappa_2 t_2}{t_1 + t_2} \approx \frac{1}{2} \kappa_2 \quad \text{for } \kappa_2 \gg \kappa_1, t_1 \approx t_2 \quad (5.67)$$

where κ_x and t_x are the thermal conductivities and thicknesses of each layer. Equation 5.67 shows that for a thermally conductive layer (high κ) added to an insulator (low κ), the overall thermal conductivity approaches that of the conductor. As most etched layers of interest (polysilicon, photoresist, aluminum, etc.) are highly thermally conductive compared to the relevant membrane materials (silicon dioxide, silicon nitride), the etched layers dominate. Equations 5.37 and 5.38 reveal that the

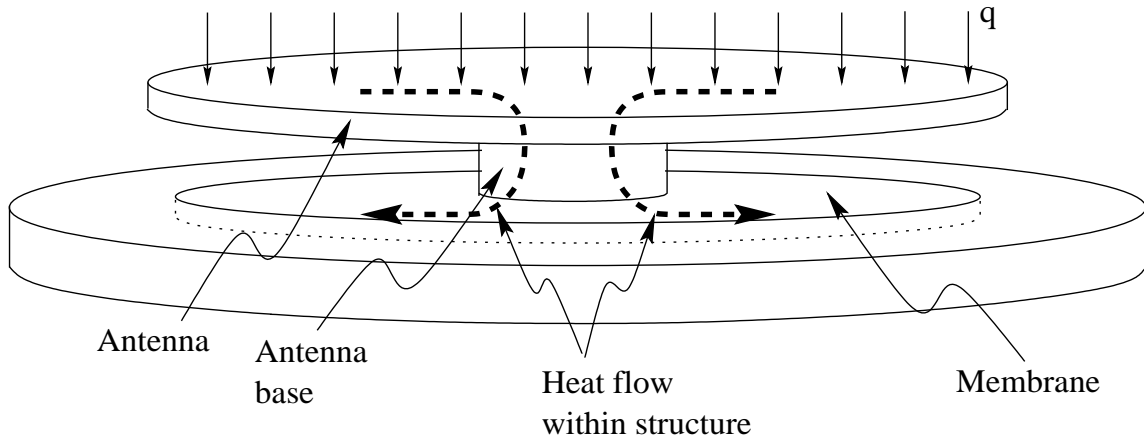


Figure 5.10: Modified thermal flux sensor design, with added heat-funneling antenna. Note: the vertical scale is exaggerated for clarity.

sensitivity of the Gardon structure is inversely proportional to the conductivity of the membrane. As a result, this dramatic increase in κ results in a significant decrease in overall sensitivity.

5.8 Modified Gardon Gauge: Operation

For the reasons identified in Section 5.7, a modification must be made to the standard Gardon structure to retain its high sensitivity, while permitting a sacrificial layer to be added to its surface. For this purpose, we add an “antenna” structure to the top of the Gardon membrane (see Figure 5.10). This modification offers several benefits. In this structure, the heat strikes the top of the antenna, flows inward to the center of the antenna, flows down into the membrane, and then exits the structure through the membrane at the edge. First, because all of the heat flows outward from the center of the structure to the edge, more of a thermal drop is experienced by the membrane, and the sensitivity is consequently increased. It will be shown in Section 5.9 that the sensitivity of this modified structure (to ion flux heating) is given by the equation,

$$S_{\text{ion}} = \frac{\alpha a^2 V_{DD}}{8\kappa w} \ln\left(\frac{D}{b}\right) \quad (5.68)$$

where a is the diameter of the antenna, and b is the diameter of the supporting post. By comparison with Equation 5.38, it is evident that this is a factor of $4\frac{a^2}{D^2} \ln\left(\frac{D}{b}\right)$ larger than the standard structure. The second advantage of this structure over the traditional Gardon gauge is that the addition of a to-be-etched layer does not affect the sensitivity. Because this layer is applied to the antenna instead of the membrane, and the thermal conductivity of the antenna does not affect the sensitivity, this problem is eliminated. In fact, as we shall see in the next section, it is actually advantageous from the perspective of the sensor time constant to have a high-conductivity antenna structure.

5.9 Modified Gardon Gauge: Analysis

The analysis of this modified structure is very similar to that for the standard Gardon structure. Most of the sensor parameters are simply scaled by a constant, which relates to the increased sensitivity provided by the antenna. Figure 5.11 shows the new sensor's geometry, including relevant dimensions and parameters that will be used in this analysis.

5.9.1 Sensitivity

The addition of the antenna structure complicates the analysis of the overall sensitivity, because the heat now flows along a more complex path. All of the heat is assumed to enter through the antenna, flow into the base region of the membrane, and flow out through the membrane. Therefore, the analysis in Section 5.5 of the equivalent thermal flux due to resistive heating can be directly applied to this problem. In that analysis, a resistive heater provided heat to the membrane through a central region, and the equation relating the thermal drop to the applied power is

$$\frac{\Delta T_{\text{Modified}}}{\Delta T_{\text{Standard}}} = 4 \frac{a^2}{D^2} \ln \left(\frac{D}{b} \right) \quad (5.71)$$

Multiplying the sensitivities given in Equations 5.37 and 5.38 by this factor yields,

$$S_{\text{chem}} = \frac{\alpha a^2 V_{DD}}{16 \kappa w} \ln \left(\frac{D}{b} \right) \quad (5.72)$$

$$S_{\text{ion}} = \frac{\alpha a^2 V_{DD}}{8 \kappa w} \ln \left(\frac{D}{b} \right) \quad (5.73)$$

5.9.2 Responsivity

Responsivity is calculated in the same way for the modified structure as it is for the standard Gardon structure, and the result is,

$$R_{\text{chem}} = \frac{\alpha V_{DD}}{4 \pi \kappa w} \ln \left(\frac{D}{b} \right) \quad (5.74)$$

$$R_{\text{ion}} = \frac{\alpha V_{DD}}{2 \pi \kappa w} \ln \left(\frac{D}{b} \right) \quad (5.75)$$

5.9.3 Power Dissipation

The analysis of the temperature drop across the membrane due to resistive heating of the central resistor applies in exactly the same way to the modified Gardon structure. Comparing Equation 5.52 to the new relation for ΔT during thermal flux measurement (Equation 5.70), it is straightforward to derive the new equivalence between external thermal flux and central resistor measurement heating,

$$\frac{q_{\text{external}}}{P_{\text{electrical}}} = \frac{1}{\pi a^2} \quad (5.76)$$

Plugging Equation 5.54 into Equation 5.76 yields,

$$q_{\text{p,equiv}} = \left(\frac{\lambda V_{DD}}{\pi a b} \right)^2 \frac{2}{\rho_s} \quad (5.77)$$

5.9.4 Time Constant

Because the antenna is assumed to be more conductive than the membrane, and because the antenna is directly connected (through the base) to the central resistor, it is assumed that the overall thermal response of the sensor is governed by the response of the antenna alone. Given this assumption, the time constant analysis of Section 5.5 can be directly used. Combining Equation 5.59 with Equation 5.70, the time constant for the modified Gardon structure is found to be,

$$\tau = \frac{c_{\text{ant}}\rho_{\text{ant}}ha^2}{4\kappa w} \ln\left(\frac{D}{b}\right) \quad (5.78)$$

where c_{ant} and ρ_{ant} are the specific heat and material density, respectively, for the antenna structure.

5.9.5 Thermal Noise

The Johnson thermal noise voltage at the output terminals is exactly the same for this sensor as for the standard Gardon gauge. The only difference in analysis is that the sensitivity is different between the two, and the new equivalent input thermal flux noise is,

$$q_{\text{n,equiv,chem}} = \frac{32b\kappa w\sqrt{2k_B\Delta fT\rho_s}}{\alpha\lambda a^2 V_{DD} \ln\left(\frac{D}{b}\right)} \quad (5.79)$$

$$q_{\text{n,equiv,ion}} = \frac{16b\kappa w\sqrt{2k_B\Delta fT\rho_s}}{\alpha\lambda a^2 V_{DD} \ln\left(\frac{D}{b}\right)} \quad (5.80)$$

5.9.6 Antenna Deflection

Because the modified Gardon structure contains a free-standing antenna, an analysis must be performed to find the deflection of this structure. If the deflection under its own weight is greater than the spacing between the antenna and the membrane

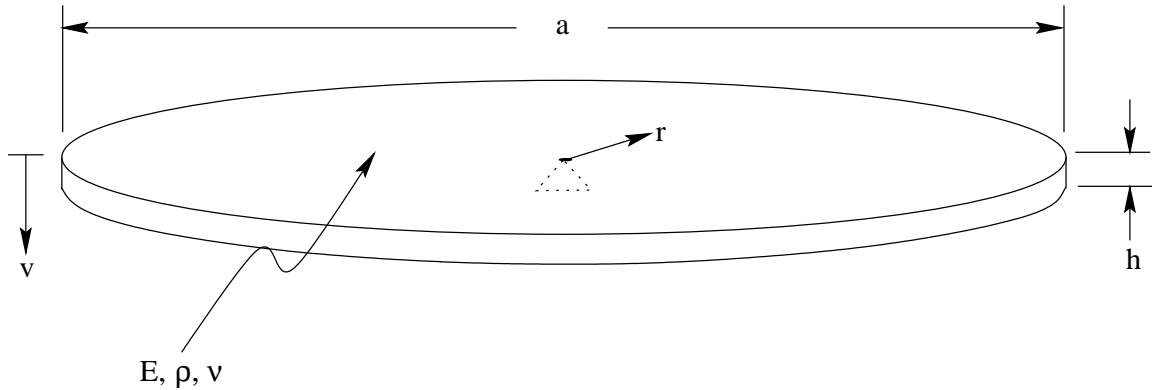


Figure 5.12: Model used for calculation of antenna flexure due to gravity. The dotted triangle indicates the support point.

(δ), then the two will touch and heat will transfer through the contact point. Because the assumption is made in all of the above analyses that heat flows through the central support only, this condition must be avoided.

It is assumed that the antenna can be modeled as a thin, uniform disk supported at a single point in the center (see Figure 5.12). It is further assumed that the only force acting on the disk is gravity. While other forces could act on the disk (due to motion of the sensor wafer, or vibration of the supporting surface), each of these forces will be proportional to the gravitational force. Contact forces will not be related to the gravitational force, and these will in fact be much larger in magnitude than gravitational forces; therefore, contact to the structure should be avoided to keep from damaging the structure.

For a thin plate structure, the equation relating deflection to applied pressure is given by [82],

$$\nabla^2 \nabla^2 v = \frac{1}{D} P(r, \theta) \quad (5.81)$$

where v defines the downward deflection of the plate at a location (r, θ) , $P(r, \theta)$ is the applied pressure field, and D is called the “flexural rigidity” of the plate, which is given by [82],

$$D = \frac{1}{12} \left(\frac{Eh^3}{1 - \nu^2} \right) \quad (5.82)$$

where E and ν are the elastic modulus and Poisson's ratio, respectively, for the antenna material, and h is the thickness of the antenna. For gravitational loading only, $P = \rho gh$, and Equations 5.81 and 5.82 can be combined to yield,

$$\nabla^2 \nabla^2 v = \frac{12\rho g(1 - \nu^2)}{Eh^2} \quad (5.83)$$

If radial symmetry is assumed, then,

$$\nabla^2 v = \frac{\partial^2 v}{\partial r^2} + \frac{1}{r} \frac{\partial v}{\partial r} \equiv v_{rr} + \frac{1}{r} v_r \quad (5.84)$$

Plugging this relation into Equation 5.83 yields,

$$v_{rrrr} + \frac{2}{r} v_{rrr} - \frac{1}{r^2} v_{rr} + \frac{1}{r^3} v_r = \frac{12\rho g(1 - \nu^2)}{Eh^2} \quad (5.85)$$

The general solution to this fourth-order non-homogeneous ordinary differential equation is,

$$v(r) = Ar^2 + B \ln r + Er^2 \ln r + F + \frac{3\rho g(1 - \nu^2)}{16Eh^2} r^4 \quad (5.86)$$

The boundary conditions for Equation 5.86 are that the deflection is zero at the center ($v(0) \equiv 0$), the plate is flat at the center ($v_r(0) = 0$), there is no shear force at the plate edge ($v_r(\frac{1}{2}a) = 0$), and there is no bending moment at the plate edge ($v_{rr}(\frac{1}{2}a) = 0$). The solution of Equation 5.86 subject to these boundary conditions is,

$$v(r) = \frac{3\rho g(1 - \nu^2)}{16Eh^2} \left(r^4 - a^2 r^2 \ln \left(\frac{2r}{a} \right) \right) \quad (5.87)$$

and the maximum deflection (occurring at $r = \frac{1}{2}a$) is,

$$v_{\max, \text{antenna}} = \frac{3\rho g a^4 (1 - \nu^2)}{256 E h^2} \quad (5.88)$$

Because the antenna is supported by a post sitting on an edge-supported membrane, this membrane will also deflect under both its own weight and the weight of the antenna acting at the center. This deflection can be found by solving,

$$v_{rrrr} + \frac{2}{r} v_{rrr} - \frac{1}{r^2} v_{rr} + \frac{1}{r^3} v_r = \frac{12\rho_i g (1 - \nu_i^2)}{E w^2} + W \Pi(b) \quad (5.89)$$

where ρ_i , ν_i , and w are the properties of the membrane, W is the total weight of the antenna, and $\Pi(b)$ is the function defined by,

$$\Pi(b) = \begin{cases} 1 & \text{for } r \leq b \\ 0 & \text{for } r > b \end{cases} \quad (5.90)$$

The weight of the antenna is simply the density times the volume,

$$W = \pi a^2 h \rho g \quad (5.91)$$

For the membrane, the following boundary conditions apply: the deflection at the edge is defined to be zero ($v\left(\frac{D}{2}\right) \equiv 0$), the edge is rigidly supported ($v_r\left(\frac{D}{2}\right) = 0$), the membrane is flat at the edge of the center post ($v_r\left(\frac{b}{2}\right) = 0$), and the shear force at the edge is equal to the total force load ($v_{rrr}\left(\frac{D}{2}\right) = W + \rho_i \pi \frac{D^2}{4} w g$). Assuming the support post is small compared to the size of the membrane, the solution of Equation 5.89 subject to these boundary conditions can be approximated as the sum of the deflection due to the membrane weight and the deflection due to the antenna weight at the center. In this case, the maximum deflection is [83],

$$v_{\max, \text{membrane}} \approx v_{\text{ant}} + v_{\text{memb}} = \frac{3a^2 h \rho g D^2 (1 - \nu_i^2)}{4w^2 E} + \frac{3\rho_i g D^4 (1 - \nu_i^2)}{4w^2 E} \quad (5.92)$$

Adding Equation 5.88 to Equation 5.92, the total deflection of the entire structure is,

$$v_{\max} = \frac{3\rho g a^4 (1 - \nu^2)}{256 E h^2} + \frac{3a^2 h \rho g D^2 (1 - \nu_i^2)}{4w^2 E} + \frac{3\rho_i g D^4 (1 - \nu_i^2)}{4w^2 E} \quad (5.93)$$

5.9.7 Built-in stress

Any residual stress in the antenna structure resulting from the fabrication process will cause warping of the antenna. If the vertical stress gradient is positive (higher tensile stress at the top of the structure), then the antenna will bow up, and become shaped like a bowl. The inverse is also true. Therefore, the fabrication process must be carefully planned and controlled, to avoid these gradients.

An analytical formula for the amount and direction of curvature would not be very useful for planning, since available models for the stress resulting from a given process are typically empirical, and usually approximate. Therefore, detailed stress gradient analysis will not be performed, and processing techniques will instead be used to minimize this type of stress as much as possible.

5.9.8 Parasitic Heat Transfer

The analysis of heat loss mechanisms performed in Section 5.5 applies to nearly every aspect of the modified Gardon structure. The heat loss from the top of the antenna will be analogous to the heat loss calculated for the top of the membrane in the standard gauge. Because there is still a “pit” beneath the membrane, all of the heat loss calculations will still apply to the pit underneath the modified structure. The only analysis that must be added is to calculate the heat transfer between the bottom of the antenna structure and the top of the membrane. Any heat transfer here will serve to make the antenna “transparent” to heat, which will bring the structure’s sensitivity closer to the standard Gardon membrane.

Because the temperature difference between the antenna and the membrane is expected to be only a degree or two, the previous analysis of radiation between the

membrane and the substrate applies in the same way. Using the same technique, the thermal flux from the antenna to the membrane is $12\frac{W}{m^2}$, or 1% of the typical thermal flux being measured.

Because the pressures are the same as in the previous analysis, the same argument can be used to show that convection heat transfer between the antenna and the membrane can easily be neglected.

Because radiation and convection heat transfer across the thin gap between the antenna and the membrane can both be neglected, conduction is all that must be calculated. Putting Equations 5.29, 5.31, and 5.32 together, a relation for the heat transfer can be found,

$$q = \frac{P}{50\mu mT} k_{\text{cond},760\text{T}} (T - T_{\text{surr}}) \quad \text{for} \quad P < \left(\frac{50\mu mT}{L} \right) \quad (5.94)$$

where L is the dimension of the containment vessel. Equation 5.94 shows that for pressures below a certain pressure limit, the thermal flux is only a function of pressure and the temperature gradient. For a pressure of $20mT$ and a temperature gradient of $2K$, the conductive thermal flux is $200\frac{W}{m^2}$, which is 20% of the typical value. This is a significant portion of the total thermal flux, and it has the effect of reducing the sensitivity of the modified structure. In the limiting case, where all externally applied thermal flux “leaks” through the antenna to the membrane, the sensitivity will approach the sensitivity of the standard Gardon structure. However, even in this case the antenna still serves its primary purpose: to allow the addition of a conductive “etched” material to the Gardon structure.

5.9.9 Analysis Summary

The results of the analysis performed in Sections 5.5 and 5.9 are summarized in Table 5.1. From this table, it can be readily observed that the “modified” Gardon structure offers an improvement of $4\frac{a^2}{D^2} \ln\left(\frac{D}{b}\right)$ for most parameters.

Parameter	Symbol	Standard Gardon Gauge	“Modified” Gardon Gauge
Sensitivity (chemical)	S_{chem}	$\frac{\alpha D^2 V_{DD}}{64\kappa w}$	$\frac{\alpha a^2 V_{DD}}{16\kappa w} \ln\left(\frac{D}{b}\right)$
Sensitivity (ion flux)	S_{ion}	$\frac{\alpha D^2 V_{DD}}{32\kappa w}$	$\frac{\alpha a^2 V_{DD}}{8\kappa w} \ln\left(\frac{D}{b}\right)$
Responsivity (chemical)	R_{chem}	$\frac{\alpha V_{DD}}{16\pi\kappa w}$	$\frac{\alpha V_{DD}}{4\pi\kappa w} \ln\left(\frac{D}{b}\right)$
Responsivity (ion flux)	R_{ion}	$\frac{\alpha V_{DD}}{8\pi\kappa w}$	$\frac{\alpha V_{DD}}{2\pi\kappa w} \ln\left(\frac{D}{b}\right)$
Equivalent Heating	$q_{\text{p,equiv}}$	$\left(\frac{\lambda V_{DD}}{\pi D b}\right)^2 \frac{8}{\rho_s} \ln\left(\frac{D}{b}\right)$	$\left(\frac{\lambda V_{DD}}{\pi a b}\right)^2 \frac{2}{\rho_s}$
Time Constant	τ	$\frac{c\rho D^3}{16\kappa}$	$\frac{c_{\text{ant}}\rho_{\text{ant}}ha^2}{4\kappa w} \ln\left(\frac{D}{b}\right)$
Input-Referred Thermal Noise (chemical)	$q_{\text{n,equiv,chem}}$	$\frac{128b\kappa w\sqrt{2k_B\Delta f T\rho_s}}{\alpha\lambda D^2 V_{DD}}$	$\frac{32b\kappa w\sqrt{2k_B\Delta f T\rho_s}}{\alpha\lambda a^2 V_{DD} \ln\left(\frac{D}{b}\right)}$
Input-Referred Thermal Noise (ion flux)	$q_{\text{n,equiv,ion}}$	$\frac{64b\kappa w\sqrt{2k_B\Delta f T\rho_s}}{\alpha\lambda D^2 V_{DD}}$	$\frac{16b\kappa w\sqrt{2k_B\Delta f T\rho_s}}{\alpha\lambda a^2 V_{DD} \ln\left(\frac{D}{b}\right)}$
Physical Deflection	v_{max}	N/A	$\frac{3\rho g a^4(1-\nu^2)}{256Eh^2} + \frac{3a^2 h\rho g D^2(1-\nu_i^2)}{4w^2 E} + \frac{3\rho_i g D^4(1-\nu_i^2)}{4w^2 E}$

Table 5.1: Summary of analytical results for both the standard Gardon gauge structure and the “modified” Gardon structure.

5.10 Numerical Optimization of Modified Gauge

5.10.1 Optimization Setup

To design the optimal modified Gardon gauge structure, Matlab [84] was used to perform a numerical optimization. The equations from Table 5.1 were entered into a Matlab function (`sim_structure.m`, listed in Appendix D), so that the performance parameters of a particular geometry could be quickly evaluated. Then, a nonlinear cost function and seven nonlinear boundary conditions were formulated and entered into two Matlab functions (`optfun.m` and `optnonlcon.m`, respectively, also listed in Appendix D). Since the goal of the optimization was to design a sensor with maximum sensitivity, the cost function (J) was chosen to be the negative of the sensitivity,

$$J = -\frac{\alpha a^2 V_{DD}}{8\kappa w} \ln\left(\frac{D}{b}\right) \quad (5.95)$$

To keep the optimization process “well-behaved”, meaning that the final design should be implementable using available fabrication techniques, several constraints were imposed. These are listed in Table 5.2. In addition, the free variables in the optimization were limited to reasonable values, and these ranges are shown in Table 5.4.

The first two constraints ensure that the resulting structure is properly characterized by the analysis performed in Section 5.9. For example, if the antenna were smaller than the membrane, then some of the incident heat would strike the membrane directly, and this is not taken into account in the analysis. Also, if the central post is too large, then the assumption that it is at a uniform temperature will not be valid.

Constraint #3 states that the edges of the structure should not bend down by more than $0.1\mu m$, to avoid touching the edge of the membrane. If this occurs, then most of the heat will flow outward through that contact point, rather than inward through the post, which will reduce the sensitivity from the calculated value.

To make sure that the parasitic heat transfer modes do not become significant,

#	Description	Constraint Equation
1	The antenna must be larger than or equal to the membrane	$D - a \leq 0$
2	The center post should have less than 10% the diameter of the membrane	$10 - D/b \leq 0$
3	The maximum deflection should be less than 0.1um	$v_{\max} - 0.1 \leq 0$
4	The total temperature drop from antenna to substrate should be less than 4 °C	$\Delta T_{\text{ant}} + \Delta T_{\text{memb}} - 4 \leq 0$
5	Equivalent resistive heating should be less than 10% of measured heat flux	$q_{\text{equiv}}/q_{\text{applied}} - 0.1 \leq 0$
6	Time constant should be less than 0.3s	$\tau - 0.3 \leq 0$
7	1% of scale reading should be 3 times greater than noise	$3 - S * (0.01) * q_{\text{applied}}/V_{\text{rms}} \leq 0$

Table 5.2: Constraints imposed on numerical optimization of modified Gardon structure.

constraint #4 requires that the temperature difference across the structure remain below 4°C . If this temperature difference were too high, conductive heat losses through the gap would become comparable to the incident thermal flux. In addition, for plasma processes, a much higher temperature at the center of the structure might begin to cause differences in the reaction rate at that location, adversely affecting the measurement.

The fifth constraint states that the equivalent heating due to electrical measurement should contribute no more than 10% of the total heat flux to the structure. This is to avoid loss of accuracy due to this “extra” thermal flux.

Constraint #6 requires the time constant of the sensor to be less than 0.3s. This is a performance requirement, chosen to match the approximate speed of the plasma behaviors that we are interested in. While many plasma effects occur on the kilohertz or megahertz time scales, we are ignoring those effects for now.

The last constraint imposes the restriction that the signal-to-noise ratio at 1% of full-scale should be at least 3. This ensures that the measurement will not be corrupted by this type of noise.

5.10.2 Optimization Results

To solve the optimization problem posed in Section 5.10.1, the Matlab routine `fmincon` was used (see the `optimization.m` file in Appendix D for the calling sequence). This routine is a nonlinear constrained optimization solver, which uses nonlinear programming techniques to find the problem solution. The numerical parameters used in the optimization are given in Table 5.3, and the allowed range for each of the geometrical parameters is shown in Table 5.4.

Using `fmincon`, the optimal structure was found, and its geometrical and performance parameters are shown in Table 5.5. Appendix D, Section D.5 shows the detailed output from the program. The optimal structure for the given constraints

Parameter	Symbol	Value
Thermal Flux	q	$1000 \frac{W}{m^2}$
Resistor Material	-	Phosphorus-doped polysilicon
Temperature Coef. of Resistivity	α	$0.001 K^{-1}$
Sheet Resistance	ρ_s	$20 \frac{\text{Ohm}}{\square}$
Membrane Material	-	Low-stress silicon nitride
Thermal Conductivity	κ	$16 \frac{W}{mK}$
Specific Heat	c	$691 \frac{J}{kgK}$
Material Density	ρ	$2400 \frac{kg}{m^3}$
Thickness	w	$0.5 \mu m$
Antenna Material	-	Undoped polysilicon
Specific Heat	c_{ant}	$712 \frac{J}{kgK}$
Material Density	ρ_{ant}	$2331 \frac{kg}{m^3}$
Thickness	h	$1.2 \mu m$
Minimum Linewidth	λ	$3.5 \mu m$
Sensor Bandwidth	Δf	$50 Hz$
Average Substrate Temperature	T	$300 K$

Table 5.3: Summary of materials and process-related parameters used in Gardon gauge analysis. These factors are assumed to be fixed when considering geometrical tradeoffs.

Parameter	Symbol	Acceptable Range
Membrane Diameter	D	100 to 1000 μm
Antenna Diameter	a	100 to 1000 μm
Base Width	b	10 to 200 μm
Supply Voltage	V_{DD}	0.1 to 10V

Table 5.4: Summary of geometrical parameters used in Gardon gauge analysis. These factors may be tuned to maximize sensitivity.

and material choices yields a sensitivity (to ion flux) of $0.58 \frac{\mu V}{W/m^2}$ and a time constant of 0.01s. The sensor is 327 μm in diameter, has a post diameter of 32.7 μm , and uses a supply voltage of 0.25V. All of these figures are reasonable, and are in the right neighborhood for good manufacturability.

Geometrical Parameters		Performance Parameters	
Item	Value	Item	Value
Membrane diameter (D)	326.6 μm	Sensitivity (S_{ion})	$0.58 \frac{\mu V}{W/m^2}$
Antenna diameter (a)	326.6 μm	Time constant (τ)	0.01s
Antenna post diameter (b)	32.7 μm	Equivalent heat flux (q_{equiv})	100 $\frac{W}{m^2}$
Supply voltage (V_{DD})	0.25V	Equivalent noise (q_{rms})	0.07 $\frac{W}{m^2}$
		Maximum “droop” (v_{max})	1nm

Table 5.5: Results from Matlab optimization of the modified Gardon gauge structure

5.11 Modified Gardon Fabrication

5.11.1 Requirements

There were several challenges to fabricate a structure of the type described in Section 5.8. The most difficult of these challenges are described in this section.

Low Stress Membrane

One requirement was that the membrane material had to be low-stress, with no compressive stress at all. The reason for this is that any compressive stress would cause the membrane to buckle or “bulge”, which would distort the shape of the Gardon structure. With high tensile stress, there would be a high likelihood that the membrane would tear. To satisfy this requirement, low-stress nitride film (deposited by non-stoichiometric LPCVD of 4:1 $SiCl_2H_2:NH_3$) was used. LPCVD nitride is nearly always under tensile stress due to thermal mismatch with the silicon substrate. The excess silicon incorporated into the film by the non-stoichiometric recipe brings the thermal coefficient of expansion closer to the bulk silicon, reducing the stress level.

Highly Selective Release Etch

Another requirement was that an etchant needed to be used to clear out the space between the antenna and the membrane, and also the large space underneath the membrane. Because this sub-membrane cavity needed to be fairly large (to avoid excessive conduction heat losses to the substrate), the release etchant needed to be very selective to all other exposed substances. If the selectivity was too low, other parts of the structure would be etched away during the final release etch. To meet this requirement, XeF_2 etchant was selected. XeF_2 is a very rapid etchant (etch rates of up to $10 \frac{\mu m}{min}$ have been reported [85]), is highly selective to oxide (a 50\AA SiO_2 layer forms a hard mask [86]), and very selective to most other materials [85]. However, it was discovered during the fabrication of these devices that XeF_2 can attack SiN

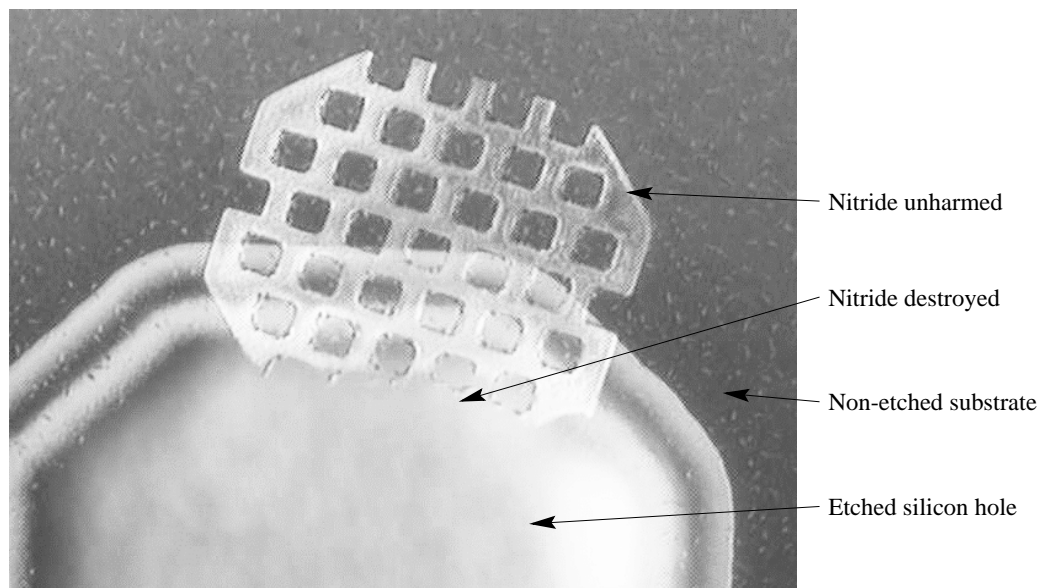


Figure 5.13: SEM image of nitride plate partially destroyed by XeF_2 etchant. The portion of the structure sitting on the surrounding material is not harmed by the etchant; however, the portion hanging over the edge of a pit being etched into the silicon is completely destroyed.

under some circumstances. Other researchers give conflicting reports on this matter: in [87], it is reported that stoichiometric nitride is etched at $120 \frac{\text{\AA}}{\text{min}}$ and low-stress nitride is etched at less than $2 \frac{\text{\AA}}{\text{min}}$; however, in [85] it is reported that stoichiometric nitride is not etched at all.

It was observed during experimentation that nitride in isolated areas was not etched by XeF_2 ; however, nitride that was near or over large areas of etched silicon *was* etched (see Figure 5.13 for an illustration of this fact). This is perhaps why the literature contains conflicting stories. If blanket layers of nitride were used to test the etch rate, it would be low, as no silicon etching would be taking place nearby.

Two theories could support this observation. One is that the temperature increase generated by the exothermic XeF_2/Si reaction increases the nitride etch rate. This would cause the observed behavior, because areas near the etched silicon would become hotter than those situated away from the etched regions. Another hypoth-

esis is that reaction byproducts from the XeF_2/Si reaction somehow catalyze the nitride etch process. Therefore, nitride near silicon regions would receive more etch byproducts, and would therefore etch more quickly.

To test these hypotheses, two experiments were conducted. In the first, the temperature effect was tested by attempting to reduce, as much as possible, the substrate temperature near etched areas. To accomplish this, the process chamber temperature was reduced from the standard operating setpoint of $40^\circ C$ to room temperature, $23^\circ C$. Also, the etch cycle time was increased to 1 minute from a standard time of 30 seconds, to allow the wafer more time to cool between cycles. Finally, the XeF_2 pressure was decreased to $0.7T$ and the nitrogen pressure was increased to $80T$, from their standard settings of $4T$ and $0T$, respectively. The purpose of this change was to decrease the average etch rate by reducing the available XeF_2 etchant at the surface of the wafer. This experiment had the effect of *decreasing* the selectivity to nitride, as opposed to increasing it. Therefore, it appears that temperature does not play a role in the XeF_2 / nitride etch reaction.

The second experiment was meant to test the reaction byproduct theory. In this experiment, the residence time of the XeF_2 in the process chamber was reduced to 7 seconds per cycle, from its typical 30 second value. The other settings were kept at “typical” values: $4T$ XeF_2 , $0T$ N_2 , $40^\circ C$ chamber temperature. By pumping out the process chamber immediately after each cycle, the reaction byproducts were quickly removed from the chamber. This experiment had the intended effect: the nitride etch selectivity was dramatically increased. Using this process, $120\mu m$ of substrate silicon was etched out from underneath a $0.5\mu m$ low-stress nitride plate, with only slight etching of the edges of the plate (see Figure 5.14).

Protected Antenna Structure

To build the modified Gardon structure, there needed to be a structural material to form the antenna, but this material had to be protected from the isotropic release

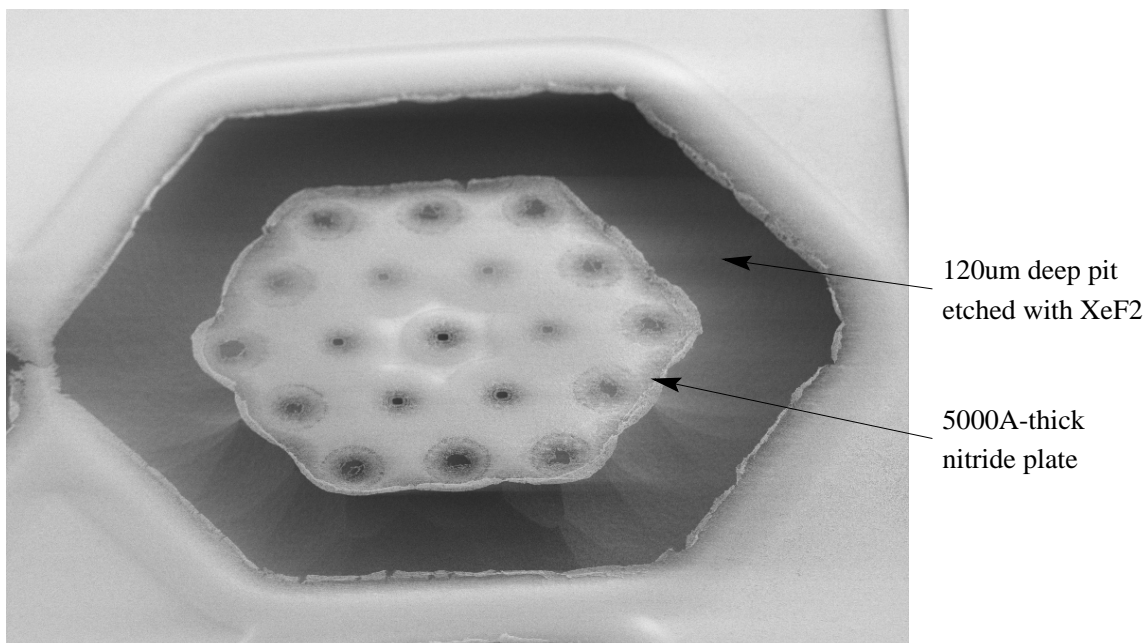


Figure 5.14: SEM image of $0.5\mu\text{m}$ nitride plate, supported in the middle, over the top of a $120\mu\text{m}$ pit etched into the silicon substrate by XeF_2 etchant.

etchant (XeF_2). One of the best, and most used, MEMS structural materials is polysilicon. However, polysilicon is attacked by XeF_2 etchant at nearly the same rate as single crystal silicon. Therefore, either a different structural layer was needed, or some kind of protective coating needed to surround the polysilicon.

The first technique, using a non-polysilicon antenna, was first attempted. Using this process, the antenna consisted of a SiO_2 / aluminum sandwich, supported at the center by SiO_2 . With a bi-layer structure, residual stress in each layer was critical, because it can cause residual bending of the structure. Care was taken to equalize the stress levels in each material by tuning the LPCVD LTO process, and by tuning the power and pressure settings for the aluminum sputtering process. However, even with this attempted matching, the residual stress was very different in the two layers, resulting in a highly distorted antenna structure (see Figure 5.15).

The second technique, using a purely polysilicon antenna structure, was then tried. To protect this polysilicon from the XeF_2 etch, an oxidation step before and

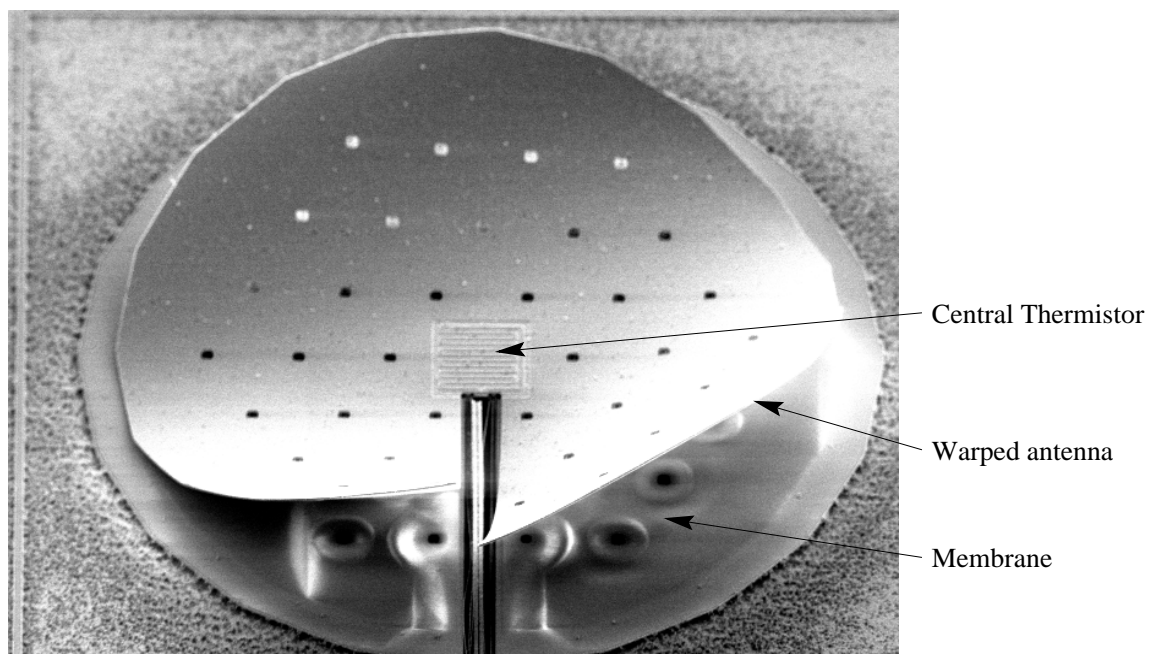


Figure 5.15: SEM image of modified Gardon structure with high levels of residual stress. This antenna was constructed using a SiO_2 / aluminum sandwich structure.

after polysilicon patterning was used. This oxidized the entire surface of the structural polysilicon with 1000\AA of SiO_2 , protecting it from the XeF_2 etch. While this increased the process complexity by one masking layer (to selectively etch away the protective oxide to provide through-holes), it provided the necessary stress-gradient free antenna structure.

5.11.2 Process Flow

To fabricate the structure shown diagrammatically in Figure 5.10, the process listed in Figure 5.16 was used. This process can be used to create a 5000\AA low stress nitride membrane, a doped polysilicon thermistor, a doped polysilicon sacrificial layer, a $1.2\mu\text{m}$ oxide-coated undoped polysilicon layer for the antenna structure, aluminum interconnections, polysilicon/aluminum overcrossings, and a sacrificial photoresist layer to be etched by the plasma process.

1. Start with $\langle 100 \rangle$ test-grade wafers
2. Deposit $0.5\mu m$ low-stress nitride via LPCVD
3. Pattern with NITRIDE mask
4. Plasma etch nitride using SF_6/He chemistry
5. Deposit $1.5\mu m$ phosphorus-doped polysilicon via LPCVD
6. Pattern with POLY mask
7. Plasma etch poly using HBr chemistry
8. Grow 1000\AA wet thermal oxide
9. Deposit $1.2\mu m$ undoped polysilicon
10. Pattern with STRUCTURE mask
11. Wet etch polysilicon in $64\%HNO_3/33\%H_2O/3\%NH_4F$, $3-4\mu m$ overetch
12. Grow 1000\AA wet thermal oxide
13. Pattern with STRUCTURE mask
14. Wet etch oxide in 5:1 BHF
15. Deposit $0.8\mu m$ aluminum/2% silicon via RF magnetron sputtering
16. Pattern with METAL mask
17. Wet etch aluminum in $80\%H_3PO_4/10\%H_2O/5\%CH_3COOH/5\%HNO_3$
18. Sinter aluminum, $400^\circ C$, N_2 , 20m
19. Pattern with ETCH mask ($2.0\mu m$ g-line resist)
20. Dice wafer
21. Release structures using XeF_2 etch

Figure 5.16: Simplified fabrication process for thermal flux sensor construction (see Appendix C for full process).

5.11.3 Final structure

The structures resulting from the process described in the previous section are shown in Figures 5.17, 5.18, 5.19, and 5.20. These figures show the antenna structure overall, as well as closeups of one corner of the antenna and etch holes. A cross-sectional view of the antenna, membrane, and sub-membrane cavity is shown in Figure 5.21. While the cleaving process used to expose the sensor sidewall breaks the membrane and fractures the silicon, the antenna is left whole. Therefore, in this figure the entire antenna can be seen at the top of the membrane. A closeup of the XeF_2 etched pit underneath the membrane is shown in Figure 5.22.

As shown in the figures, this process was successful. Both the photoresist-coated and uncoated antenna structures were relatively stress-free, with very little residual warping. The nitride membranes were left unharmed by the XeF_2 etch process, and these membranes were able to fully support the antenna structures. Low resistance electrical connections were successfully made to the central and outer doped polysilicon thermistors.

5.12 Experimental Results

5.12.1 Bench-top Experiment

To verify the functionality of the thermal flux sensor, it was attached to a computer-based data acquisition system (National Instruments AT-MIO/64-E3). The applied voltage, current, and sensor output voltages were all digitized and recorded by the computer. By applying a fixed voltage ($0.25V$) to a sensor, and measuring the three output voltages, the resistor connectivity and matching was evaluated.

First, both sensors (each consisting of three modified Gardon structures, one “etched” and the other two “non-etched”, connected in the Wheatstone bridge arrangement) on the die under test were determined to be functional. All twelve re-

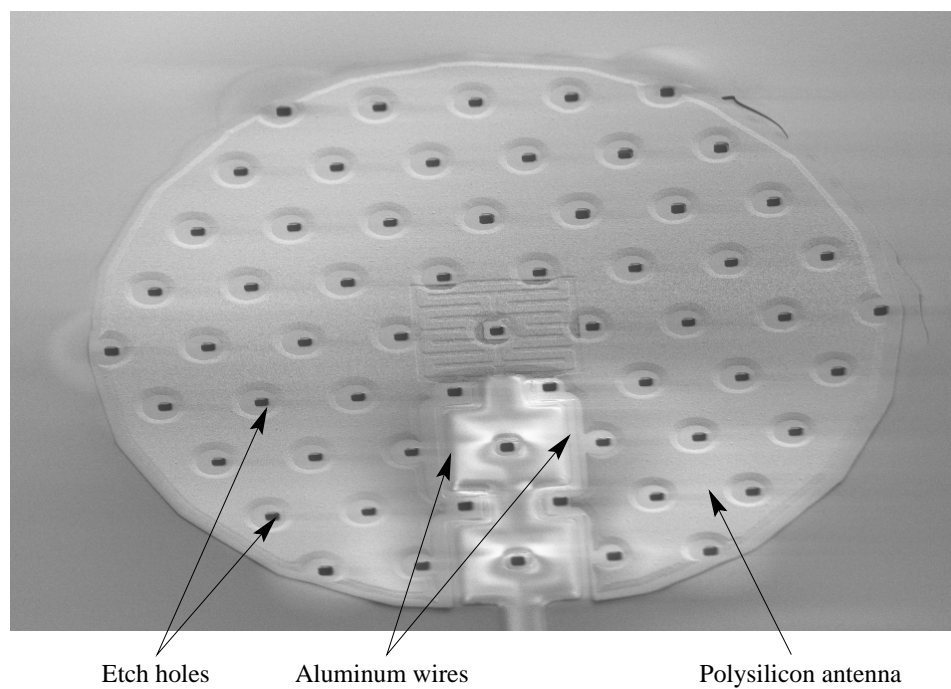


Figure 5.17: SEM image of modified Gardon structure, *without* photoresist coating.

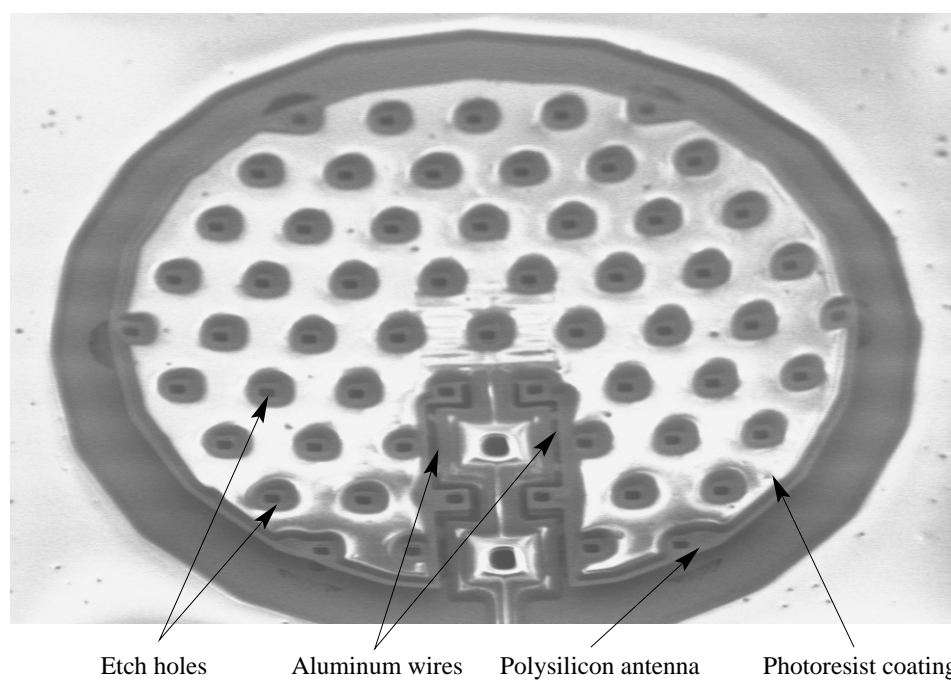


Figure 5.18: SEM image of modified Gardon structure, *with* photoresist coating.

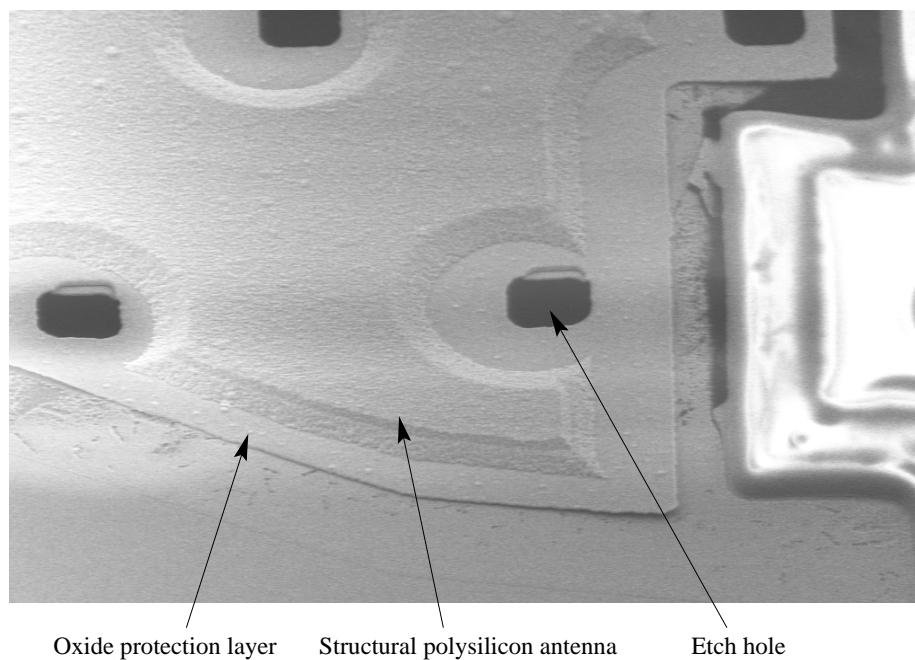


Figure 5.19: SEM image closeup of modified Gardon structure, *without* photoresist coating.

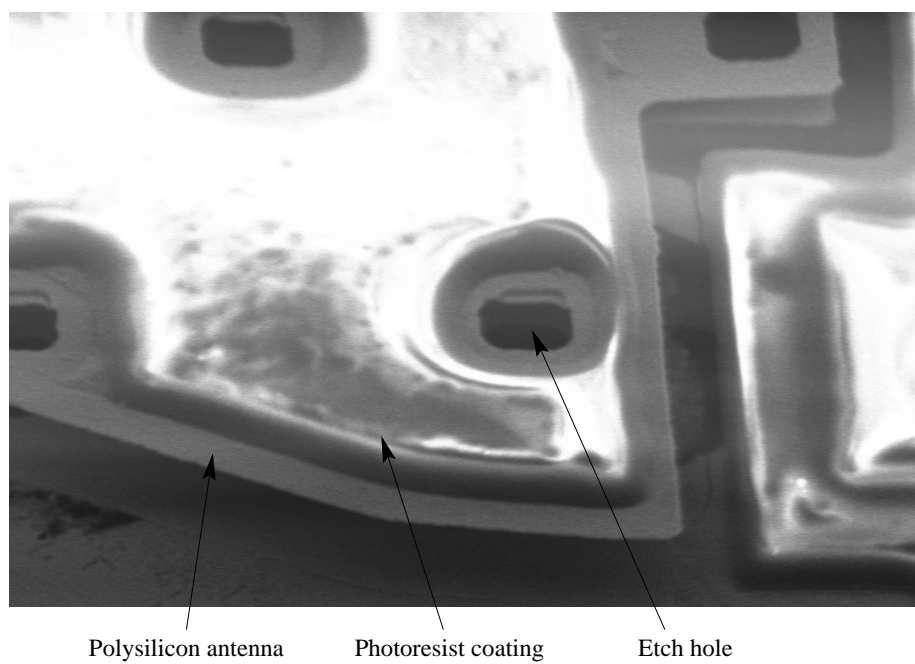


Figure 5.20: SEM image closeup of modified Gardon structure, *with* photoresist coating.

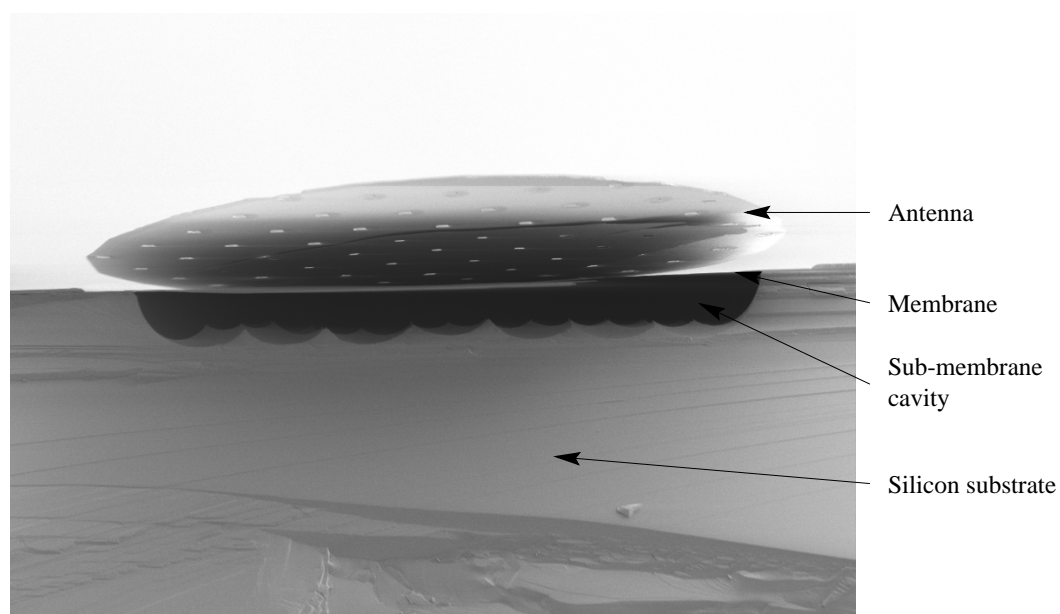


Figure 5.21: SEM image of cross section of modified Gardon structure, with complete antenna still present. The cleaving process breaks the wafer and membrane, but leaves the antenna intact, as shown.

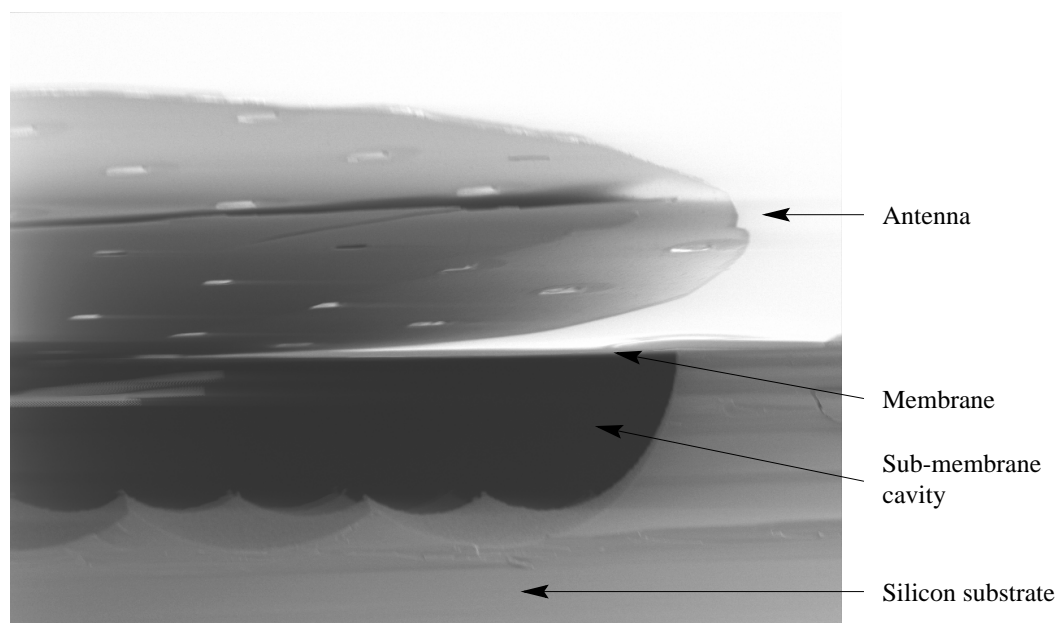


Figure 5.22: Closeup SEM image of sub-membrane pit etched with XeF_2 .

sistors were connected to the bridge, and all voltage outputs were reasonable. The six voltage outputs (for no applied thermal flux) were: 120.0mV, 123.1mV, 122.6mV, 124.5mV, 123.8mV, and 123.3mV; the supply voltage was 246.6mV. From these measurements, it is easy to see that the reference resistors are well matched to the center resistors on the Gardon structures. The matching for each structure was computed to be: 2.7%, 0.1%, 0.5%, 1.0%, 0.4%, and 0.0%, for an average of 0.8%.

5.12.2 Low Pressure Experiment

Experimental Setup

To verify the performance of the prototype sensor, a vacuum chamber experiment was designed. A stack containing a thin-film heater (Hukseflux Co., 100 Ω film heater), the chip containing the prototype thermal flux sensor, and an off-the-shelf thermal flux sensor (Hukseflux Co., HFP01SC Heat Flux Sensor), was assembled as shown in Figure 5.23. A photo of the heater and commercial thermal flux sensor is shown in Figure 5.24, and a photo of the edgeboard connector and prototype sensor is shown in Figure 5.25. The stack was placed into a vacuum chamber so that low pressure testing could be carried out. To make electrical connection to the sensors and the heater, a 25-wire vacuum feedthrough was constructed.

As shown in Figure 5.23, the heat from the thin-film heater flows both upward to the surrounding gas and downward through the stack. The heat that flows downward goes through both the prototype sensor and the commercial sensor; therefore, the thermal flux through each is identical. By comparing the readings from the prototype sensor to that of the commercial sensor, a calibration constant can be calculated.

Sensitivity Measurement

An experiment was performed in which the applied heat flux was stepped gradually upward through ten values. During the experiment, which lasted approximately 45

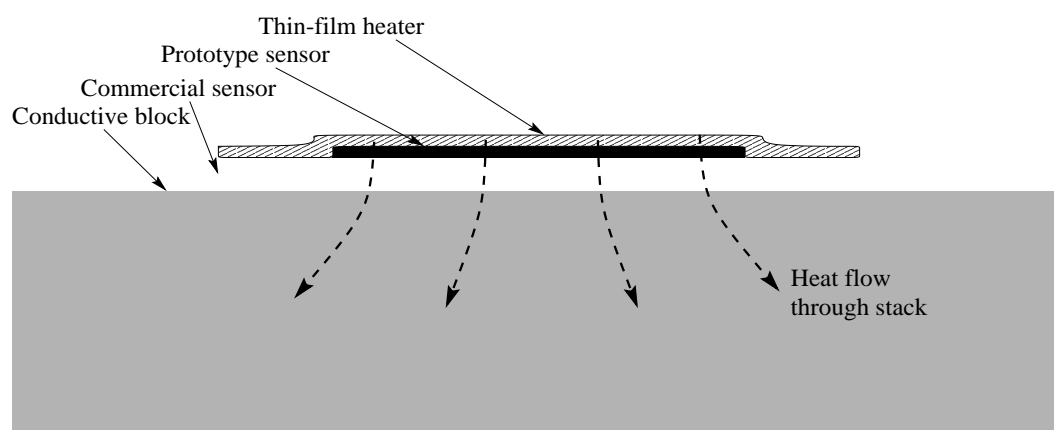


Figure 5.23: Diagram of experimental setup used to verify and calibrate the heatflux sensors.

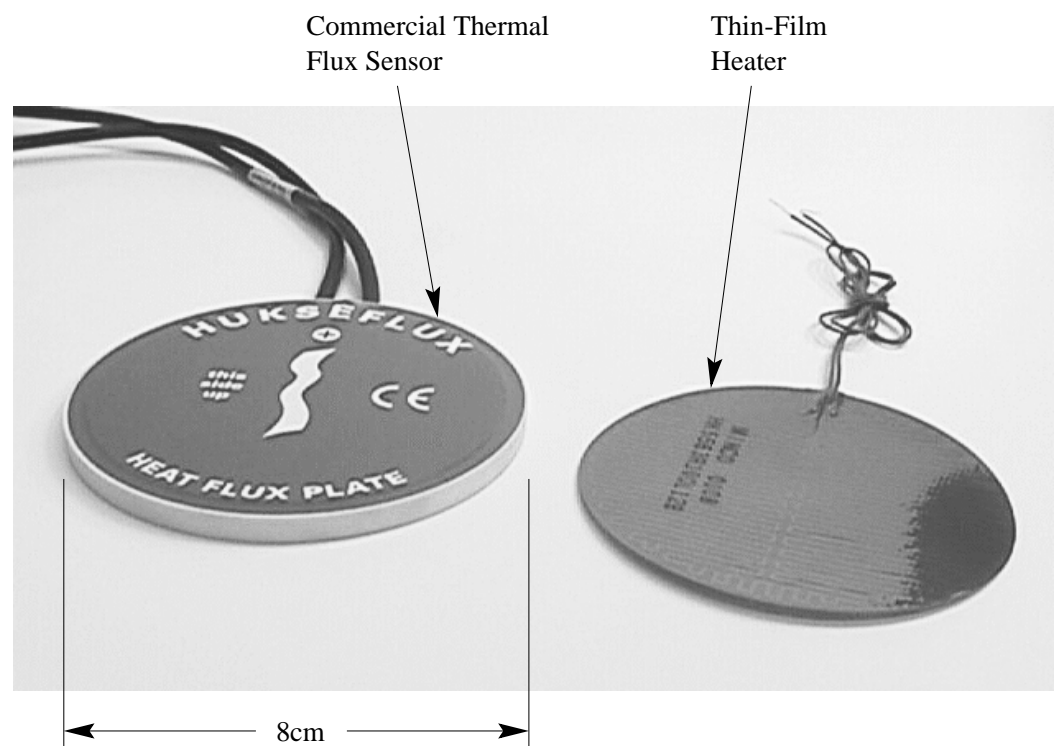


Figure 5.24: Photo of thin-film heater and off-the-shelf thermal flux sensor.

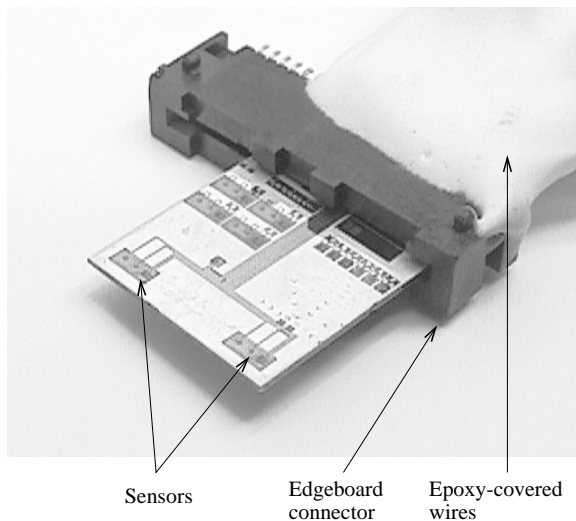


Figure 5.25: Photo of thermal flux sensor die connected to edgeboard connector.

minutes, both the prototype sensor outputs and the commercial sensor output were recorded. These data are shown in Figure 5.26. The measurements of V_{ion} accurately track the increases in thermal flux, while the measurements of V_{chem} stay relatively constant at zero. This is the expected behavior, since in this experiment the sensors are uniformly heated. As a result, the flux difference between the “etched” and “non-etched” Gardon structures is zero.

To find the calibration curve for the prototype sensor, the “final” value of each step was required. To accomplish this, a Matlab function (see Appendix D, Section D.6) was written to find the best-fit exponential curve for each of the steps, and output the asymptotic value for each. The routine finds the best three parameters, V_B , V_E , and τ , that minimize the error (ϵ),

$$\epsilon = \sum_k |y_{data,k} - \hat{y}_k| \quad (5.96)$$

$$\hat{y}_k = V_B + (V_E - V_B) \left(1 - e^{-\frac{kT}{\tau}}\right) \quad (5.97)$$

where T is the sampling rate, V_B is the “beginning” value of the exponential, V_E is the asymptotic limit, and τ is the time constant. In this way, the experiment could be

performed more quickly, because each step did not need to completely reach steady state; instead, the asymptotic value estimated by the program for each step could be used.

By plotting the “actual” heatflux values, as measured by the commercial sensor, to the voltage outputs from the prototype sensor, a calibration curve could be generated (see Figure 5.27). A regression line was fit to this plot; the line has a slope of $0.25 \frac{\mu V}{W/m^2}$, compared to the theoretical sensitivity (calculated in Section 5.9.1) of $0.58 \frac{\mu V}{W/m^2}$. From this number, the responsivity of the prototype sensor is calculated to be $3.0V/W$. For comparison, the responsivity of the commercial sensor is $0.031V/W$, two orders of magnitude less.

The most likely explanation for the reduced sensitivity is that the parasitic heat loss mechanisms described in Section 5.9.8 are significant. This experiment was conducted at $1.5T$, which is significantly higher than the $20mT$ design pressure. However, as will be described below, other difficulties arose when an attempt was made to test at this pressure.

Repeatability Measurement

The prototype sensor’s repeatability was found by calculating the standard deviation of a section of data during which the applied thermal flux was constant. Using the sensitivity derived above, the $3\text{-}\sigma$ repeatability is $8.3 W/m^2$, or about 0.8% of the expected full scale value.

Time Constant Measurement

To compute the sensor’s time constant, the τ parameter from the Matlab routine (described in the Sensitivity section above) was used as an estimate. For the data set shown in Figure 5.26, the average time constant over all steps was 19.0 seconds. This value is three orders of magnitude slower than the theoretically calculated value of 0.01 seconds.

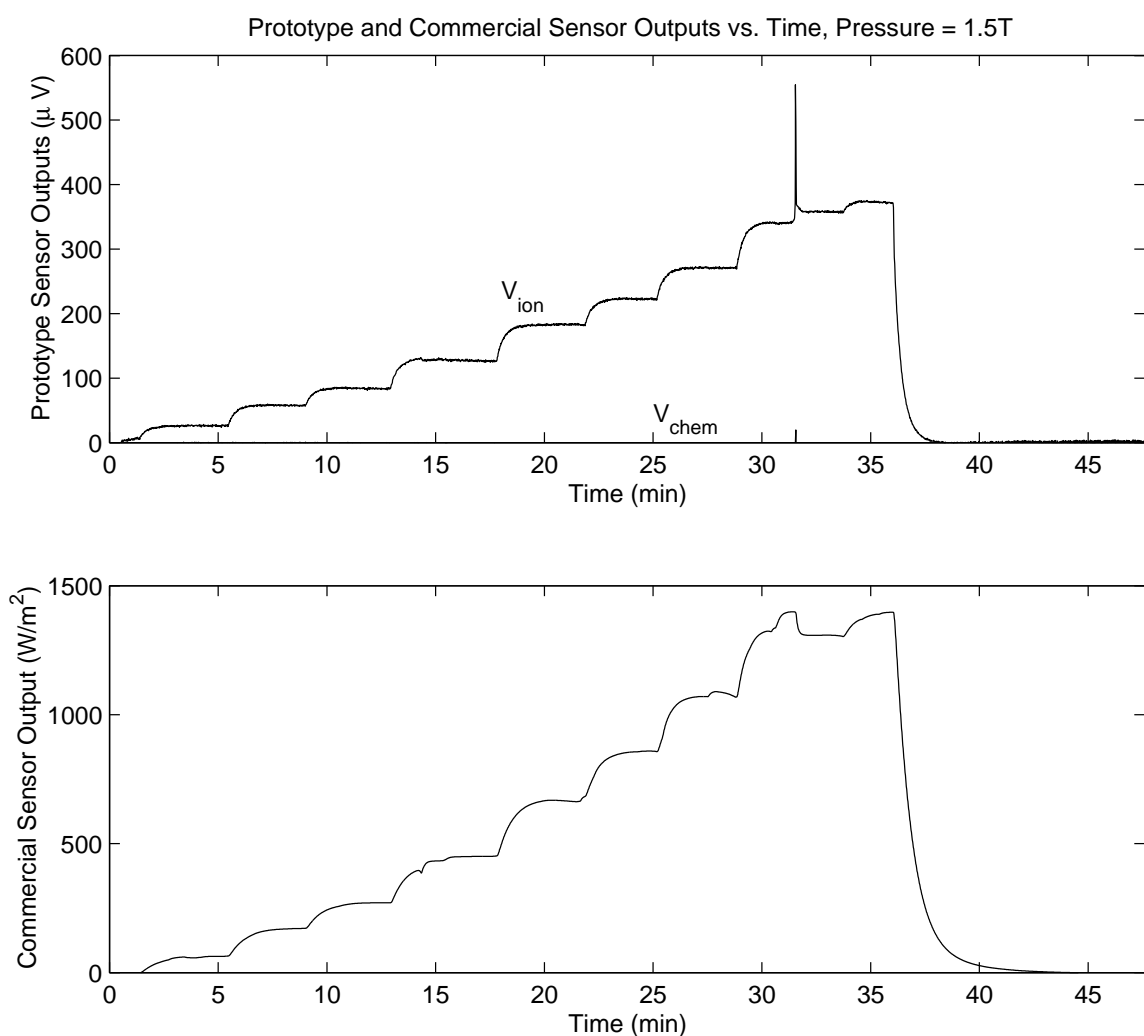


Figure 5.26: Plot of sensor voltage output and commercial sensor output vs. time. This experiment was conducted inside a vacuum chamber, at a pressure of 1.5T. An electrical glitch was observed 31.5 minutes into the experiment; this section of data was ignored in the analysis.

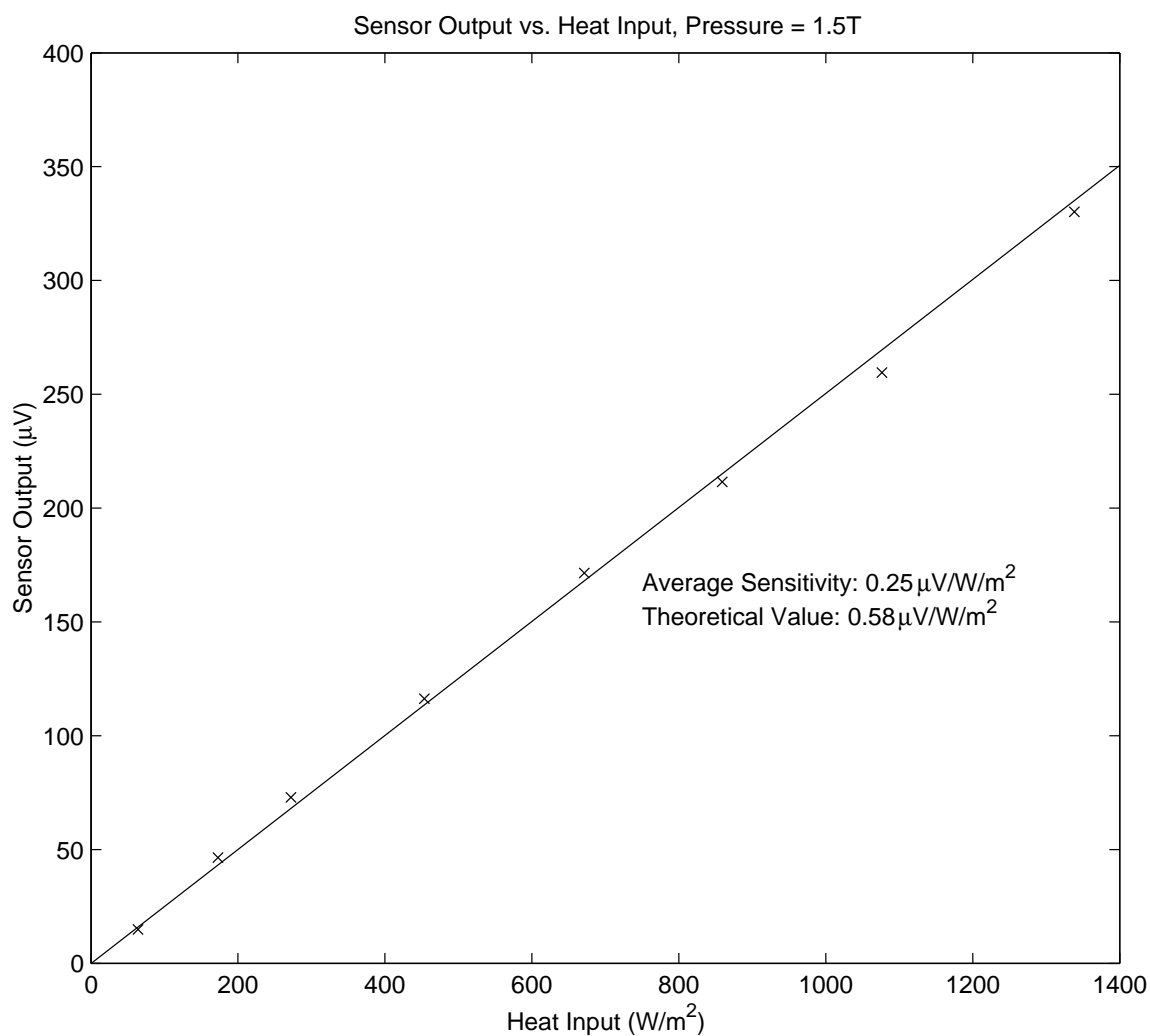


Figure 5.27: Calibration curve showing sensor voltage output vs. measured thermal flux. Also shown is a best-fit line through the data, which gives a measured sensitivity of $0.25 \frac{\mu V}{W/m^2}$. The theoretical sensitivity for this sensor was calculated to be $0.58 \frac{\mu V}{W/m^2}$.

Several factors could result in this dramatically higher time constant. First, several approximations were made in the computation of the sensor time constant, such as the assumption that the time constant depends on the material parameters for the antenna only. Errors in these approximations would cause differences between the computed and the measured values; however, such a large offset is unlikely to be caused by this type of error.

The most likely cause is that the experimental apparatus has a slower time constant than the sensors. In this case, the exponential profile measured by the sensors would indicate the ramp-up rate of the thermal flux in the stack, not the speed of the sensors. Given that the sensor stack contains significant material, it has a significant thermal mass, causing a slow time constant perhaps on the order of seconds. Therefore, this is the most likely scenario.

To accurately measure the sensor's time constant, an apparatus capable of rapid thermal transients would be required. This apparatus would not only require a thermal flux source capable of rapid changes, but the substrate and all surfaces near the sensor would need to have low thermal mass, to allow it to quickly reach a new equilibrium. Such a setup is beyond the scope of this research. An upper bound on the time constant (19.0 seconds) has been measured, and this figure will be taken to be the actual time constant.

Pressure Sensitivity

The experimental apparatus showed a sensitivity to pressure. Since the layers of the stack shown in Figure 5.23 are not completely in physical contact, the majority of the heat transfer through the stack is accomplished by conduction through the chamber gas. Therefore, as the pressure is decreased, the thermal conductivity through the gas decreases; consequently, the coupling efficiency in the stack is reduced. Below about 1T, the conductivity is too low for the experimental setup to be effectively used. In addition, below this pressure the surface temperature of the heater rises,

and this causes damage to the sensors (see Figure 5.28 for an example).

The sensitivity of a prototype sensor was measured as a function of pressure, and these data are shown in Figure 5.29. The general trend is toward lower sensitivity at lower pressure. While this trend is not predicted by the analysis presented in this chapter, it can be explained by a number of factors:

1. At lower pressure, the uniformity of the setup is compromised. Heat is preferentially transferred through the stack at locations where the heater is in contact with the sensor substrate. This causes a non-uniform thermal flux through the sensor substrate, which could compromise the effectiveness of the structure. The design of the sensor assumes that all heat flows vertically through the structure; any lateral thermal flux could alter the temperature gradient between the membrane structure and the reference resistor.
2. Because the surface temperature of the heater is higher during the low pressure experiments, more of the heat transfer to the sensor is accomplished through radiation. The sensor substrate is smaller than the heater and commercial sensor, so some of the heat goes directly from the heater to the substrate. If the emissivity of the prototype sensor is different from the commercial sensor, it is possible that heat could begin to be preferentially transferred to the commercial sensor, causing a decrease in the measured sensitivity.
3. During the low pressure experiments, the applied thermal flux was kept low, to avoid damage to the sensor. As a result, the accuracy of these measurements is less than the high pressure measurements.

It should be noted that each of these factors is a result of the calibration setup only, and will not affect the accuracy of the sensor when operating inside a plasma. In a plasma, the thermal flux will be applied to the structure in a vertical direction, which will ensure that the sensor works as expected. Also, the heat source will come from the plasma ions and chemistry, and not through conductive transfer; therefore, the problems associated with radiative transfer will not pose a problem.

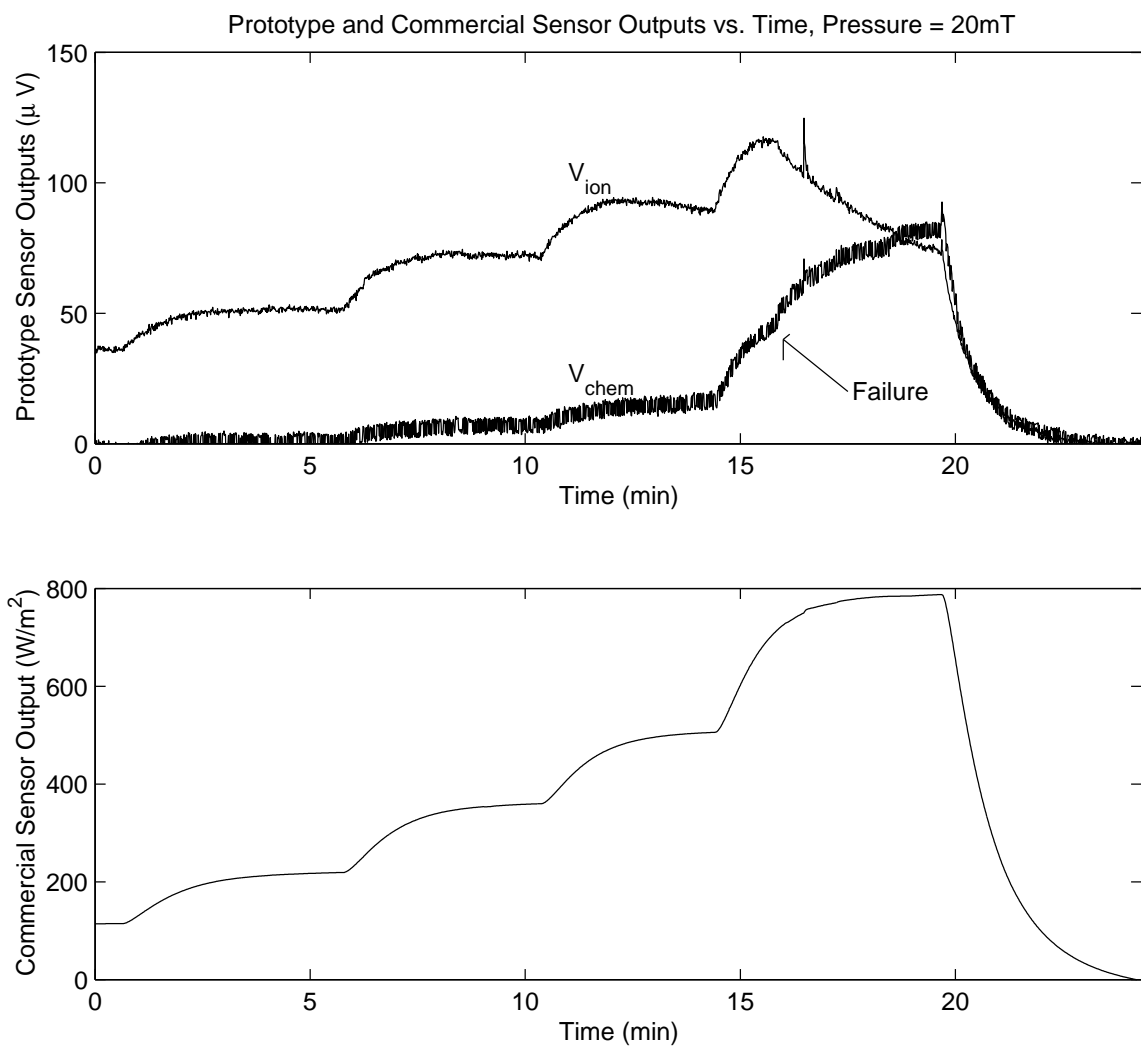


Figure 5.28: Example of sensor failure at low pressure. During this segment of data, the applied thermal flux is gradually increased until a sudden change in the sensor characteristics is observed (denoted by the arrow). After this point, the sensitivity of the sensor is reduced by roughly a factor of two.

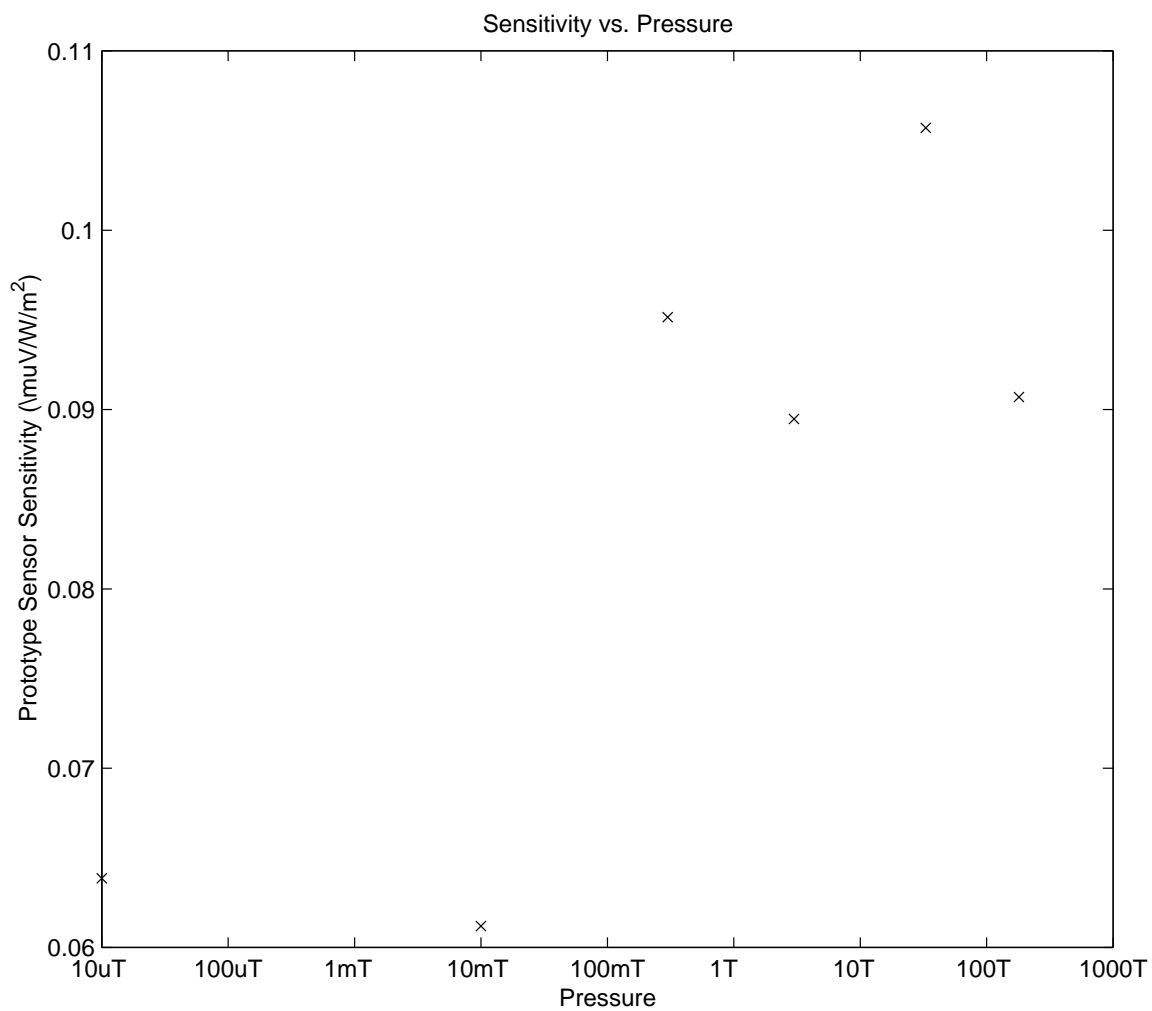


Figure 5.29: Plot of prototype sensor sensitivity vs. pressure. Note that the sensitivity of this sensor is less than that for the sensor plotted in Figure 5.27. Due to the nonuniformity of the XeF_2 etch step, there is a high sensor-to-sensor nonuniformity of sensitivity.

5.12.3 O_2 Plasma Experiment

The prototype sensor was placed into a commercial plasma etch chamber (PlasmaTherm Model PK-12), to test its performance under etching conditions. This tool contains a 12-inch diameter, 6-inch high cylindrical chamber, and a 500W, 13.56 MHz capacitively-coupled power supply. A 6-wire, twisted-pair vacuum feedthrough was constructed to allow electrical access to the prototype sensor inside the chamber. A ferrite block was placed around the wires immediately outside the feedthrough, to reduce RF noise on the lines.

A prototype sensor was placed into the chamber, and the sensor outputs were monitored using the same monitoring system described in Section 5.12.1. An experiment was performed in which the RF power was set to 10W, and various mixtures of N_2 and O_2 were allowed to flow into the chamber. The data from this experiment are shown in Figure 5.30. As can be seen from the figure, the recorded sensor output was on the order of 10 to 30mV, which is many orders of magnitude larger than the expected value. The maximum power density measured should be less than the total power divided by the chuck area, which is $140\frac{W}{m^2}$ for this experiment. Using the sensitivity computed in the previous section ($0.25\frac{\mu V}{W/m^2}$), this is equivalent to a sensor output voltage of $30\mu V$. However, the voltages recorded during the plasma experiment were approximately three orders of magnitude larger than this.

This problem is most likely due to the use of wired connections. The wires connecting the sensor to the feedthrough (which were $\approx 8''$ long) functioned as antennas, collecting the RF power from the power source and overlaying it onto the sensor voltages. Because the sensors generate relatively small signal levels, the signal was completely lost in this noise. Therefore, no information could be gleaned from this experiment.

To counteract this problem, several solutions are possible. First, filtering electronics can be added to the sensor system, to avoid the transmission of RF noise along the wires. This solution requires rather sophisticated electronics to filter this type

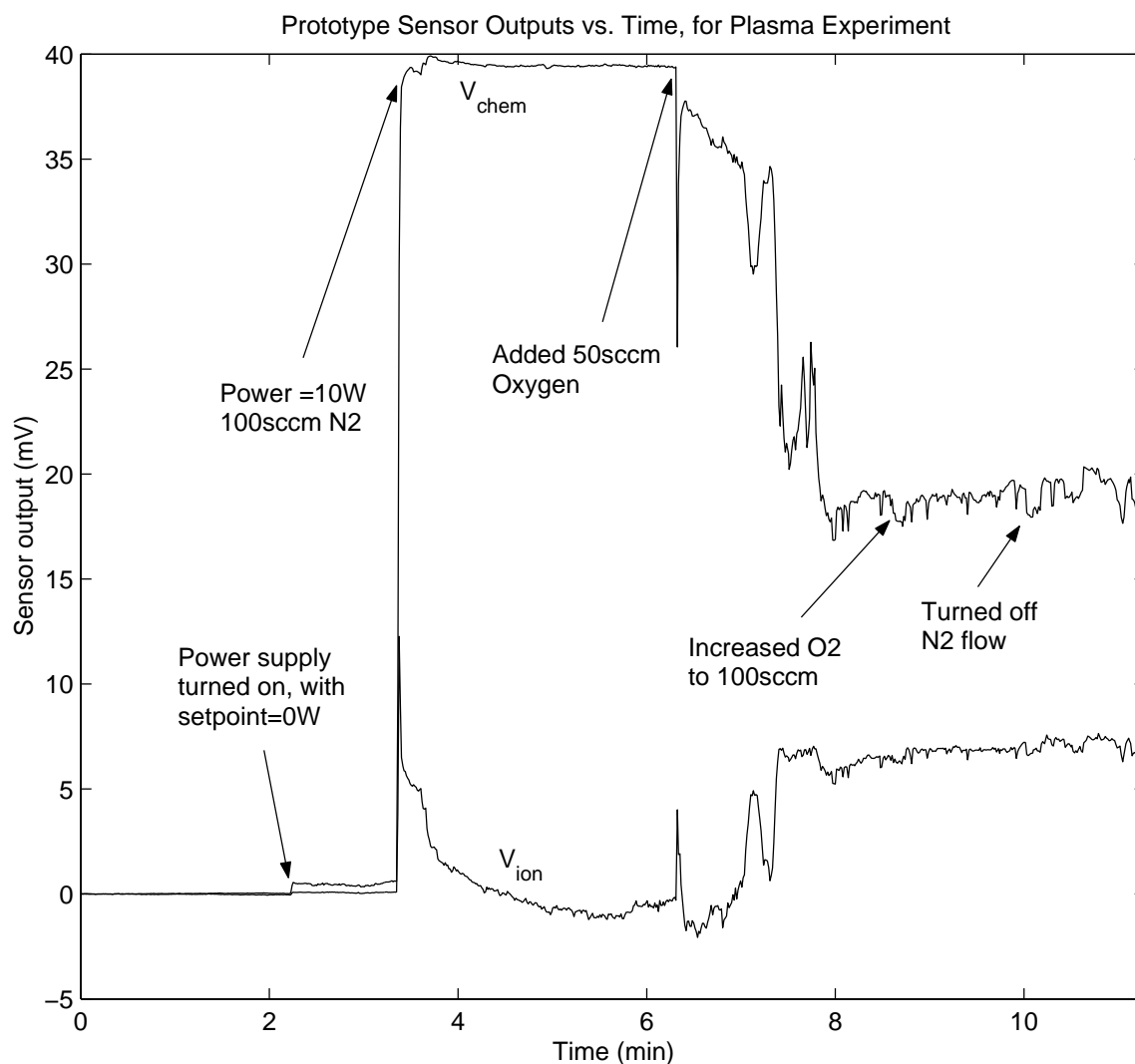


Figure 5.30: Plot of thermal flux sensor output during an experimental run inside an active O_2 plasma. During the experiment, the power setpoint was 10W, and the gas flows were adjusted during the run with various combinations of N_2 and O_2 .

of noise without drawing significant power out of the plasma, thereby perturbing the measured quantities. Another solution is to use wireless electronics and communications, to avoid the need to carry signals out of the chamber using wires. A final solution is to repeatedly turn the plasma on and off, and only take data during the off-periods. Since there is no electrical interference when the plasma is off, the sensors provide valid thermal flux measurements. By observing the decay curve just after the plasma is shut down (see Figure 5.31), the value during plasma exposure can be estimated.

Clearly, the best solution is the use of wireless electronics, because it avoids the hassles associated with the other two methods. However, this method is also the most complicated. All such techniques are outside the scope of this research, and will be left as future work.

5.13 Summary

This chapter describes the design, construction, and testing of a prototype thermal flux sensor, for use in plasma etch processes. A complete theoretical analysis of the proposed sensor is undertaken, with results for sensitivity, time constant, signal to noise ratio, and other performance parameters given. Next, a detailed description of the fabrication process used to construct a prototype thermal flux sensor is presented. Finally, results from bench-top, low-pressure, and in-plasma testing of this sensor are presented. The prototype sensor is shown to have a sensitivity of $0.25 \frac{\mu V}{W/m^2}$, repeatability of $8.3 W/m^2$, and time constant of 19 seconds.

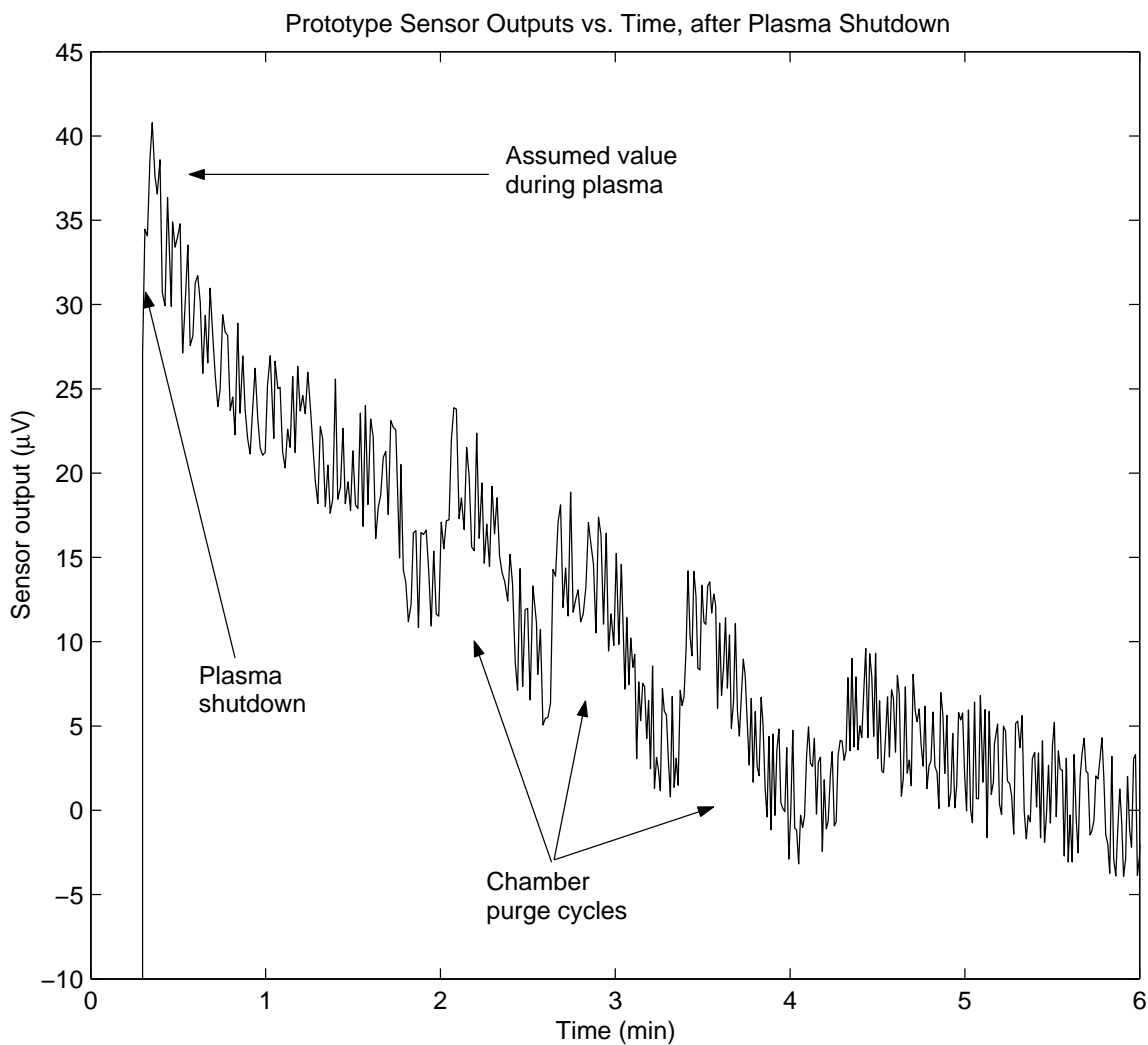


Figure 5.31: Plot showing a method for determination of the plasma thermal flux from the time decay after the shutdown of plasma. The thermal flux measurement returns to normal after plasma is shut down, and the time decay can be used to extrapolate back to find the thermal flux while the plasma was active. Note that the three pump/purge cycles performed by the machine after plasma shutdown can be observed in the data.

Chapter 6

Conclusion

6.1 Dissertation Summary

Many semiconductor process state variables are difficult or impossible to measure using external, in-line metrology. The measurement of these variables is important for many reasons. The availability of high-fidelity process state measurement is critical to the vital functions of equipment design, process optimization, equipment fault diagnosis, and process control.

One method to alleviate this lack of data, discussed in this dissertation, is the application of sensors, electronics, a communication system, and a power source to the surface of a blank silicon wafer. Because this wafer is completely autonomous, and physically resembles a standard wafer, it can be loaded into a process tool by the standard handling robotics. As the wafer is processed, it can measure the variables of interest and transmit them outside the chamber. These data can then be used for any or all of the above-mentioned tasks. Additionally, because the data can be highly spatially resolved, highly temporally resolved, and available in real time, many other applications can be conceived. Real-time control loops can be applied to tune automatically, or pattern matching techniques can be used to efficiently diagnose faults [17].

In this dissertation, two such wafer-mounted sensors were discussed. A polysilicon film thickness sensor design was presented, and results from a prototype design were reported. This sensor is accurate, repeatable, and stable, and includes a temperature compensation system to avoid thermally-generated errors. The other sensor discussed in this dissertation is a thermal flux sensor. Chapter 5 discussed the design, analysis, construction, and testing of this sensor. The thermal flux sensor was successfully tested, yielding a measured sensitivity of $0.25 \frac{\mu V}{W/m^2}$, a repeatability of $8.3 W/m^2$, and a time constant of 19 seconds.

6.2 Future Research Directions

This dissertation has explored the design, fabrication, and testing of two sensors for etch processes. There are clearly many other sensor types that need to be built, and many other semiconductor (and even non-semiconductor) processes that could benefit from wafer-mounted, fully-integrated sensor arrays. For example, in lithographic exposure tools, it would be very beneficial to be able to measure the latent image profile immediately following exposure in order to more accurately control exposure dose. Another example would be an on-wafer endpoint sensor for CMP, which could be used for run-to-run endpoint control. The list of possible sensors for different processes is daunting.

This research has focussed only on the sensor component of the wafer-mounted sensor concept. Further work on wireless communications, onboard power systems, and environmental isolation schemes is necessary to drive this concept to wide-spread industrial use. Since typical wafer handling robotics expect to receive standard-size wafers, these “extra” components must be made as small and light as possible, to avoid collision with system components. This miniaturization concept can be taken to an extreme, as shown in Figure 6.1. This figure shows a silicon wafer that has a hollow cavity at its center. Inside this cavity, a power source, measurement electronics, and

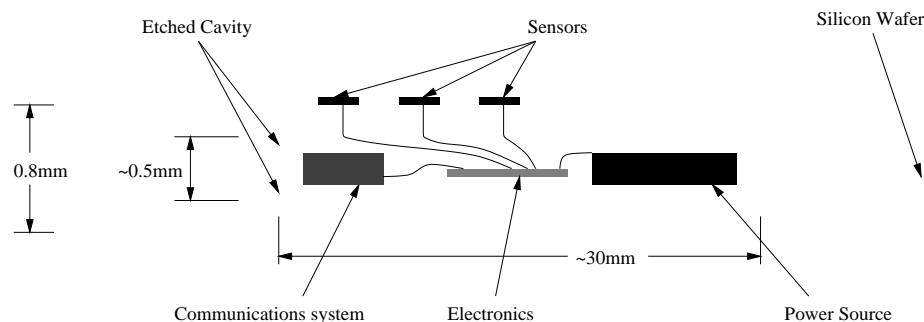


Figure 6.1: “Clam-shell” sensor wafer, with electronics, power supply, and communications system fully encapsulated inside a standard silicon wafer.

a through-the-wafer wireless communication system are located. Wires are passed from the cavity through part of the wafer, to surface-mounted sensors. Because all of the components are located inside the wafer, robotics and process chambers will function exactly as expected.

Another aspect of this research which could warrant future research is new methods for using the type of data provided by a wafer-mounted sensor system. Because current metrology tools do not offer information of this type (spatially-resolved, temporally-resolved, and in real-time), there are many applications that are enabled by this technology. For example, by closing a real-time control loop around the process tool, it might be possible to auto-tune, or auto-diagnose the equipment in much less time than is traditionally necessary for these tasks. More research must be conducted to develop and test these new types of applications.

Bibliography

- [1] Semiconductor Industry Association. *Int. Technology Roadmap for Semiconductors 1999 Edition*. 1999.
- [2] Mason Freed. *In-situ* etch rate sensor arrays for plasma etch processes. Mechanical engineering, University of California, Berkeley, Berkeley, CA, May 1999.
- [3] Mason Freed, Michiel Krüger, Costas Spanos, and Kameshwar Poolla. Real time *in-situ* data acquisition using autonomous on-wafer sensor arrays. *Proc. 9th Int. Symp. on Semicond. Manufact.*, Sep 2000.
- [4] Mason Freed, Michiel Krüger, Costas Spanos, and Kameshwar Poolla. Autonomous, on-wafer sensors for process modeling, diagnosis, and control. *to be published in IEEE Trans. on Semicond. Manufact.*, 2001.
- [5] N. Chong, J. Lim, J. Sakamoto, B. Dunn, M. Krüger, M. Freed, S. Eitapence, K. Poolla, and C. Spanos. Lithium batteries for powering sensor arrays. *Proc. 198th Meeting Electrochem. Soc.*, Oct 2000.
- [6] Darin Fisher, Mason Freed, Costas Spanos, and Kameshwar Poolla. Micro-sensor arrays for calibration, control, and monitoring of semiconductor manufacturing processes. *Proc. IEEE Int. Conf. on Control Applications*, pages 784–788, Aug 1999.
- [7] Darin Fisher, Mason Freed, Costas Spanos, and Kameshwar Poolla. Autonomous

- micro-sensor arrays for process control of semiconductor manufacturing processes. *Proc. 38th Conf. on Decision and Control*, pages 4179–4184, Dec 1999.
- [8] O. Solgaard, F.S.A. Sandejas, and D.M. Bloom. A deformable grating optical modulator. *Optics Lett.*, 17(9):688–690, May 1992.
- [9] SensArray Corporation. <http://www.sensarray.com>.
- [10] Private communication with David Steele at Advanced Micro Devices.
- [11] Omega Engineering, Inc. <http://www.omega.com>.
- [12] Michael A. Lieberman and Allan J. Lichtenberg. *Principles of Plasma Discharges and Materials Processing*. John Wiley and Sons, Inc., 1994.
- [13] James D. Plummer, Michael D. Deal, and Peter B. Griffin. *Silicon VLSI Technology: Fundamentals, Practice and Modeling*, chapter 10. Prentice Hall Electronics and VLSI Series, 2000.
- [14] Michael A. Lieberman and Allan J. Lichtenberg. *Principles of Plasma Discharges and Materials Processing*, chapter 1. John Wiley and Sons, Inc., 1994.
- [15] Michael A. Lieberman and Allan J. Lichtenberg. *Principles of Plasma Discharges and Materials Processing*, chapter 15. John Wiley and Sons, Inc., 1994.
- [16] Stanley Wolf and Richard N. Tauber. *Silicon Processing for the VLSI Era*, volume 1, page 546. Lattice Press, Sunset Beach, California, 1986.
- [17] Anna Maria Ison. *Probabilistic Modeling for Fault Classification of Plasma Equipment*. Electrical engineering, University of California at Berkeley, Berkeley, CA, 1999.
- [18] Gary S. May and Costas J. Spanos. Automated malfunction diagnosis of semiconductor fabrication equipment: A plasma etch application. *IEEE Trans. on Semicond. Manufact.*, 6(1):28–40, Feb 1993.

- [19] S. Dolins, A. Srivastava, and B. Flinchbaugh. Monitoring and diagnosis of plasma etch processes. *IEEE Trans. on Semicond. Manufact.*, 1(1), Feb 1988.
- [20] Costas J. Spanos and Gary S. May. Using regression equations for model-based diagnosis in the berkeley computer-aided manufacturing system. In *Wkshop. on Intel. Diag. Cntrl. Sys. for Manufac.*, July 1990.
- [21] H.M. Anderson. Plasma diagnostics for semiconductor processing. *2000 Digest LEOS Summer Topical Meetings*, pages II17–18, Jul 2000.
- [22] Joel O. Stevenson, Pamela P. Ward, Michael L. Smith, and Richard J. Markle. A plasma process monitor/control system. *Surface and Interface Analysis*, 26:124–133, 1998.
- [23] D. Tretheway and E.S. Aydil. Modeling of heat transport and wafer heating effects during plasma etching. *J. Electrochem. Soc.*, 143:3674, 1996.
- [24] Eray S. Aydil and Demetre J. Economou. Modeling of plasma etching reactors including wafer heating effects. *J. Electrochem. Soc.*, 140(5):1471–1481, May 1993.
- [25] Semiconductor Industry Association. *National Technology Roadmap for Semiconductors 1997 Edition*. 1997.
- [26] M.D. Baker, F.R. Williams, and G.S. May. A novel in-situ monitoring technique for reactive ion etching using a surface micromachined sensor. *IEEE Trans. on Semicond. Manufact.*, 11(2):254–265, May 1998.
- [27] T. Dalton, W. Conner, and H. Sawin. Interferometric real-time measurement of uniformity for plasma etching. *J. Electrochem. Soc.*, 141:1893, 1994.
- [28] Ka Shun Wong and Duane S. Boning. On *in-situ* etch rate extraction from interferometric signals. In *Electrochem. Soc. Proc.*, volume 95-4, pages 360–371. Electrochem. Soc., 1995.

- [29] David A. White, Duane Boning, Stephanie W. Butler, and Gabriel G. Barna. Spatial characterization of wafer state using principal component analysis of optical emission spectra in plasma etch. *IEEE Trans. on Semicond. Manufact.*, 10(1):52–60, Feb 1997.
- [30] D. White. *in-situ* wafer uniformity estimation using principal component analysis methods. Electrical engineering and computer science, Massachusetts Institute of Technology, Cambridge, MA, May 1995.
- [31] E. Chevalier and P. Maquin. Innovative integrated plasma tool for process and exhaust monitoring. *Proc. SPIE*, 3884:88–95, Sep 1999.
- [32] A.I. Chowdhury, T.M. Klein, and G.N. Parsons. *In-situ* real-time mass spectroscopic sensing and mass balance modeling of selective area silicon pecvd monitoring. *AIP Conf. Proc.*, (449):363–367, Mar 1998.
- [33] Trey Roessig. *Integrated MEMS Tuning Fork Oscillators for Sensor Applications*. Mechanical engineering, University of California at Berkeley, Berkeley, CA, May 1998.
- [34] Gregory T.A. Kovacs. *Micromachined Transducers Sourcebook*, pages 310–312. WCB McGraw-Hill, 1998.
- [35] Moshe Sarfaty, Chris Baum, Michael Harper, Noah Hershkowitz, and J. Leon Shohet. Real-time determination of plasma etch-rate selectivity. *Plasma Sources Sci. Technol.*, 7:581–589, 1998.
- [36] Nanometrics, Inc. <http://www.nanometrics.com>.
- [37] Dieter K. Schroder. *Semiconductor Material and Device Characterization*, pages 1–13. Wiley Interscience, 1990.
- [38] L.J. van der Pauw. A method of measuring specific resistivity and hall effect of discs of arbitrary shape. *Philips Res. Rep.*, 13:1–9, 1958.

- [39] Michael W. Cresswell, Nadine M.P. Guillaume, William E. Lee, Richard A. Allen, William F. Guthrie, Rathindra N. Ghosttagore, Zoe E. Esborne, Neal Sullivan, and Loren W. Linholm. Extraction of sheet resistance from four-terminal sheet resistors replicated in monocrystalline films with nonplanar geometries. *IEEE Trans. on Semicond. Manufact.*, 12(2):154–165, 1999.
- [40] Patrick Troccoli, Lynda Mantalas, Richard Allen, and Loren Linholm. Extending electrical measurements to the $0.5\mu\text{m}$ regime. *Proc. SPIE*, 1464:90–103, 1991.
- [41] Jacob Millman and Christos C. Halkias. *Integrated Electronics*, pages 1–18. McGraw-Hill Kogakusha, Ltd., Tokyo, 1972.
- [42] J.A. Meyer, K.H.R. Kirmse, J.S. Jenq, S.Y. Perez-Montero, H.L. Maynard, A.E. Wendt, J.W. Taylor, and N. Hershkowitz. Experiments with back side gas cooling using an electrostatic wafer holder in an electron cyclotron resonance etching tool. *Appl. Phys. Lett.*, 64(15):1926–1928, Apr 1994.
- [43] J. Ding, J.S. Jenq, G.H. Kim, H.L. Maynard, J.S. Hamers, N. Hershkowitz, and J.W. Taylor. Etching rate characterization of SiO_2 and si using ion energy flux and atomic fluorine density in a $\text{cf}_4/\text{o}_2/\text{ar}$ electron cyclotron resonance plasma. *J. Vac. Sci. Technol. A*, 11(4):1283–1288, Jul 1993.
- [44] Joseph C. Martz, Dennis W. Hess, and Eugene E. Petersen. A generalized model of heat effects in surface reactions. i. model development. *J. Appl. Phys.*, 72(8):3282–3288, Oct 1992.
- [45] Joseph C. Martz, Dennis W. Hess, and Eugene E. Petersen. A generalized model of heat effects in surface reactions. ii. application to plasma etching reactions. *J. Appl. Phys.*, 72(8):3289–3293, Oct 1992.
- [46] A. Durandet, O. Joubert, J. Pelletier, and M. Pichot. Effects of ion bombardment

- and chemical reaction on wafer temperature during plasma etching. *J. Appl. Phys.*, 67(8):3862–3866, Apr 1989.
- [47] S.J. Pearton, A.B. Emerson, U.K. Chakrabarti, E. Lane, K.S. Jones, K.T. Short, Alice E. White, and T.R. Fullowan. Temperature dependence of reactive ion etching of gaas with $\text{ccl}_2\text{f}_2:\text{o}_2$. *J. Appl. Phys.*, 66(8):3839–3849, Oct 1989.
- [48] Lee M. Loewenstein. Temperature dependence of silicon nitride etching by atomic flourine. *J. Appl. Phys.*, 65(1):386–387, Jan 1989.
- [49] J.C. Martz, D.W. Hess, and W.E. Anderson. Tantalum etching in fluorocarbon/oxygen rf glow discharges. *J. Appl. Phys.*, 67(8):3609–3617, Apr 1990.
- [50] Robert Gardon. An instrument for the direct measurement of intense thremal radiation. *Rev. Sci. Instr.*, 24(5):366–370, May 1953.
- [51] J.S. Kraabel, J.W. Braughn, and A.A. McKillop. An instrument for the measurement of heat flux from a surface with uniform temperature. *Trans. ASME*, 102:576–578, Aug 1980.
- [52] Jaechul Chun, S. Hwan Oh, Seung S. Lee, and Moohwan Kim. Design and fabrication of micro heat flux sensor. In *Proc. 1999 IEEE Int. Conf. on Intelligent Robots and Systems*, pages 1045–1048, 1999.
- [53] Friedemann Völklein and Ernst Kessler. Thermoelectric microsensor for heat flux measurement. In *17th Int. Conf. on Thermoelectrics*, pages 214–217, May 1998.
- [54] E. Piccini, S.M. Guo, and T.V. Jones. The development of a new direct-heat-flux gauge for heat-transfer facilities. *Meas. Sci. and Technol.*, 11:342–349, 2000.
- [55] W.N. MacPherson, J.M. Kilpatrick, J.S. Barton, J.D.C. Jones, L. Zhang, and I. Bennion. Heat flux measurement using fibre-bragg-grating fabry-perot sensors. *Meas. Sci. and Technol.*, 10, 1999.

- [56] L.W. Langley, A. Barnes, G. Matijasevic, and P. Gandhi. High-sensitivity, surface-attached heat flux sensors. *Microelec. Journ.*, 30:1163–1168, 1999.
- [57] A.H. Epstein, G.R. Guenette, R.J.G. Norton, and Cao Yuzhang. High-frequency response heat-flux gauge. *Rev. Sci. Instr.*, 57(4):639–649, Apr 1986.
- [58] Masanori Hayashi, Akira Sakurai, and Shigeru Aso. A study of multi-layered thin film heat transfer gauge and a new method of measuring heat transfer rate with it. In *15th Fluid Dynamics Conf.*, pages 91–101, Oct 27 1983.
- [59] Wolf D. Bauer and John B. Heywood. Transfer function of thin-film heat flux sensor. *Exp. Heat Trans.*, 10:181–190, 1997.
- [60] N. Martins, M.G. Carvelho, N.H. Afgan, and A.I. Leontiev. A new instrument for radiation heat flux measurement - analysis and parameter selection. *Heat Recovery Systems and CHP*, 15(8):787–796, 1995.
- [61] Loren P. Johnson and Thomas E. Diller. Measurements with a heat flux microsensor deposited on a transonic turbine blade. *IEEE*, 37(1), 1995.
- [62] J.C. Ingraham and G. Miller. Infrared calorimeter for time-resolved plasma energy flux measurement. *Rev. Sci. Instr.*, 54(6):673–676, Jun 1983.
- [63] F. Volklein, M. Blumers, and L. Schmitt. Thermoelectric microsensors and microactuators (mems) fabricated by thin film technology and micromachining. In *18th Int. Conf. Thermoelectrics*, pages 285–293, 1999.
- [64] Vital M. Meyer, Niklaus Schneeberger, and Bruno Keller. Epoxy-protected thermopile as high sensitive heat flux sensor. In *Transducers '97*, pages 1267–1270, Jun 1997.
- [65] J.G. Korvink, R. Lenggenhager, J. Funk, G. Wachutka, and H. Baltes. Computer-aided trade-off study of an integrated infrared sensor. *IEEE*, pages 173–176, 1994.

- [66] R. Lenggenhager, D. Jaeggi, P. Malcovati, H. Duran, H. Baltes, and E. Doering. Cmos membrane infrared sensors and improved tmahw etchant. *IEEE*, pages 531–534, 1994.
- [67] Mehran Mehregany. Mems for smart structures. *SPIE*, 2448:105–114, 1995.
- [68] D.G. Holmberg and T.E. Diller. High-frequency heat flux sensor calibration and modeling. *J. Fluids Engin.*, 117:659–664, Dec 1995.
- [69] Vital M. Meyer and Bruno Keller. A new heat flux sensor: From microvolts to millivolts. *Sensors and Materials*, 8(6):345–356, 1996.
- [70] Christopher S.K. Cho, Gustave C. Fralick, and Hemanshu D. Bhatt. An experimental study of a radially arranged thin-film heat-flux gauge. *Meas. Sci Technol.*, 8:721–727, 1997.
- [71] Jih-Fen Lei, Herbert A. Will, and Lisa C. Martin. Microfabricated thin-film physical sensors for hostile environments. *IEEE*, pages 13–1–13–7, 1998.
- [72] R. Wendt, K. Ellmer, and K. Wiesemann. Thermal power at a substrate during zn:al thin film deposition in a planar magnetron sputtering system. *J. Appl. Phys.*, 82(5):2115–2122, Sep 1997.
- [73] M.F. Faudon, K.A. Thole, R.L. Engelstad, D.J. Resnick, K.D. Cummings, and W.J. Dauksher. Thermal analysis of an x-ray mask membrane in a plasma environment. *J. Vac. Sci. Technol. B*, 13(6):3050–3054, Nov 1995.
- [74] Kenneth HG. Kreider and Frank DiMeo. Platinum/palladium thin-film thermocouples for temperature measurements on silicon wafers. *Sens. Act. A*, 69:46–52, 1998.
- [75] K. Ellmer and R. Mientus. Calorimetric measurements with a heat flux transducer of the total power influx onto a substrate during magnetron sputtering. *Surf. Coatings and Technol.*, pages 1102–1106, 1999.

- [76] Gregory T.A. Kovacs. *Micromachined Transducers Sourcebook*, pages 560–564. WCB McGraw-Hill, 1998.
- [77] Efundu. http://www.efunda.com/designstandards/sensors/methods/wheatstone_bridge.cfm.
- [78] Frank P. Incropera and David P. DeWitt. *Fundamentals of Heat and Mass Transfer*, pages 2–12. John Wiley and Sons, New York, 1996.
- [79] Frank P. Incropera and David P. DeWitt. *Fundamentals of Heat and Mass Transfer*, pages 48–49,315,346–360,827–853. John Wiley and Sons, New York, 1996.
- [80] Stanley Wolf and Richard N. Tauber. *Silicon Processing for the VLSI Era*, volume 1, pages 75–76. Lattice Press, Sunset Beach, California, 1986.
- [81] Paul R. Gray and Robert G. Meyer. *Analysis and Design of Analog Integrated Circuits*, pages 719–722. John Wiley & Sons, Inc., 3 edition, 1993.
- [82] Stephen D. Senturia. *Microsystem Design*, pages 220–222. Kluwer Academic Press, 2000.
- [83] Arthur P. Boresi, Omar M. Sidebottom, Fred B. Seely, and James O. Smith. *Advanced Mechanics of Materials*, pages 441–443. John Wiley and Sons, Inc., 3 edition, 1978.
- [84] Inc. The Mathworks. <http://www.mathworks.com/>.
- [85] Patrick B. Chu, Jeffrey T. Chen, Richard Yeh, Gisela Lin, Jeff C.P. Huang, Brett A. Warneke, and Kristofer S.J. Pister. Controlled pulse-etching with xenon difluoride. In *Transducers '97*, June 1997.

- [86] M.H. Hecht, R.P.Vasquez, F.J. Grunthaner, N. Zamani, and J. Maserjian. A novel x-ray photoelectron spectroscopy study of the al/ SiO_2 interface. *J. Appl. Phys.*, 57:5256–5261, June 1985.
- [87] Kirt R. Williams. Etch rates for micromachining and ic processing v4.4. <http://www-bsac.EECS.Berkeley.EDU/db/etch.pdf>, July 29 1996.
- [88] L.B. Valdes. Resistivity measurements on germanium for transistors. In *Proc. I.R.E.*, volume 42, pages 420–427. I.R.E., Feb 1954.

Appendix A

Four Point Probe Analysis

The four-point probe technique can be used to measure sheet resistance (resistivity divided by thickness) of a thin sheet of material. This method involves placing four small probes on a planar sample of material in a straight line. In the ideal case, the sample must be an infinite plane. See Figure A.1 for a schematic of this arrangement. However, corrections can be made to the ideal case to allow for finite geometries.

To find a relation between the voltage measured and the current sourced, we first find the voltage at a point p , which is located at a distance r from a point current source (sourcing current I), in a very thin sheet of material. It is assumed that the material is much thinner than the probe spacing, so that no current flows in the vertical direction within the material. Because it is assumed that the current flows

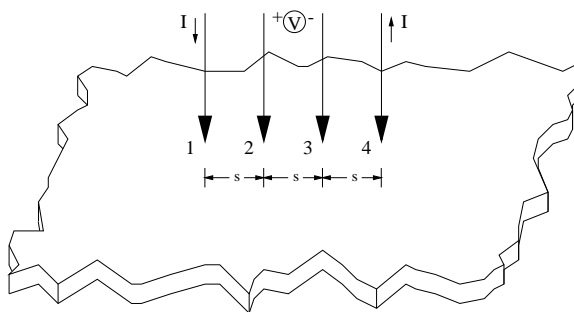


Figure A.1: Infinite sheet with linear four-probe arrangement

outward uniformly into the material, the current density can be found by dividing the total current by the area of a cylindrical surface centered about the source,

$$J = \frac{I}{(2\pi r)t} \quad (\text{A.1})$$

where J is the current density, t is the thickness of the sheet, and r is the distance from the current source. Now, voltage and current density are related by $-\nabla V = E = \rho J$, or in this one-dimensional case $-\frac{d}{dr}V = \rho J$, where ρ is the resistivity of the material. Solving this equation with J defined as in Equation A.1 above yields,

$$V = -\frac{\rho I}{2\pi t} \ln(r) \quad (\text{A.2})$$

Applying this equation to the four-point probe situation, where there are both a current source (probe #1) *and* a current sink (probe #4), the voltages at the inner probes (probes #2 and #3) are,

$$V_2 = -\frac{\rho I}{2\pi t} \ln(s) - \frac{\rho(-I)}{2\pi t} \ln(2s) \quad (\text{A.3})$$

$$V_3 = -\frac{\rho I}{2\pi t} \ln(2s) - \frac{\rho(-I)}{2\pi t} \ln(s) \quad (\text{A.4})$$

Now, to find the voltage difference measured across probes #2 and #3, the two voltages are subtracted,

$$\begin{aligned} V_{diff} &= \left(-\frac{\rho I}{2\pi t} \ln(s) - \frac{\rho(-I)}{2\pi t} \ln(2s) \right) - \left(-\frac{\rho I}{2\pi t} \ln(2s) - \frac{\rho(-I)}{2\pi t} \ln(s) \right) \\ &= \frac{\rho I}{2\pi t} (2 \ln(2s) - 2 \ln(s)) \\ &= \frac{\rho I}{\pi t} \ln 2 \end{aligned} \quad (\text{A.5})$$

Finally, solving this equation for $\frac{\rho}{t}$, the sheet-resistance, yields,

$$\rho_s \equiv \frac{\rho}{t} = \frac{\pi}{\ln 2} \frac{V}{I} \quad (\text{A.6})$$

This result only applies to the ideal infinite plane case. However, a correction factor F can be added to Equation A.6 which corrects the equation for non-infinite geometry to get [88],

$$\rho_s = F \frac{\pi}{\ln 2} \frac{V}{I} \quad (\text{A.7})$$

The dimensionless parameter F is a function of geometrical factors including sample size and probe placement relative to sample edges, and can be calculated using a number of methods [37]. However, if the lateral diameter of the sample is much larger (at least a factor of 10) than the probe spacing, and if the probe spacing is much larger than the sample thickness, then F is very close to unity, and no correction is necessary [88].

Appendix B

Film Thickness Sensor Process

The final film-thickness sensor (seen in Figure 4.7) was fabricated using the process shown below. This process flow allows the fabrication of polysilicon film-thickness sensors, buried polysilicon temperature compensation sensors, complex aluminum interconnections, wire over-cross structures, and solderable nickel bond pads.

Film Thickness Sensor Process v3.5

1. Start with $\langle 100 \rangle$ test-grade wafers
2. Grow 3000Å wet oxide
 - a. Pirahna clean 10 min
 - b. 10:1 BHF dip 10 sec
 - c. Grow oxide, 1050 °C, 25m, steam
3. Deposit 8000Å n+ doped polysilicon (sheet resistance $\approx 20 \frac{\text{ohm}}{\text{sq}}$)
 - a. Pirahna clean 10 min
 - b. 10:1 BHF dip 10 sec
 - c. Deposit poly, 610 °C, 5h 30m, LPCVD SiH_4
4. Anneal poly, 900 °C, 30m, N_2
5. Measure poly thickness and sheet resistance
6. Pattern with POLY mask
 - a. 30m dehydration bake / HMDS coat
 - b. Spin 1.3 μm G-line resist, 5000rpm, 30s
 - c. Soft bake, 90 °C, 60s
 - d. Expose wafers using contact lithography

- e. Develop resist
- f. Hard bake, 120°C , 30m
7. Wet polysilicon etch in $64\% \text{HNO}_3 / 33\% \text{H}_2\text{O} / 3\% \text{NH}_4\text{F}$
8. Strip resist
9. Deposit 8000\AA of Al-2%Si via RF magnetron sputtering, 4.5kW, 6mT
10. Pattern with METAL1 mask
 - a. 30m dehydration bake / HMDS coat
 - b. Spin $1.3\mu\text{m}$ G-line resist, 5000rpm, 30s
 - c. Soft bake, 90°C , 60s
 - d. Expose wafers using contact lithography
 - e. Develop resist
 - f. Hard bake, 120°C , 30m
11. Wet aluminum etch in $80\% \text{H}_3\text{PO}_4 / 10\% \text{H}_2\text{O} / 5\% \text{CH}_3\text{COOH} / 5\% \text{HNO}_3$
12. Strip resist
13. Apply 10000\AA spin-on-glass
 - a. Perform 30m dehydration bake at 120°C
 - b. Spin Futurex IC1-200 SiO₂ SOG, 3000 rpm, 20s
 - c. Perform solvent evaporation, 120°C , 30m
 - d. Complete solvent evaporation, 200°C , 30m
14. Anneal SOG, 400°C , 30m, N_2
15. Pattern with VIA mask
 - a. 30m dehydration bake / HMDS coat
 - b. Spin $1.3\mu\text{m}$ G-line resist, 5000rpm, 30s
 - c. Soft bake, 90°C , 60s
 - d. Expose wafers using contact lithography
 - e. Develop resist
 - f. Hard bake, 120°C , 30m
16. Plasma etch SOG using $\text{CHF}_3 / \text{CF}_4 / \text{He}$ chemistry
17. Strip resist
18. Deposit 8000\AA of Al-2%Si via RF magnetron sputtering, 4.5kW, 6mT
19. Sinter aluminum, 400°C , 30m, N_2
20. Deposit 3000\AA of Ni via RF magnetron sputtering, 1.5kW, 4mT
21. Pattern with METAL2 mask
 - a. 30m dehydration bake / HMDS coat
 - b. Spin $1.3\mu\text{m}$ G-line resist, 5000rpm, 30s
 - c. Soft bake, 90°C , 60s
 - d. Expose wafers using contact lithography
 - e. Develop resist
 - f. Hard bake, 120°C , 30m
22. Wet nickel etch in $50\% \text{HF} / 50\% \text{HNO}_3$
23. Wet aluminum etch in $80\% \text{H}_3\text{PO}_4 / 10\% \text{H}_2\text{O} / 5\% \text{CH}_3\text{COOH} / 5\% \text{HNO}_3$
24. Strip resist

Appendix C

Thermal Flux Sensor Process

The final thermal flux sensor (seen in Figures 5.17 and 5.18) was fabricated using the process shown below. This process flow allows the fabrication of “bare” thermal flux sensors, “coated” thermal flux sensors, surface temperature sensors, aluminum interconnections, and doped polysilicon wire over-cross structures.

Thermal Flux Sensor Process v2.1

1. Start with $\langle 100 \rangle$ test-grade wafers
2. Deposit $0.5\mu\text{m}$ low-stress nitride via LPCVD
 - a. Pirahna clean 10m
 - b. 10:1 BHF dip 10s
 - c. Deposit nitride, 100sccm SiCl_2H_2 , 25sccm NH_3 , 835°C , 140mT, 1h 55m
 - d. Measure nitride thickness, inspect for particles
3. Pattern with NITRIDE mask
 - a. 30m dehydration bake / HMDS coat
 - b. Spin $1.3\mu\text{m}$ G-line resist, 5000rpm, 30s
 - c. Soft bake, 90°C , 60s
 - d. Expose wafers using contact lithography
 - e. Develop resist
 - f. Hard bake, 120°C , 30m
4. Plasma etch nitride using SF_6/He chemistry
5. Strip resist
6. Deposit $1.5\mu\text{m}$ phosphorus-doped polysilicon via LPCVD

- a. Include 1000Å oxide test wafer
 - b. Pirahna clean 10m
 - c. 5:1 BHF dip 10s
 - d. Deposit polysilicon, SiH_4 , PH_3 , 610 °C, 3h 30m
 - e. Measure polysilicon thickness, sheet resistance, inspect for particles
7. Pattern with POLY mask
 - a. 30m dehydration bake / HMDS coat
 - b. Spin 1.3µm G-line resist, 5000rpm, 30s
 - c. Soft bake, 90 °C, 60s
 - d. Expose wafers using contact lithography
 - e. Develop resist
 - f. Hard bake, 120 °C, 30m
 8. Plasma etch poly using HBr chemistry
 9. Strip resist
 10. Grow 1000Å wet thermal oxide
 - a. Include blank test wafer
 - b. Include previous poly control wafer for later sheet resistance measurement
 - c. Pirahna clean 10m
 - d. 10:1 BHF dip 10s
 - e. Grow oxide, 1000 °C, 10m, steam
 - f. Measure oxide thickness on blank wafer, inspect film for particles
 11. Perform pre-deposition of undoped poly (to condition furnace tube walls)
 - a. Deposit poly, 605 °C, 100sccm SiH_4 , 300mT, 30m, empty furnace
 12. Deposit 1.2µm undoped polysilicon
 - a. Include 1000Å oxide control wafer
 - b. Deposit poly, 605 °C, 100sccm SiH_4 , 300mT, 2h 30m
 - c. Measure poly thickness, inspect film for particles
 13. Pattern with STRUCTURE mask
 - a. 30m dehydration bake / HMDS coat
 - b. Spin 1.3µm G-line resist, 5000rpm, 30s
 - c. Soft bake, 90 °C, 60s
 - d. Expose wafers using contact lithography
 - e. Develop resist
 - f. Hard bake, 120 °C, 30m
 14. Wet etch polysilicon in 64% HNO_3 /33% H_2O /3% NH_4F
 - a. Agitate once per minute
 - b. Goal: $\approx 3 - 4\mu m$ lateral overetch
 15. Strip resist
 16. Grow 1000Å wet thermal oxide

- a. Include blank test wafer
 - b. Pirahna clean 10m
 - c. 10:1 BHF dip 10s
 - d. Grow oxide, 1000 °C, 10m, steam
 - e. Measure oxide thickness on blank wafer, inspect film for particles
17. Pattern with STRUCTURE mask
- a. 30m dehydration bake / HMDS coat
 - b. Spin 1.3 μm G-line resist, 5000rpm, 30s
 - c. Soft bake, 90 °C, 60s
 - d. Expose wafers using contact lithography
 - e. Develop resist
 - f. Hard bake, 120 °C, 30m
18. Wet etch oxide in 5:1 BHF
19. Strip resist
20. Re-measure polysilicon sheet resistance
21. Deposit 0.8 μm aluminum/2% silicon via RF magnetron sputtering
- a. Include blank 1000Å oxide test wafer
 - b. Pirahna clean 10m
 - c. Sputter Al/2
 - d. Inspect for particles
 - e. Measure aluminum sheet resistance on blank wafer
22. Pattern with METAL mask
- a. 30m dehydration bake / HMDS coat
 - b. Spin 1.3 μm G-line resist, 5000rpm, 30s
 - c. Soft bake, 90 °C, 60s
 - d. Expose wafers using contact lithography
 - e. Develop resist
 - f. Hard bake, 120 °C, 30m
23. Wet etch aluminum in 80% H_3PO_4 /10% H_2O /5% CH_3COOH /5% HNO_3
24. Inspect again for particles
25. Strip resist
26. Sinter aluminum, 400 °C, N_2 , 20m
27. Measure aluminum sheet resistance using test structures
28. Measure polysilicon sheet resistance using test structures
29. Measure aluminum-polysilicon contact resistance using test structures
30. Pattern with ETCH mask
- a. 30m dehydration bake / HMDS coat
 - b. Spin 2.0 μm G-line resist, 2200rpm, 30s
 - c. Soft bake, 90 °C, 60s
 - d. Expose wafers using contact lithography

- e. Develop resist
 - f. Hard bake, $120\text{ }^{\circ}\text{C}$, 1h
31. Dice wafer, stepping distances: $x=15.08\text{mm}$, $y=20.000\text{mm}$
 32. Release structures
 - a. Etch in XeF_2 etchant, 45 cycles, 14s per cycle, 3.5T XeF_2 , no N_2 , $40\text{ }^{\circ}\text{C}$

Appendix D

Matlab Code

D.1 Matlab program: `sim_structure.m`

```
function paramsout=sim_structure(D,a,b,Vdd,w,h,Rspoly,alpha,...
    top_matl,membr_matl,deltaf,T,lambda,qapplied)
%function params=sim_structure(D,a,b,Vdd,w,h,Rspoly,alpha,...
    top_matl,membr_matl,deltaf,T,lambda,qapplied)
%
% D - diameter of membrane in m
% a - diameter of antenna in m
% b - diameter of post in m
% Vdd - supply voltage in V
% w - thickness of membrane in m
% h - thickness of antenna in m
% Rspoly - sheet resistance of polysilicon in Ohm/sq
% alpha - thermal coefficient of resistance of polysilicon in /C
% top_matl - antenna material
% membr_matl - membrane material
% deltaf - noise bandwidth in Hz
% T - operating temperature in K
% lambda - minimum feature size in m
% qapplied - applied heat flux in W/m^2
%
% params.sensitivity - sensitivity (chemical) in uV/W/m^2
% params.sion        - sensitivity (ion flux) in uV/W/m^2
% params.responsivity - responsivity (chemical) in V/W
% params.Rinner      - inner thermistor resistance in ohms
```

```

% params.qelec      - heat flux expended during measurement in W/m^2
% params.qequiv    - equivalent measurement heat flux in W/m^2
% params.tau       - time constant in s
% params.Vrms      - RMS noise voltage in V
% params.qrms      - RMS equivalent heat flux noise
% params.vmax      - maximum "droop" of antenna and membrane in um
% params.deltaTant - temperature drop across antenna in K
% params.deltaTmemb - temperature drop across membrane in K

if nargin<14
    help sim_structure
    return
end;

[km,cm,rhom,Em,num]=getprops(top_matl);
[ki,ci,rhoi,Ei,nui]=getprops(membr_matl);

% Assume eta = 0
eta=0;
kb=1.381e-23; % J/K

params.sensitivity=(1+eta)*Vdd*alpha*a*a*log(D/b)/16/ki/w;
params.sion=2*params.sensitivity;
params.responsivity=params.sensitivity*2/pi/a/a;
params.Rinner=pi*b*b*Rspoly/8/lambda/lambda;
params.qelec=8*lambda*lambda*Vdd*Vdd/pi/pi/b/b/b/b/Rspoly;
params.qequiv=8*lambda*lambda*Vdd*Vdd/pi/pi/a/a/b/b/Rspoly;
params.tau=cm*rhom*a*a*log(D/b)/8/ki + ci*rhoi*D*D/4/ki;
params.Vrms=b/lambda*sqrt(2*pi*deltaf*kb*T*Rspoly);
params.qrms=params.Vrms/params.sensitivity;
params.vmax=3*rhom*9.8*a*a/16*( (1-num*num)*a*a/Em/h/h +...
    (1-nui*nui)*D*D/Ei/w/w );
params.deltaTant=(a*a-b*b)*qapplied/16/h/km;
params.deltaTmemb=a*a*qapplied*log(D/b)/8/ki/w;

% Convert units:
params.sensitivity=params.sensitivity*1e6; % convert V to uV
params.sion=params.sion*1e6;             % convert V to uV
params.vmax=params.vmax*1e6;            % convert m to um

```

```

if nargout<1
    fprintf('Results for membrane=%s, antenna=%s\n',membr_matl,...
        top_matl);
    fprintf('-----\n');
    fprintf('Membrane diameter (D): %0.2f um\n',D*1e6);
    fprintf('Antenna diameter (a): %0.2f um\n',a*1e6);
    fprintf('Antenna post diameter (b): %0.2f um\n',b*1e6);
    fprintf('Supply voltage (Vdd): %0.2f V\n',Vdd);
    fprintf('\n');
    fprintf('Sensitivity: %0.2f uV/W/m^2\n',params.sensitivity);
    fprintf('Time constant: %0.2f s\n',params.tau);
    fprintf('Total temperature drop: %0.2f K\n',params.deltaTant+...
        params.deltaTmemb);
    fprintf('Resistance: %0.2f Ohms\n',params.Rinner);
    fprintf('Equivalent heat flux: %0.2f W/m^2\n',params.qequiv);
else
    paramsout=params;
end;

```

D.2 Matlab program: optfun.m

```

function [F] = optfun(X,w,h,Rspoly,alpha,top_matl,...
    membr_matl,deltaf,T,lambda,qapplied)
%function [F] = optfun(X,w,h,Rspoly,alpha,top_matl,...
    membr_matl,deltaf,T,lambda,qapplied)
%
% X(1) = D;    % m
% X(2) = a;    % m
% X(3) = b;    % m
% X(4) = Vdd; % V
%
% F = -sensitivity (uV/W/m^2)

D = X(1);
a = X(2);
b = X(3);
Vdd = X(4);

params = sim_structure(D,a,b,Vdd,w,h,Rspoly,alpha,top_matl,...
    membr_matl,deltaf,T,lambda,qapplied);

```

```
F = -params.sensitivity;
```

D.3 Matlab program: optnonlcon.m

```
function [C,Ceq] = optnonlcon(X,w,h,Rspoly,alpha,...
    top_matl,membr_matl,deltaf,T,lambda,qapplied)
%function [C,Ceq] = optnonlcon(X,w,h,Rspoly,alpha,...
    top_matl,membr_matl,deltaf,T,lambda,qapplied)
%
% X(1) = D;    % m
% X(2) = a;    % m
% X(3) = b;    % m
% X(4) = Vdd; % V
%
% C(X)<=0
% Ceq(X)=0

D=X(1);
a=X(2);
b=X(3);
Vdd=X(4);

params = sim_structure(D,a,b,Vdd,w,h,Rspoly,alpha,...
    top_matl,membr_matl,deltaf,T,lambda,qapplied);

C=[

    % 1/100 scale reading should be 3 times greater than noise
    % 3 - sensitivity*(1/100)*qapplied / Vrms <= 0
    3 - params.sensitivity/1e6*(1/100)*qapplied / params.Vrms;

    % Time constant should be less than 0.3s
    % tau - 0.3 <= 0
    params.tau - 0.3;

    % Equivalent resistive heating less than 1/10 of measured heat flux
    % qequiv / qapplied - 0.1 <= 0
    params.qequiv / qapplied - 0.1;
```

```

% The center post less than 1/10 the diameter of the membrane
% 10 - D/b <= 0
10 - D/b;

% The center post less than 1/10 the diameter of the antenna
% 10 - a/b <= 0
10 - a/b;

% The maximum deflection should be less than 0.1um
% vmax - 0.1 <= 0
params.vmax - 0.1;

% The total temperature drop from antenna to substrate less than 4C
% dTant + dTmemb - 4 <= 0
params.deltaTant + params.deltaTmemb - 4;

% The antenna must be larger than or equal to the membrane
% D - a <= 0
%D - a;

];

Ceq = [];

```

D.4 Matlab program: optimization.m

```

function optimization(Dinit,ainit,binit,Vddinit,top_matl,membr_matl)
%function optimization(Dinit,ainit,binit,Vddinit,top_matl,membr_matl)
%
% optimization of antenna-based structure, NOT assuming antenna and
% membrane are the same size
%
% For material choices, type 'help getprops'

% Semi-fixed values:
w=0.5e-6;      % m
h=1.2e-6;      % m
Rspoly=20;     % Ohm/sq
alpha=0.001;   % unitless

```

```

deltaf=10;      % Hz
T=300;         % K
lambda=3.5e-6; % m
qapplied=1000; % W/m^2

if nargin<6
    membr_matl='nitride';
end
if nargin<5
    top_matl='poly';
end
if nargin>0 & nargin<4
    error('You must specify all initial conditions, or none of them');
end;
if nargin<4
    % Initial guesses:
    Dinit=300e-6; % m
    ainit=300e-6; % m
    binit=30e-6;  % m
    Vddinit=0.5;  % V
end

X0 = [Dinit;ainit;binit;Vddinit];
A=[];B=[];Aeq=[];Beq=[];
LB=[100e-6; % m
    100e-6; % m
    10e-6;  % m
    0.1];   % V
UB=[1000e-6; % m
    1000e-6; % m
    200e-6;  % m
    10];     % V
options=optimset('Diagnostics','on'); %
options=optimset(options,'Display','iter'); %
options=optimset(options,'MaxFunEvals',5000); %
options=optimset(options,'MaxIter',1000); %
options=optimset(options,'LargeScale','off'); %
%options=optimset(options,'GradObj','on'); %

X=fmincon('optfun',X0,A,B,Aeq,Beq,LB,UB,'optnonlcon',options,...
    w,h,Rspoly,alpha,top_matl,membr_matl,deltaf,T,lambda,qapplied);

```

```

D=X(1);
a=X(2);
b=X(3);
Vdd=X(4);

% Display results:
sim_structure(D,a,b,Vdd,w,h,Rspoly,alpha,top_matl,membr_matl,...
    deltaf,T,lambda,qapplied)

% Export all variables to the workspace, so user can play with them:
assignin('caller','D',D);
assignin('caller','a',a);
assignin('caller','b',b);
assignin('caller','Vdd',Vdd);
assignin('caller','w',w);
assignin('caller','h',h);
assignin('caller','Rspoly',Rspoly);
assignin('caller','alpha',alpha);
assignin('caller','top_matl',top_matl);
assignin('caller','membr_matl',membr_matl);
assignin('caller','deltaf',deltaf);
assignin('caller','T',T);
assignin('caller','lambda',lambda);
assignin('caller','qapplied',qapplied);

disp(' ');
disp('You can re-simulate with: "sim_structure(D,a,b,Vdd,w,h,...
    Rspoly,alpha,top_matl,membr_matl,deltaf,T,lambda,qapplied)"');

```

D.5 Modified Gardon Optimization Results

```
>> optimization
```

```

%%%%%%%%%%%%%%%%%%%%%%%%%%%%%%%%%%%%%%%%%%%%%%%%%%%%%%%%%%%%%%%%%%%%%%%%
Diagnostic Information

```

```
Number of variables: 4
```

Functions

Objective: optfun
 Gradient: finite-differencing
 Hessian: finite-differencing
 (or Quasi-Newton)
 Nonlinear constraints: optnonlcon
 Gradient of nonlinear constraints: finite-differencing

Constraints

Number of nonlinear inequality constraints: 7
 Number of nonlinear equality constraints: 0

 Number of linear inequality constraints: 0
 Number of linear equality constraints: 0
 Number of lower bound constraints: 4
 Number of upper bound constraints: 4

Algorithm selected

medium-scale

%%%

End diagnostic information

Iter	F-count	f(x)	max constraint	Step-size	Directional derivative
1	5	-0.809503	1.432	1	0.0782
2	11	-0.693964	0.4542	1	0.294
3	17	-0.401712	0.09113	1	0.0958
4	23	-0.305938	0.01086	1	0.015
5	29	-0.290952	0.000266	1	0.000386
6	35	-0.290566	1.765e-07	1	2.56e-07

Optimization terminated successfully:

Search direction less than 2*options.TolX and
 maximum constraint violation is less than options.TolCon

Active Constraints:

11
 12
 13
 15

Results for membrane=nitride, antenna=poly

```
-----
Membrane diameter (D): 326.62 um
Antenna diameter (a): 326.62 um
Antenna post diameter (b): 32.66 um
Supply voltage (Vdd): 0.25 V
```

```
Sensitivity: 0.29 uV/W/m^2
Time constant: 0.01 s
Total temperature drop: 4.00 K
Resistance: 683.99 Ohms
Equivalent heat flux: 100.00 W/m^2
```

You can re-simulate with:

```
"sim_structure(D,a,b,Vdd,w,h,Rspoly,alpha,top_matl,membr_matl,...
    deltaf,T,lambda,qapplied)"
>> d=sim_structure(D,a,b,Vdd,w,h,Rspoly,alpha,top_matl,...
    membr_matl,deltaf,T,lambda,qapplied)
```

d =

```
    sensitivity: 0.2906
           sion: 0.5811
responsivity: 1.7339
    Rinner: 683.9856
    qelec: 1.0000e+04
    qequiv: 100.0002
    tau: 0.0059
    Vrms: 2.1293e-08
    qrms: 0.0733
    vmax: 7.8627e-04
    deltaTant: 0.1618
    deltaTmemb: 3.8382
```

>>

D.6 Matlab program: findexps.m

```
function [finalvals,beginvals,alphas,plotargs]=findexps(time,...
    data,edgelocs,plotcolors,lovershoot,rovershoot)
```

```

% time is a vector of time values
% data is a VECTOR of data values
% edgelocs is an Nx2 list of sample number pairs denoting
%   where each section is located. edgelocs(:,1) indicates
%   the left- hand edges of each, and edgelocs(:,2)
%   indicates the right side.
% plotcolors is a string indicating the desired color for
%   the plotargs output
% Xovershoot are vectors of how much to extend the plotted
%   fit curve beyond the given limits. zero indicates none,
%   1.0 indicates extend on each end by the total size of
%   the segment. Values greater than 1.0 are interpreted
%   in a literal sense: they are the extension lengths on
%   each side in the units of time. overshoots default
%   to zero.
%
% finalvals is a list of the final values for each exponential
% beginvals is a list of the beginning values for each exponential
% alphas is a list of the alpha values for each exponential
% plotargs is a cell array that can be passed to PLOT to plot
%   the fitted exponentials

if nargin<3
    error('findexps needs at least 3 arguments.');
```

```

end;
if nargin<6
    rovershoot=0.0*ones(size(edgelocs,1),1);
end;
if nargin<5
    lovershoot=0.0*ones(size(edgelocs,1),1);
end;
if nargin<4
    plotcolors='r';
end;

finalvals=[]; beginvals=[]; alphas=[];
plotargs={};
for ii=1:size(edgelocs,1)
    ns=edgelocs(ii,1);
    ne=edgelocs(ii,2);
    t=time(ns:ne);
    [bv,ev,alpha]=realfindexps(t,data(ns:ne));

```

```

    finalvals=[finalvals;ev];
    beginvals=[beginvals;bv];
    alphas=[alphas;alpha];
    if lovershoot(ii)<=1
        lovertime=(time(ne)-time(ns))*lovershoot(ii);
    else
        lovertime=lovershoot(ii);
    end;
    if rovershoot(ii)<=1
        rovertime=(time(ne)-time(ns))*rovershoot(ii);
    else
        rovertime=rovershoot(ii);
    end;
    plottime=linspace(time(ns)-lovertime,time(ne)+rovertime,length(t));
    plotargs=[plotargs {plottime bv+(ev-bv)*(1-exp(alpha*(plottime-...
        time(ns)))) plotcolors}];
end;
fprintf('\n');

```

```

function [beginval,endval,alpha]=realindexps(time,data)
% Given data and time, this function finds the best-fit exponential
% that goes through the data. It returns the data begin value, the
% data end value, and the alpha. The equation fitting the data must
% follow the form:
%
%  $y = BV + (EV - BV)[1 - \exp(\alpha*t)]$ 
%

```

```

TOTAL_ITERATIONS=3;
ARANGE=10;
BRANGE=10;
ERANGE=10;

%rangeperdim=round(TOTAL_POINTS^(1/3));

totalrange=max(data)-min(data);
totaltime=max(time)-min(time);
L=length(data);
data=reshape(data,L,1);
time=reshape(time,L,1);

```

```

beginrange=[data(1)-totalrange/15 data(1)+totalrange/15];
endrange=[data(L)-totalrange/5 data(L)+totalrange/5];
dir=sign(data(L)-data(1));
% Find minimum time point where data goes above 63% point:
if dir>0
    sixtythreept=min(time(find(data>(0.6321*totalrange+min(data)))))...
        -time(1);
else
    sixtythreept=min(time(find(data<(max(data)-0.6321*totalrange))))...
        -time(1);
end;
if sixtythreept==0
    warning('Range not properly selected!');
    return
end;
alphanrange=[-1.3/sixtythreept -0.6/sixtythreept];
%alphanrange=[-1/(time(2)-time(1)) -1/(time(L)-time(1))];

y=data*ones(1,ARANGE);
t=time*ones(1,ARANGE)-time(1);
mincost=inf;

fprintf('Minimizing: ');
for ii=1:TOTAL_ITERATIONS
    for br=linspace(beginrange(1),beginrange(2),BRANGE)
        for er=linspace(endrange(1),endrange(2),ERANGE);
            ar=ones(L,1)*linspace(alphanrange(1),alphanrange(2),ARANGE);
            err=sum(abs(y-br-(er-br)*(1-exp(ar.*t))));
            mc=min(err);
            if (mc<mincost)
                mincost=mc;
                minar=ar(1,find(err==mc));
                minar=minar(1);
                miner=er;
                minbr=br;
            end;
        end;
    end;
    fprintf(' (%0.4g)',mincost);

beginrange=[minbr-(beginrange(2)-beginrange(1))/(BRANGE-1)...
    minbr+(beginrange(2)-beginrange(1))/(BRANGE-1)];

```

```
    endrange=[miner-(endrange(2)-endrange(1))/(ERANGE-1) ...  
             miner+(endrange(2)-endrange(1))/(ERANGE-1)];  
    alphanrange=[minar-(alphanrange(2)-alphanrange(1))/(ARANGE-1) ...  
               minar+(alphanrange(2)-alphanrange(1))/(ARANGE-1)];  
end;  
fprintf(' Done.\n');  
  
beginval=mean(beginrange);  
endval=mean(endrange);  
alpha=mean(alphanrange);
```